

Dynamics of free and bound excitons in GaN nanowires: Origin of the nonradiative recombination channel

DISSERTATION

zur Erlangung des akademischen Grades

doctor rerum naturalium

(Dr. rer. nat.)

im Fach Physik

eingereicht an der

Mathematisch-Naturwissenschaftlichen Fakultät

Humboldt-Universität zu Berlin

von

Dipl.-Phys. Christian Hauswald

Präsident der Humboldt-Universität zu Berlin:

Prof. Dr. Jan-Hendrik Olbertz

Dekan der Mathematisch-Naturwissenschaftlichen Fakultät:

Prof. Dr. Elmar Kulke

Gutachter:

(i) Prof. Dr. Henning Riechert

(ii) Prof. Dr. Oliver Benson

(iii) Dr. Pierre Lefebvre

eingereicht am: 04.12.2014

Tag der mündlichen Prüfung: 12.03.2015

*'If a man will begin with certainties, he shall end in doubts;
but if he will be content to begin with doubts, he shall end in certainties.'*

Sir Francis Bacon
The Advancement of Learning, vol. 1 (1605)

Abstract

GaN nanowires (NWs) can be fabricated with a high structural perfection on various crystalline and amorphous substrates. They offer intriguing possibilities for both fundamental investigations of the GaN material system as well as applications in optoelectronic devices. Although prototype devices based on GaN NWs have been presented already, several fundamental questions remain unresolved to date. In particular, the internal quantum efficiency (IQE), an important basic figure of merit for optoelectronic applications, is essentially unknown for GaN NWs.

This thesis presents a detailed investigation of the exciton dynamics in GaN NWs using continuous-wave and time-resolved photoluminescence (PL) spectroscopy. Spontaneously formed ensembles and ordered arrays of GaN NWs grown by molecular-beam epitaxy are examined. The experiments are combined with simulations based on the solution of rate equation systems to obtain new insights into the recombination dynamics in GaN NWs at low temperatures. In particular, the free and bound exciton states in GaN NWs are found to be coupled and affected by a nonradiative channel between 10 and 300 K. The investigation of samples with different NW diameters and coalescence degrees conclusively shows that the dominating nonradiative channel is neither related to the NW surface nor to coalescence-induced defects. Hence, we conclude that nonradiative point defects are the origin of the fast recombination dynamics in GaN NWs, and limit the IQE of the investigated samples to about 20% at cryogenic temperatures. We also demonstrate that the frequently observed biexponential decay for the donor-bound exciton originates from a coupling with the acceptor-bound exciton state in the GaN NWs. Motivated by an experimentally observed, strong dependence of the PL intensity of ordered GaN NW arrays on the NW diameter, we perform numerical simulations of the light absorption and extraction to explore the external quantum efficiency of these samples.

Keywords: GaN, nanowire, time-resolved photoluminescence, surface, coalescence, free excitons, bound excitons, radiative recombination, nonradiative recombination, internal quantum efficiency, absorption, extraction efficiency, external quantum efficiency

Zusammenfassung

GaN-Nanodrähte können mit einer hohen strukturellen Perfektion auf verschiedenen kristallinen und amorphen Substraten gewachsen werden. Sie bieten somit faszinierende Möglichkeiten, sowohl zur Untersuchung von fundamentalen Eigenschaften des Materialsystems, als auch in der Anwendung in optoelektronischen Bauteilen. Obwohl bereits verschiedene Prototypen solcher Bauteile vorgestellt wurden, sind viele grundlegende Eigenschaften von GaN-Nanodrähten noch ungeklärt, darunter die interne Quanteneffizienz (IQE), welche ein wichtiges Merkmal für optoelektronische Anwendungen darstellt.

Die vorliegende Arbeit präsentiert eine detaillierte Untersuchung der Rekombinationsdynamik von Exzitonen, in selbst-induzierten und selektiv gewachsenen GaN Nanodraht-Proben, welche mit Molekularstrahlepitaxie hergestellt wurden. Die zeitaufgelösten Photolumineszenz (PL)-Experimente werden durch Simulationen ergänzt, welche auf Ratengleichungs-Modellen basieren. Es stellt sich heraus, dass die Populationen von freien und gebundenen Exzitonen gekoppelt sind und zwischen 10 und 300 K von einem nichtstrahlenden Kanal beeinflusst werden. Die Untersuchung von Proben mit unterschiedlichem Nanodraht-Durchmesser und Koaleszenzgrad zeigt, dass weder die Nanodraht-Oberfläche, noch Defekte als Folge von Koaleszenz diesen nichtstrahlenden Kanal induzieren. Daraus lässt sich folgern, dass die kurze Zerfallszeit von Exzitonen in GaN-Nanodrähten durch Punktdefekte verursacht wird, welche die IQE bei 10 K auf 20 % limitieren. Der häufig beobachtete biexponentiellen PL-Zerfall des Donator-gebundenen Exzitons wird analysiert und es zeigt sich, dass die langsame Komponente durch eine Kopplung mit Akzeptoren verursacht wird. Motiviert durch Experimente, welche eine starke Abhängigkeit der PL-Intensität vom Nanodraht-Durchmesser zeigen, wird die externe Quanteneffizienz von geordneten Nanodraht-Feldern mit Hilfe numerischer Simulationen der Absorption und Extraktion von Licht in diesen Strukturen untersucht.

Stichwörter: GaN, Nanodrähte, zeitaufgelöste Photolumineszenz, Exzitonen, strahlende Rekombination, nichtstrahlende Rekombination, interne Quanteneffizienz, optische Extinktion, Extraktionseffizienz, externe Quanteneffizienz

List of publications

Publications of parts of this work

C. Hauswald, P. Corfdir, J. K. Zettler, V. M. Kaganer, K. K. Sabelfeld, S. Fernández-Garrido, T. Flissikowski, V. Consonni, T. Gotschke, H. T. Grahn, L. Geelhaar, and O. Brandt, *Origin of the nonradiative decay of bound excitons in GaN nanowires*, Phys. Rev. B **90**, 165304 (2014)

C. Hauswald, T. Flissikowski, H. T. Grahn, L. Geelhaar, H. Riechert, and O. Brandt, *Radiative and nonradiative decay of excitons in GaN nanowires*, (**invited paper**), Proc. SPIE Gall. Nitride Mater. Devices **IX**, edited by J.-I. Chyi, Y. Nanishi, H. Morkoç, J. Piprek, E. Yoon, and H. Fujioka, p. 89860V (2014)

C. Hauswald, T. Flissikowski, T. Gotschke, R. Calarco, L. Geelhaar, H. T. Grahn, and O. Brandt, *Coupling of exciton states as the origin of their biexponential decay dynamics in GaN nanowires*, Phys. Rev. B **88**, 075312 (2013).

Further publications

P. Corfdir, J. K. Zettler, C. Hauswald, S. Fernández-Garrido, O. Brandt, and P. Lefebvre, *Sub-meV linewidth in GaN nanowire ensembles: Absence of surface excitons due to the field ionization of donors*, Phys. Rev. B **90**, 205301 (2014).

P. Corfdir, C. Hauswald, J. K. Zettler, T. Flissikowski, J. Lähnemann, S. Fernández-Garrido, L. Geelhaar, H. T. Grahn, O. Brandt, *Stacking faults as quantum wells in nanowires: Density of states, oscillator strength and radiative efficiency*, Phys. Rev. B **90**, 195309 (2014).

S. Fernández-Garrido, V. M. Kaganer, C. Hauswald, B. Jenichen, M. Ramsteiner, V. Consonni, L. Geelhaar and O. Brandt *Correlation between the structural and optical properties of spontaneously formed GaN nanowires: a quantitative evaluation of the impact of nanowire coalescence*, Nanotechnology **25**, 455702 (2014).

List of publications

- J. Lähnemann, C. Hauswald, M. Wölz, U. Jahn, M. Hanke, L. Geelhaar, O. Brandt, *Localization and defects in axial (In,Ga)N/GaN nanowire heterostructures investigated by spatially resolved luminescence spectroscopy*, J. Phys. D. Appl. Phys. **47**, 394010 (2014).
- C. Somaschini, S. Bietti, A. Trampert, U. Jahn, C. Hauswald, H. Riechert, S. Sanguinetti, and L. Geelhaar, *Control over the Number Density and Diameter of GaAs Nanowires on Si(111) Mediated by Droplet Epitaxy*, Nano Lett. **13**, 3607 (2013).
- J. Kamimura, P. Bogdanoff, J. Lähnemann, C. Hauswald, L. Geelhaar, S. Fiechter, and H. Riechert, *Photoelectrochemical Properties of (In,Ga)N Nanowires for Water Splitting Investigated by in Situ Electrochemical Mass Spectroscopy*, J. Am. Chem. Soc. **135**, 10242 (2013).
- O. Marquardt, C. Hauswald, M. Wölz, L. Geelhaar, and O. Brandt, *Luminous efficiency of axial $In_xGa_{1-x}N/GaN$ nanowire heterostructures: interplay of polarization and surface potentials*, Nano Lett. **13**, 3298 (2013).
- C. Chèze, M. Siekacz, G. Muzioł, H. Turski, S. Grzanka, M. Kryśko, J. L. Weyher, M. Boćkowski, C. Hauswald, J. Lähnemann, O. Brandt, M. Albrecht, and C. Skierbiszewski, *Investigation on the origin of luminescence quenching in N-polar (In,Ga)N multiple quantum wells*, J. Vac. Sci. Technol. B Microelectron. Nanom. Struct. **31**, 03C130 (2013).
- M. Sawicka, C. Chèze, H. Turski, G. Muzioł, S. Grzanka, C. Hauswald, O. Brandt, M. Siekacz, R. Kucharski, T. Remmele, M. Albrecht, M. Kryśko, E. Grzanka, T. Sochacki, and C. Skierbiszewski, *Ultraviolet light-emitting diodes grown by plasma-assisted molecular beam epitaxy on semipolar GaN (2021) substrates*, Appl. Phys. Lett. **102**, 111107 (2013).
- M. Wölz, S. Fernández-Garrido, C. Hauswald, O. Brandt, F. Limbach, L. Geelhaar, and H. Riechert, *Indium incorporation in InGaN/GaN nanowire heterostructures investigated by line-of-sight quadrupole mass spectrometry*, Cryst. Growth Des. **12**, 5686 (2012).
- P. Dogan, O. Brandt, C. Hauswald, R. Calarco, A. Trampert, L. Geelhaar, and H. Riechert, *Influence of nanowire template morphology on the coalescence overgrowth of GaN nanowires on Si by molecular beam epitaxy*, Proc. SPIE Gall. Nitride Mater. Devices **VII**, pp. 82620P1 - 82620P8 (2012).
- F. Limbach, C. Hauswald, J. Lähnemann, M. Wölz, O. Brandt, A. Trampert, M. Hanke, U. Jahn, R. Calarco, L. Geelhaar, and H. Riechert, *Current path in light emitting diodes based on nanowire ensembles*, Nanotechnology **23**, 465301, (2012).

M. Wölz, J. Lähnemann, O. Brandt, V. M. Kaganer, M. Ramsteiner, C. Pfüller, C. Hauswald, C. N. Huang, L. Geelhaar, and H. Riechert, *Correlation between In content and emission wavelength of $In_xGa_{(1-x)}N/GaN$ nanowire heterostructures*, *Nanotechnology* **23**, 455203 (2012).

Conference presentations

C. Hauswald, *Radiative and nonradiative decay of excitons in GaN nanowires*, **(invited talk)**, SPIE Photonics West 2014, San Francisco, USA, February 2014

C. Hauswald, T. Flissikowski, T. Gotschke, R. Calarco, L. Geelhaar, H. T. Grahn, and O. Brandt, *Biexponential luminescence decay in GaN nanowire ensembles as a signature for the coupling of bound exciton states*, **(contributed talk)**, 10th International Conference on Nitride Semiconductors (ICNS), Washington DC, USA, August 2013

C. Hauswald, O. Brandt, T. Flissikowski, T. Gotschke, R. Calarco, L. Geelhaar, H. T. Grahn and H. Riechert, *Photoluminescence intensity and lifetime of ordered arrays of GaN nanowires with different diameter and pitch* **(Poster)**, Spring Meeting of the German Physical Society (DPG), Regensburg, March 2013

C. Hauswald, O. Brandt, T. Flissikowski, T. Gotschke, R. Calarco, L. Geelhaar, H.T. Grahn and H. Riechert, *Recombination dynamics of free and bound excitons in GaN nanowires with different diameters grown by selective area epitaxy on Si substrates* **(Poster)**, Nanowires Workshop 2012, Berlin, September 2012

C. Hauswald, T. Gotschke, O. Brandt, N. Koo, J. W. Kim, R. Calarco, L. Geelhaar and H. Riechert, *μ -Photoluminescence of GaN nanowires with different diameter and pitches grown by selective-area epitaxy on Si substrates* **(contributed talk)**, Spring Meeting of the German Physical Society (DPG), Berlin, March 2012

Abbreviations

(A^0, X)	(neutral) acceptor-bound exciton
CCD	charge-coupled device
cw(-PL)	continuous-wave (photoluminescence)
$(D^0, X_{A,B})$	(neutral) donor-bound A-, B-exciton
EBL	electron-beam lithography
EQE	external quantum efficiency
FEM	finite element method
FDTD	finite-difference time-domain
FWHM	full width at half maximum
IQE	internal quantum efficiency
LED	light-emitting diode
LO	longitudinal optical (phonon)
LPB	lower polariton branch
MBE	molecular beam epitaxy
μ PL	micro-photoluminescence
NBE	near-band edge (luminescence)
NW	nanowire
PL	photoluminescence
SAG	selective-area growth
SC	streak camera
SEM	scanning electron microscopy
SF	(basal plane) stacking fault
TEM	transmission electron microscopy
TES	two-electron satellite
TRPL	time-resolved photoluminescence
UPB	upper polariton branch
$X_{A,B,C}$	free A-,B-,C-exciton

List of basic symbols

Symbol	Name	Unit
α	ratio of surface near to total donors in the core-shell model	
A	Absorbance	
c_0	speed of light in vacuum (299 792 458)	m s^{-1}
c	speed of light in a medium	m s^{-1}
d_{disk}	equivalent disk diameter	nm
d^*	effective nanowire diameter	nm
e	elementary charge (1.602×10^{-19})	C
E_g	band gap energy	eV
ϵ	dielectric constant	
ϵ_0	vacuum permittivity (8.854×10^{-12})	F m^{-1}
\hbar	Planck constant divided by 2π (1.054×10^{-34})	Js
k_B	Boltzmann constant (1.381×10^{-23})	J K^{-1}
k	wavevector or reciprocal space vector	
m_0	electron rest mass (9.109×10^{-31})	kg
m_e^*	reduced effective electron mass	m_0
m_h^*	reduced effective hole mass	m_0
n	real part of the refractive index	
\tilde{n}	complex refractive index	
η_{coll}	collection efficiency	
η_{ext}	external quantum efficiency	
η_{extr}	extraction efficiency	
η_{int}	internal quantum efficiency	
$N_{\text{D,A}}$	donor / acceptor concentration	cm^{-3}
P	Perimeter	nm
R	Reflectance	
S	surface recombination velocity	cm/s
σ	Coalescence degree of a nanowire ensemble	
$\tau_{\text{eff,r,nr}}$	effective / radiative / non-radiative lifetimes	
T	Temperature or Transmittance as indicated	

Contents

List of publications	vii
Abbreviations	xi
List of basic symbols	xiii
Contents	xv
1. Introduction	1
2. Fundamentals	5
2.1. Crystal structure and electronic band structure of GaN	5
2.2. Recombination processes in bulk GaN and GaN nanowires (NWs)	7
2.2.1. Radiative processes	7
2.2.2. Nonradiative processes and internal quantum efficiency	16
2.3. Absorption and extraction of light in planar layers and NW ensembles . . .	18
3. Experimental and numerical methods	21
3.1. GaN NWs fabricated by spontaneous formation and selective-area growth	21
3.2. Continuous-wave μ -photoluminescence spectroscopy	25
3.3. Time-resolved μ -photoluminescence spectroscopy	27
3.4. Introduction to the numerical methods	31
3.4.1. Finite-element method	31
3.4.2. Finite-difference time-domain method	32
4. Spectroscopy of NW ensembles and single NWs - a treatise on the benefits of good statistics	35
4.1. Differences between dispersed and as-grown GaN NW PL measurements	35
4.2. Role of statistics in optical spectroscopy of GaN NWs	37

Contents

4.3. Spectroscopy of single free-standing GaN NWs in samples grown by selective-area epitaxy	40
5. Investigating the origin of the fast decay of bound excitons in GaN nanowires	45
5.1. Introduction	45
5.2. Considering an enhanced radiative recombination rate of bound excitons	47
5.3. A first step towards understanding the PL transient of GaN NWs	48
5.4. Investigating the origin of the short component of the bound exciton decay	53
5.4.1. Observation of identical lifetimes of the free and donor-bound exciton	53
5.4.2. Temperature dependence of the PL intensity and exciton lifetimes	55
5.4.3. Rate equation model describing the coupling of free and bound excitons	57
5.4.4. Dependence of the effective lifetime on the surface-to-volume ratio	61
5.4.5. Dependence of the effective lifetime on the coalescence degree . . .	63
5.5. Conclusion	64
6. Origin of the biexponential exciton decay transient in GaN nanowires	67
6.1. Motivation: PL transients of the investigated GaN NW ensembles	67
6.2. Spectral properties in cw and transient photoluminescence spectroscopy .	69
6.3. Modeling with a system of nonlinear rate equations	71
6.4. Discussion of the simulation results and origin of the coupling	74
6.4.1. Possible impact of the electric fields in GaN NWs	78
6.5. Coupling between other bound exciton states	79
6.6. Conclusion	81
7. Internal and external quantum efficiency of ordered arrays of GaN nanowires	83
7.1. Motivation: Photoluminescence intensity of ordered GaN NW arrays with different NW diameters	83
7.2. Internal quantum efficiency of ordered arrays of GaN nanowires	86
7.3. Coupling of light into ordered arrays of GaN NWs and subsequent absorption	87
7.3.1. Introductory example: Absorbance of a GaN slab	87
7.3.2. Calculating the absorbance of ordered GaN NW arrays	89
7.4. Extraction efficiency of GaN NWs	92
7.4.1. Guided modes in GaN NWs	95
7.4.2. Comment: Ordered NW arrays as a photonic crystal	100
7.5. Summary	100
8. Conclusions and outlook	103

A. Diameter distribution and coalescence degree of nanowire ensembles	109
B. List of samples	115
Bibliography	117
List of figures	135

Introduction

The history of semiconductor physics has demonstrated many times that crystals of high structural perfection with precise control over the density of impurities are required to facilitate both the investigation of fundamental physical processes of the material and the development of efficient devices.^[1] A prominent example is the III-V compound semiconductor GaN. This material has been epitaxially grown since the late 1960s,^[2] but it took 40 years until the material reached a structural perfection sufficient to enable the production of efficient light-emitting devices. Currently, GaN-based light emitters are widely used in optoelectronics, and have started to revolutionize solid-state lighting.^[3,4] Three of the pioneers of this field, Isamu Akasaki, Hiroshi Amano and Shuji Nakamura, will receive the 2014 Nobel Prize in physics for their work on improving the structural perfection of GaN epitaxial films and controlling the *p*-doping of GaN.^[5] The substantial amount of time required for this breakthrough was largely the result of the difficulty in obtaining GaN layers of sufficiently high structural perfection and purity by epitaxial growth on dissimilar substrates with significant lattice and thermal mismatch.^[6]

It is in this context that semiconductor nanowires (NWs) have opened a new era both in material research and device development, as their limited interfacial area with the substrate lifts the most fundamental constraint in epitaxy, namely, finding a suitable substrate for film growth.^[7] Nanowires can be grown with a high degree of structural perfection on various crystalline and amorphous substrates and thus provide new flexibility for the investigation of fundamental aspects of various semiconductors which lack a native substrate. Additionally, their unique geometry opens up promising perspectives for novel types of three-dimensional device integration in various fields.^[7-9] A prominent example of an advance in fundamental physics enabled by the NW geometry is the recent observation of Majorana fermions in hybrid superconductor-semiconductor devices made of InSb NWs.^[10] Progress in applications are also foreseen with the use of NWs, for example in photonics^[11] and solid-state lighting.^[12,13] However, many well established characterization techniques used for planar layers have yet to be adapted for NWs. Consequently, several fundamental properties of NWs remain unknown for certain materials,

1. Introduction

e. g., the NW point defect density and the impact of the large surface-to-volume ratio of NWs compared to conventional planar layers.

Motivated by the advantages of the NW geometry and the ongoing challenges in the growth of planar GaN, significant effort has been devoted to the integration of GaN NWs into optoelectronic devices, employing either bare GaN or heterostructures of the ternary compounds (In,Ga)N and (Al,Ga)N. Prototype devices include light-emitting diodes in the visible^[14] and ultraviolet spectral range,^[15] photodetectors,^[16] devices for intraband absorption,^[17] on-chip optical interconnects,^[18] and room temperature single-photon sources.^[19] Nevertheless, many fundamental aspects of these structures are not thoroughly understood yet, especially the generation, transport, and recombination of carriers. These processes play a central role in the operation of all semiconductor devices, and thus a comprehensive understanding of them is crucial for the further development of NW-based devices.

The difficulties in characterizing NWs can be seen in the lack of a reliable measure for the internal quantum efficiency of GaN NWs, which is an important figure of merit for the maturity of semiconductor crystals employed in optoelectronic applications.^[20] The relevant underlying physical process in light-emitting devices is the radiative recombination of electrons and holes. Due to their strong Coulomb interaction in GaN, the luminescence spectrum of the crystal is governed by the radiative recombination of bound electron-hole pairs, i. e., excitons, up to room temperature. Fundamentally, the internal quantum efficiency is governed by the ratio of the radiative and nonradiative exciton recombination rates. In order to investigate the radiative recombination of excitons, it is advantageous to cool the crystal to a cryogenic temperatures, which minimizes the contribution of nonradiative processes. In addition, the luminescence lines are much narrower and the intensity is higher at low temperatures, which further facilitates their investigation by optical spectroscopy.

While excitons can be considered free quasi-particles at room temperature, at low temperature excitons bind to impurities in the crystal. Fundamentally, the bound exciton complex is characterized by its energy and radiative lifetime, and both of these quantities can, in principle, be accessed by photoluminescence (PL) spectroscopy. Their experimental determination is, however, a formidable challenge which requires material with high structural perfection and a low density of nonradiative point defects. Consequently, careful experiments on thick, free-standing GaN layers provided only recently reliable values for both of these quantities,^[21,22] despite the first spectroscopic investigation of excitons in GaN date back to the 1970s.^[23]

A potential light-emitting device is not only characterized by its internal quantum efficiency, but also the extraction efficiency for the generated photons has to be taken into account. The product of both quantities is called external quantum efficiency. When NW ensembles are investigated by optical spectroscopy, major differences in the extraction efficiency are expected compared to planar structures. These differences originate from several phenomena related to the small cross-sectional size of the NWs, which, in

many cases, is comparable to the optical wavelength.^[24] Waveguiding effects inside the NWs^[25,26] and the complex far-field patterns of these sub-wavelength sized light emitters were found to play an important role.^[27] Consequently, the coupling of light into and out of NW ensembles needs to be explored in detail in order to quantify their external quantum efficiency.

The present thesis is devoted to the spectroscopic investigation of GaN NW ensembles — mainly at cryogenic temperatures — by continuous-wave (cw) and time-resolved PL spectroscopy in order to explore their internal and external quantum efficiencies. We study both spontaneously grown GaN NW ensembles and ordered arrays produced by selective-area growth using molecular-beam epitaxy on Si(111) substrates.

Following this introduction, the fundamental physics necessary to understand the results presented in this thesis are summarized in Chap. 2. This chapter provides a description of the crystallography and band structure of GaN, the generation of excitons, the physical concept of exciton-polaritons, as well as the various radiative and nonradiative recombination channels of free and bound excitons in GaN. The current understanding of the spectral peculiarities as well as of the exciton dynamics of GaN NWs are discussed in detail.

Chapter 3 presents the methodological background of this work. A description of the basic mechanisms of GaN NW formation both by spontaneous nucleation and selective-area growth is introduced. The remainder of the chapter then focuses on the experimental setups used for cw and time-resolved PL spectroscopy, as well as presenting the methods for data processing and analysis. Finally, the numerical methods used for studying the interaction of light with NWs are briefly described.

The presented spectroscopic experiments focus on the investigation of GaN NW ensembles rather than on single wires. The reasoning behind this decision is presented in Chap. 4 and motivated by a discussion of the differences between single NW and ensemble NW spectroscopy.

In Chap. 5, the central question of this thesis is presented: What is the physical origin of the peculiar, biexponential low-temperature PL transient of the donor-bound exciton complex in GaN NW ensembles? First, two intuitive models are presented which seek to explain the observed data via a straightforward correlation of the PL transient with structural parameters of the NW ensembles. However, these models do not yield satisfactory results. We thus focus first on the investigation of the origin of the fast component of the bound exciton decay in GaN NWs, employing a combination of temperature-dependent cw and time-resolved PL spectroscopy. As a direct result of these measurements, the interplay between the free and donor-bound exciton populations in GaN NWs is explored, and a coupling of both states is revealed. Hence, the donor-bound exciton complex may decay nonradiatively via the free exciton state. In view of this result, the chapter concludes with a reexamination of the influence of the NW surface and the degree of coalescence in the NW ensemble on the effective exciton lifetime.

Chapter 6 proceeds with the investigation of the slow component of the biexponential

1. Introduction

PL decay of the donor-bound exciton in GaN NW ensembles. The samples are investigated by cw and time-resolved PL spectroscopy, and an extended rate equation model is introduced to quantitatively describe the experimental data. It turns out that the slow component in the biexponential decay is caused by the coupling of the donor-bound exciton state, with the acceptor-bound exciton state which exhibits a longer effective lifetime. Finally, possible origins for the coupling between different excitonic states in GaN NWs are discussed, and it is shown that the combination of the results obtained in Chaps. 5 and 6 provide a consistent generalized picture of the low-temperature exciton dynamics within these structures.

Chapter 7 further extends the optical investigation of GaN NW ensembles by taking into account the absorption and extraction efficiency of ordered NW arrays for a PL experiment. An approach combining PL spectroscopy and numerical simulations is employed to explain unexpected results obtained for the PL intensity of these samples and to explore their external quantum efficiency.

Finally, Chap. 8 offers general conclusions drawn from the results presented as well as an outlook for further studies and discusses the implications of the present work for GaN NW-based optoelectronic devices.

Fundamentals

In this chapter, the fundamentals necessary for the understanding of this thesis are presented. In Sec. 2.1, the crystal structure and bandstructure of GaN are introduced. Section 2.2 describes the generation and properties of free and bound excitons in direct semiconductors, as well as the different radiative and nonradiative processes which govern the recombination in GaN after optical excitation. Additionally, the specific transitions observed for GaN nanowires (NWs) and their reported decay times are discussed. Finally, Sec. 2.3 provides an introduction on the differences between planar layers and NW ensembles regarding their absorption and extraction of light. The chapter is based mainly on the books of C. Kittel,^[28] H. Morkoç,^[29,30] B. I. Shklovskii,^[1] R. S. Knox,^[31] and I. Pelant,^[32] but original references are provided as well.

2.1. Crystal structure and electronic band structure of GaN

In a single-crystalline solid, the individual constituents, for example atoms, are arranged in a highly ordered, periodic lattice extending in all directions. It is this strict periodicity which enables the description of many physical properties of crystals within the Brillouin zone. For example, the periodicity allows us to describe the energy eigenstates of electrons inside the crystal by periodic Bloch waves. This concept is part of the theory of the electronic band structure and leads to the formation of energy bands in crystals which are separated by bandgaps. The III-V semiconductor GaN exhibits two crystal phases, the meta-stable zincblende phase with a cubic symmetry and the stable wurtzite phase in which both the N and Ga atoms are arranged in a hexagonal close-packed lattice. The latter is displayed in Fig. 2.1(a). Figure 2.1(b) shows a schematic representation of the resulting energy levels for wurtzite GaN at the Γ -point of the Brillouin zone. At this point the conduction band minimum coincides with the valence band maximum forming a direct bandgap of $E_g = 3.503$ eV at 1.8 K.^[33] As depicted schematically in Fig. 2.1, the combination of the spin-orbit coupling (Δ_{so}) and the crystal field (Δ_{cf}) of the anisotropic wurtzite phase along the $\langle 0001 \rangle$ -direction causes a splitting of the valence band into three subbands which are denoted by A, B and C.^[34] The magnitude

2. Fundamentals

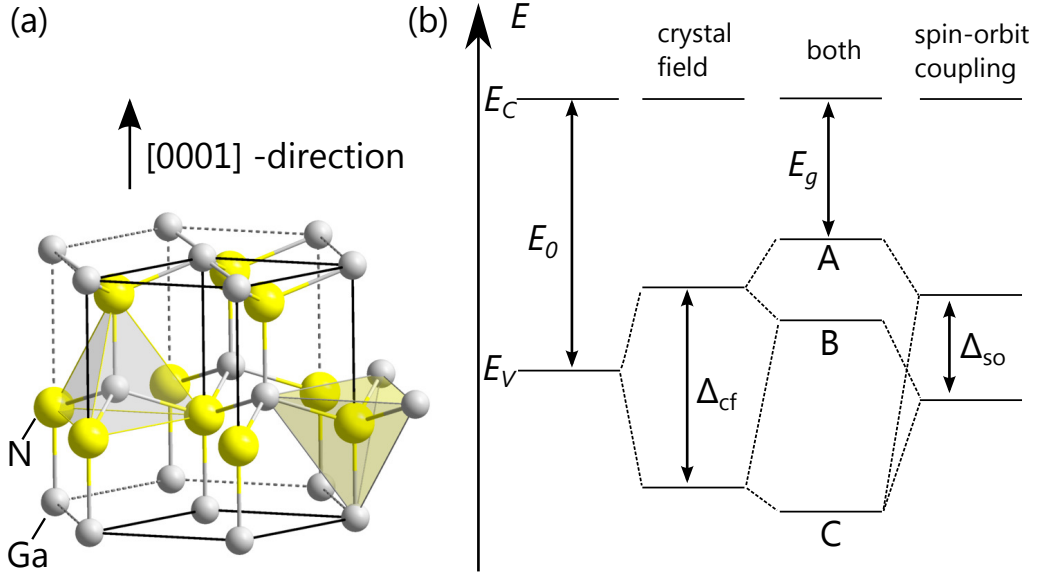


Figure 2.1: (a) Schematic representation of the wurtzite crystal structure of GaN. The solid lines depict the unit cell of the crystal (image source: Ref. 36) (b) Energy levels of wurtzite GaN at the Γ -point.^[37] Schematically displayed is the lifting of the degeneracy of the valence band (E_V) by the crystal field (Δ_{cf}) and the spin-orbit interaction (Δ_{so}) leading to the three valence bands named A, B and C due to a combination of both effects. E_g and E_0 denote the fundamental and average bandgap of the material, respectively, and E_C represents the conduction band.

of the spin-orbit and crystal field splitting in unstrained GaN are $\Delta_{so} = 19.7 \pm 1.5$ meV and $\Delta_{cf} = 9.3 \pm 0.3$ meV, respectively.^[35] The lifting of the degeneracy of the valence band gives also rise to the different polarization of photons originating from the different bands. For example, photons emitted from a process related to the A valence band are polarized perpendicular to the $\langle 0001 \rangle$ -direction, because an optical transition parallel to this axis is dipole-forbidden. In contrast, the B exciton is always dipole allowed. Since, we will not perform any polarization-resolved PL experiments within this thesis, we will not discuss the selection rules in more detail.

When GaN is grown at low temperatures, or under conditions where a high concentration of impurities is present, local deviations from the stacking sequence of the crystal along the $\langle 0001 \rangle$ -direction are formed. They are called stacking faults (SF), and the most elementary deviation from the original stacking sequence is the I_1 -SF.^[38] Stacking faults in the basal plane can be regarded as the limiting case of very thin zincblende segments in a wurtzite matrix. Due to the smaller bandgap of the zincblende phase, the I_1 -SF acts as a quantum well (QW),^[39] localizing electrons and, via the Coulomb interaction, also excitons. In addition, stacking faults exhibits perfect interfaces and thus represent very efficient radiative recombination channels.^[38] In planar GaN, the I_1 -SF is terminated by partial dislocations inside the material, while in the specific case of GaN NWs, the I_1 -SF

2.2. Recombination processes in bulk GaN and GaN nanowires (NWs)

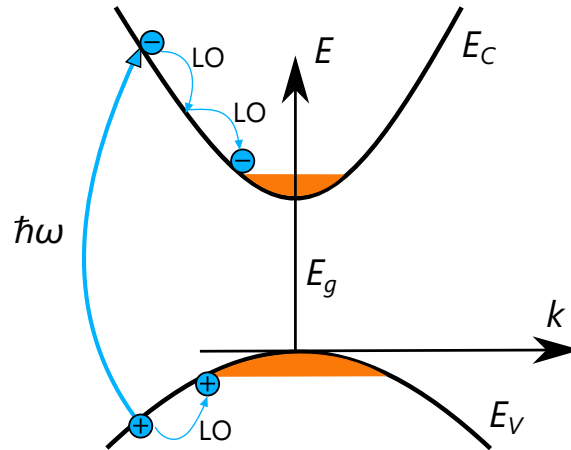


Figure 2.2: Schematic representation of the excitation of free carriers in a direct semiconductor by photons with $\hbar\omega > E_g$. The electron is lifted from the valence band (E_V) to the conduction band (E_C) leaving behind a hole. Both carriers thermalize via the emission of LO phonons to the bandedges. The orange area depicts the area where further thermalization can only occur via the emission of acoustic phonons.

was found to extend through the whole NW perpendicular to the growth direction (i. e., perpendicular to the $\langle 0001 \rangle$ direction).^[40]

2.2. Recombination processes in bulk GaN and GaN nanowires (NWs)

Photoluminescence spectroscopy is a highly sensitive, non-destructive optical method to investigate defects and impurities in direct semiconductors. An optical excitation inside the crystal is a non-equilibrium state and thus loses its excitation energy after a certain time and returns to the ground state. This transition can occur either via a radiative decay, i. e., by emitting a photon, or via a nonradiative decay where the energy is transferred to the lattice via phonons. In the following sections, examples for both processes are presented and the most important radiative and nonradiative channels in bulk GaN and GaN NWs are discussed. We will focus the discussion on optical transitions close to the band edge of GaN as the investigated samples do not exhibit any deep level luminescence.

2.2.1. Radiative processes

Excitation of carriers and the formation of free excitons

In a photoluminescence experiment, a semiconductor is excited with a photon energy $\hbar\omega > E_g$ as schematically depicted in Fig. 2.2. In this energy range, direct semiconductors exhibit a strong absorption of photons, causing electrons from the valence band to be

2. Fundamentals

excited into the conduction band and leaving behind holes (i. e., missing electrons) in the valence band. The resulting free electrons and holes thermalize to the minimum of the conduction band and maximum of the valence band, respectively, by the emission of longitudinal optical (LO) phonons. Once their energy is below that of one LO phonon, they can only further reduce their energy via the emission of acoustical phonons. During this process, the free electrons and holes attract each other by the Coulomb force, and eventually form quasi-particles of excitation, called excitons. Note that both, the process of exciton formation and the thermalization of carriers happen in parallel and on the timescale of picoseconds.

The theory of excitons was formulated in the 1930s by Frenkel, Peierls and Wannier.^[41–44] Excitons in III-V and II-VI semiconductors have typically a low binding energy and thus a large radius, which means their wavefunction extends over many unit cells of the crystal. These excitons can move freely inside an ideal crystal and are called Wannier excitons.*

A simple picture of the free Wannier exciton can be obtained when we ignore all particles in the system except the excited electron and hole. The periodic potential of the remaining valence electrons and cores gives rise to new effective masses m_e^* and m_h^* for the excited electron and hole, respectively. The interaction between the two particles is given by the Coulomb attraction, which leads to the following Schrödinger equation of this two-particle system, namely, the free exciton:

$$\left(-\frac{\hbar^2 \nabla_e^2}{2m_e^*} - \frac{\hbar^2 \nabla_h^2}{2m_h^*} - \frac{e^2}{\epsilon r_{eh}} \right) \Psi = E\Psi. \quad (2.1)$$

Here, ϵ is the dielectric constant and r_{eh} represents the distance between the electron and the hole. Analogously to the solution of the Schrödinger equation for the hydrogen atom, the center-of-mass motion can be separated from the relative motion of the two particles, which yields the following solution for the free exciton wave function:

$$\Psi = \frac{1}{\sqrt{(V)}} e^{i\mathbf{k}\mathbf{R}} F(\mathbf{r}) \quad (2.2)$$

where \mathbf{k} is the crystal momentum, V the volume of the crystal, $F(\mathbf{r})$ denotes the relative motion of both particles and

$$\mathbf{R} = \frac{1}{2}(\mathbf{r}_e + \mathbf{r}_h) \quad \text{and} \quad \mathbf{r} = \mathbf{r}_e - \mathbf{r}_h \quad (2.3)$$

*In an ideal pure and infinite crystal exhibiting no impurities, structural or point defects, the free Wannier exciton is a coherent excitation of the whole crystal from a quantum mechanical point of view.^[45] However, experimentally, diffusion lengths of the free exciton of 50 – 200 nm have been determined in real GaN crystals,^[46–48] which shows that a classical description of the free exciton may often be more appropriate.

2.2. Recombination processes in bulk GaN and GaN nanowires (NWs)

are the coordinates for the center-of-mass and relative motion of the electron and the hole forming the exciton. The solution of Eq. 2.1 then yields the total energy of the exciton in the n th state:

$$E_n = E_g + E_{\text{kin}} - E_{\text{FX}} = E_g + \frac{\hbar^2 k^2}{2(m_e^* + m_h^*)} - \frac{\mu e^4}{32\pi^2 \hbar^2 \epsilon^2 n^2}. \quad (2.4)$$

Here, E_{kin} denotes the kinetic energy of the exciton and E_{FX} the exciton binding energy where μ is the reduced exciton mass given by $\mu = (1/m_e^* + 1/m_h^*)^{-1}$. The exciton Bohr radius, i. e. the 'size' of the exciton is then defined as:

$$a_B = \frac{4\pi\hbar^2\epsilon}{\mu e^2} n^2 \quad (2.5)$$

Using isotropic masses $m_e^* = 0.2m_0$, $m_h^* = 1.1m_0$ and a dielectric constant $\epsilon = 9.5$ for GaN, we find $E_{\text{FX}} = 25 \text{ meV}$ and $a_B \approx 3 \text{ nm}$ ^[49] for the 1S-state of the exciton with $n = 1$. This value for the binding energy is close to the experimental values deduced from PL spectroscopy measurements at low temperatures in wurtzite GaN of 24.8^[50] and 25.2 meV^[51] for the free A exciton. Due to the high exciton binding energy, the recombination processes in GaN are dominated by excitonic recombination in the temperature regime between 10 and 300 K.

Radiative recombination of free excitons

The luminescence of free excitons in direct semiconductors is a rather complex process as the photon which is created by the radiative recombination of the electron and the hole during exciton annihilation is resonantly reabsorbed while traveling through the crystal. This re-absorption excites a new exciton and the process is constantly repeated. Due to this strong coupling, the exciton and the photon are no longer separate particles and should consequently be treated as a coupled system within the framework of quantum electrodynamics. The mixed exciton-photon state of the coupled system is then called *exciton-polariton*, a term introduced by Hopfield in 1958.^[52] A basic idea about polaritons and their luminescence can be obtained from the graphical representation of their dispersion curves $E(k)$ given in Fig. 2.3. The dispersion of an exciton is given by Eq. (2.4), i. e., essentially a parabola. The dispersion of a bare photon is $E(k) = \hbar ck$ and depicted by the straight, nearly vertical line in Fig. 2.3. In a coupled quantum system, the two dispersion relations exhibit an anti-crossing behavior, and new mixed states are formed in the vicinity of the anti-crossing point. These new states represent the coupled exciton-polariton and are called upper polariton branch (UPB) and lower polariton branch (LPB). The new eigenstates of the exciton-polariton are then referred to as light-like or exciton-like, depending on the relative weight of the respective wavefunctions.^[52] Additionally, a longitudinal-transversal splitting Δ_{LT} between the UPB and LPB is introduced which directly depends on the oscillator strength of the exciton.^[54]

2. Fundamentals

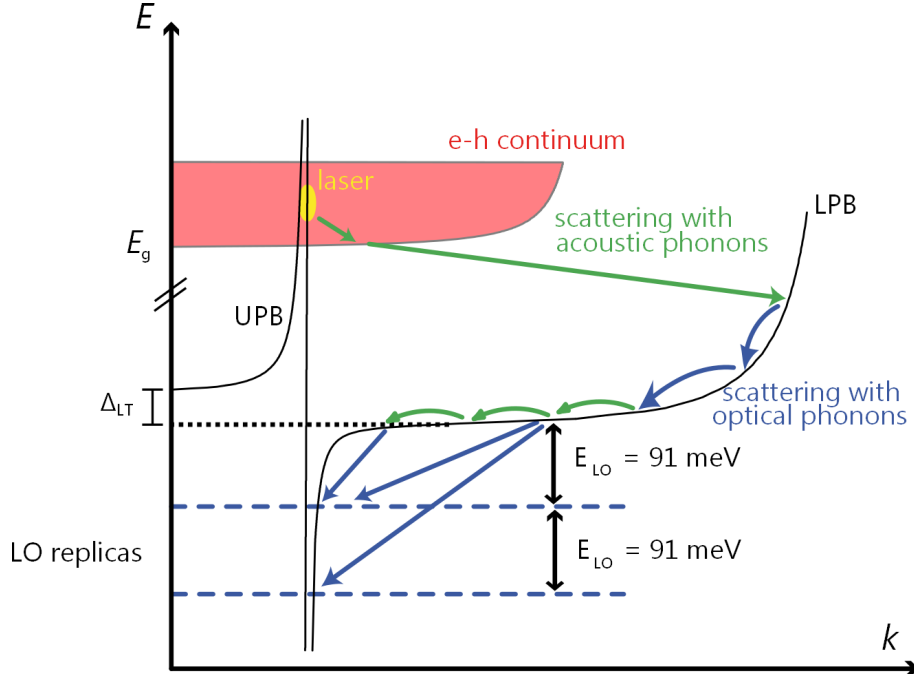


Figure 2.3: Schematic representation of the exciton-polariton dispersion assuming only one exciton branch. Electrons and holes excited by the laser form free exciton-polaritons through the emission of acoustic phonons. Subsequently, exciton-polaritons with a high kinetic energy (high k -vector) relax through the emission of optical and acoustic phonons (blue and green arrows, respectively) towards the photon-dispersion line. The recombination of exciton-like polaritons gives rise to the emission at the bottleneck energy minus n -times the LO phonon energy, with n being an integer. (Adapted with permission from Ref. 53)

After the free carriers have formed free excitons, the latter have a large kinetic energy and can thus not decay radiatively. The radiative decay is forbidden because only free exciton-polaritons, which have light-like eigenstates with $k \approx 0$, couple to photons. This inability to decay radiatively is due to the fact that the photon wavevector $2\pi/\lambda$ is negligible compared to the characteristic dimension of the Brillouin zone $2\pi/a$, i. e., the photon is not able to carry enough momentum. Instead, the exciton-polaritons relax towards the minimum of the polariton branch via the emission of phonons as depicted schematically in Fig. 2.3. This lowers their kinetic energy and transforms their eigenstates to more photon-like states. However, once their kinetic energy is below 92 meV which corresponds to the energy of a longitudinal optical phonon in GaN,^[55] they can only further reduce their energy via the emission of acoustic phonons. This process is very inefficient as the exciton-acoustic phonon scattering rate is much lower than the scattering rate of excitons with LO phonons.^[56] Additionally, the density of final states is reduced due to the small mass of photon-like polaritons. One consequence of this so-called *bottleneck* is that the thermalization of free excitons to the lattice temperature is slower than

2.2. Recombination processes in bulk GaN and GaN nanowires (NWs)

expected.[†]

In the specific case of GaN, the exciton-polariton behavior is more complex than depicted in Fig. 2.3 as several exciton branches exist due to the valence band splitting [cf. Fig.2.1(b)], and all these branches have a different coupling strength to photons.^[58] Thus the splitting between the UPB and LPB can only be observed in PL spectroscopy for samples with a very high structural perfection and purity. However, the optical transition stemming from the recombination of free A and B excitons are clearly observed in both, photoluminescence and reflectance measurements. The first spectroscopic investigations of excitons in GaN date back to the 70s and were performed by Dingle *et al.*^[23] Figure 2.4 shows a PL and reflectance spectrum of a free-standing GaN layer with a dislocation density of 10^6 cm^{-2} and a residual doping density below 10^{16} cm^{-3} . The resonances in the reflectance spectrum at 3.479 and 3.484 eV stem from the free A and B exciton, respectively. The transition denoted with (D^0, X_A) in the PL spectrum of Fig. 2.4 represents the recombination of a donor-bound exciton complex and is discussed in detail in the following section.

The discussed features, in combination with the fast trapping of excitons at impurities (which is discussed in the following subsection), leads to the situation that the radiative lifetime τ_{rad} of the free exciton at low temperatures is extremely difficult to access and thus essentially unknown. However, based on the intensity ratio between the free and bound exciton at low temperatures, a lower limit of 10 ns has been estimated for the radiative lifetime of the free exciton at $T = 10 \text{ K}$.^[59] In a crystal with a three-dimensional density of states, τ_{rad} is expected to increase with temperature proportional to $T^{3/2}$.^[60] It is thus expected that the radiative lifetime exceeds values of $\tau_{\text{rad}} > 1 \mu\text{s}$ at $T = 300 \text{ K}$. Consequently, even the longest values for the lifetime of free excitons found in state-of-the-art planar GaN layers of 40 ns at 300 K have been attributed to almost pure nonradiative recombination.^[61] Further details on the involved nonradiative processes in GaN are discussed in Sec. 2.2.2.

Excitons bound to neutral shallow impurities

Semiconductor crystals are usually not completely free of impurities. Even one of the purest semiconductors, namely, Si, exhibits typically an impurity concentration of at least 10^{11} cm^{-3} . In the case of unintentionally doped GaN grown by molecular-beam epitaxy, values of 10^{16} – 10^{17} cm^{-3} are typically found. However, due to their nanoscopic volume, very small GaN NWs are actually on the edge of being truly impurity-free.[‡] The most abundant impurities found in GaN are Si and O, which form shallow donors when they substitute a N and Ga atom in the crystal, respectively. Shallow acceptors in GaN include C and Mg, and especially the latter is observed in material grown by MBE due to a

[†]As an example for the magnitude of this effect: Photoluminescence spectra revealed an effective carrier temperatures of $T_c = 14.4 \text{ K}$ for GaAs although the sample was dispersed in a bath of liquid He with $T = 1.8 \text{ K}$.^[57]

[‡]cf. Ref. 62 and Chap. 4 for further details on this point.

2. Fundamentals

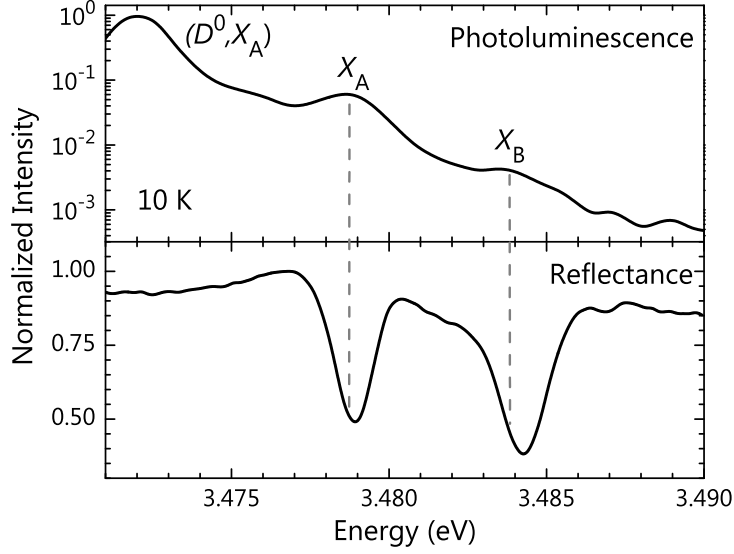


Figure 2.4: Low-temperature photoluminescence and reflectance spectra of a free-standing GaN layer (the data have been recorded by K. Ubben).

memory effect if the same machine has been used to grow p-doped GaN previously.

Shallow donors and acceptors in semiconductors can be treated as hydrogenic impurities characterized by a ionization energy E_I of the bound electron and hole, respectively:[§]

$$E_I = -\frac{m_e^* e^4}{32\pi^2 \hbar^2 \epsilon^2 n^2}. \quad (2.6)$$

The ionization energy E_I of Si and O donors is about 33 and 32 meV, respectively, which is small compared to the bandgap of GaN and thus both impurities introduce energy levels slightly below the conduction band. Neutral donors and acceptors are effective traps for free excitons. The free exciton, which we denote as X_i (here, the index i denotes the valence band from which the hole is originating) loses its kinetic energy owing to localization at these traps and forms a bound exciton complex. This complex is characterized by a binding energy E_{DX} , which was found to be proportional to the ionization energy of the impurity ('Haynes rule').^[63] In general, both neutral [(D^0, X) and (A^0, X)], as well as ionized [(D^+, X) or (A^-, X)] bound-exciton complexes can exist inside a given semiconductor material.[¶] However, it turns out that the latter represents a stable complex only for a certain m_e^*/m_h^* -ratio.^[64,65] Whether or not a stable (D^+, X) complex exists in GaN is still under debate, but appears unlikely at present.

[§]Neutral acceptors can be treated in a similar fashion as neutral donors when the effective electron mass m_e^* is exchanged with the effective hole mass m_h^* and the sign of the elementary charge e is multiplied with (-1).

[¶]Throughout this thesis, an index on the 'X' indicating the valence band of the hole, i. e., (D^0, X_A) rather than (D^0, X) , is only given when necessary.

2.2. Recombination processes in bulk GaN and GaN nanowires (NWs)

Radiative recombination of bound excitons

The recombination of a bound exciton complex, for example the (D^0, X_A) state, can occur via radiative or nonradiative recombination channels. In this section, we focus on radiative channels while nonradiative recombination in general is discussed in Sec. 2.2.2.

The lifetime of donor- and acceptor-bound excitons was experimentally found to be much shorter than the one of free excitons, which has been explained by the so-called 'giant oscillator strength' of bound excitons.^[66] Additionally, the population of bound excitons is much higher than the one of free excitons at low temperatures due to the fast trapping of the latter. The combination of both effects results in a high luminescence efficiency of bound exciton complexes and consequently, low-temperature (10 K) PL spectra of GaN are typically dominated by the recombination of bound excitons as depicted in Fig. 2.4.^[67,68] Upon increasing the sample temperature, the bound excitons get subsequently delocalized by thermal activation and free excitons start to dominate the PL spectrum. The activation process follows an Arrhenius process and depends on the binding energy E_{DX} of the complex. Note that acceptor-bound excitons in GaN have a larger binding energy than donor-bound excitons [typically 11 meV for the (A^0, X_A) compared to about 7 meV for the (D^0, X_A)].

The most commonly observed lines in PL spectra of unintentionally doped GaN are the transitions stemming from the recombination of A excitons bound to neutral oxygen [(O^0, X_A)] and silicon [(Si^0, X_A)] donors,^[68] with transition energies of 3.4714 and 3.4723 eV, respectively.^[22] However, the exact position of these lines depends on the residual doping density.^[69] All (D^0, X_A) states additionally exhibit excited rotational states with consequently larger transition energies, which can be observed in high resolution spectroscopy of very pure homoepitaxial GaN.^[21,50] High resolution, low-temperature, near-band edge spectra of homoepitaxially grown GaN layers revealed several bound exciton lines with a linewidth below 100 μeV .^[50]

So far, we only considered a direct radiative recombination of the bound exciton, in which the neutral donor is left behind in its ground state and a photon with energy $E_g - E_{FX} - E_{DX}$ is emitted. Besides this direct process, the excitation of the bound state can be partially transferred to the electron of the neutral donor, leaving the donor behind in an excited state after the recombination of the exciton.^[70] This process is called the two-electron satellite (TES) transition of the (D^0, X) . The emitted photons from a TES process have thus a reduced energy, which manifests itself by various narrow lines around 3.45 eV in the low-temperature PL spectra of GaN.^[21,22,50,71]

In contrast to the free exciton, the bound exciton complex is a localized state without any kinetic energy. Consequently, the line corresponding to the recombination of a bound exciton does not broaden with increasing temperature and exhibits a radiative lifetime which does not depend on the temperature. Still, the values assumed to reflect the radiative lifetime of the donor-bound excitons have evolved significantly during the last years. In 2006, the radiative lifetime of donor-bound excitons in GaN was believed

2. Fundamentals

to be 300 ps, and this value was determined by low-temperature (1.8 K) TRPL measurements on thick ($> 300 \mu\text{m}$) samples grown by hydride-vapor phase epitaxy (HVPE).^[72] It was also pointed out that the decay time of the (D^0, X) is very similar to the free exciton decay at elevated temperatures, as expected for a thermalized system.^[72] Later, in 2010, a radiative lifetime of at least 1 ns was determined for both the (Si^0, X_A) and (O^0, X_A) state by transient PL spectroscopy of the respective LO-replica lines on thick HVPE-grown bulk GaN.^[22] The difference to the previous value probably originates from an improved material quality due to a reduction in the dislocation density [cf. Sec. 2.2.2]. It was also pointed out that the no-phonon lines of these transitions exhibit a non-exponential decay curve and it was supposed that the initial decay is caused by a scattering process near the surface involving bound and free excitons.^[22] In planar structures, the situation is further complicated by the fact that the excitation intensity is exponentially decreasing inside the layer due to the absorption of the laser by the material and the impact of nonradiative surface recombination.^[61]

Summing up, the decay dynamics of bound excitons in planar GaN is still under investigation and so far, a minimum value for the radiative lifetime of the (D^0, X_A) of 1 ns has been determined for GaN layers with state-of-the-art quality.^[21,22] Yet, to our knowledge no consistent physical explanation has been established for the variety of recombination dynamics behavior found for bound and free excitons in this material.

Specific properties and optical transitions observed for GaN NWs

GaN nanowires (NWs) exhibit a high degree of structural perfection, i. e., they are usually free of extended defects, especially dislocations, independently of the substrate.^[40,73–75] Furthermore, they are free of strain on a macroscopic scale even when grown on lattice-mismatched substrates due to their small footprint following the principle of St Venant.^[76–78] More details regarding the growth and the different sources of strain in GaN NWs are found in Sec. 3.1 and Sec. 4.1, respectively.

Typical GaN NWs grown by molecular-beam epitaxy have diameters in the range of 50 to 250 nm, which is much larger than the exciton Bohr radius of the free exciton in GaN of $a_B = 3 \text{ nm}$. Consequently, quantum confinement plays no role for the GaN NWs investigated within this thesis. Even for GaN NWs with diameters as low as 15 nm, no sign of quantum confinement, which would manifest itself, for example, in a blueshift of the transition energies in PL spectra, was found in recent investigations.^[79]

Yet, GaN NWs differ significantly from planar layers as they exhibit a much larger surface-to-volume ratio. The free surface at the NW sidewalls gives rise to a number of additional effects which influence their electrical and optical properties. Photoconductivity measurements on GaN NWs revealed a pinning of the Fermi level at the NW sidewalls,^[80] which causes strong electric fields within the NW.^[81] The magnitude of these fields depends on both the doping and the NW diameter and can cause a complete depletion of the NW.^[82] However, it was shown that the Fermi level can be unpinned under

2.2. Recombination processes in bulk GaN and GaN nanowires (NWs)

continuous ultraviolet radiation for thin NWs with $d = 40$ nm due to the desorption of oxygen from the NW sidewalls,^[62] a process which also leads to a quenching of the PL intensity at room-temperature.^[83]

Additionally, the vicinity of a surface causes a change in the binding energy of the (D^0, X_A) state^[84,85] which inevitably leads to a broadening of the (D^0, X_A) transition when integrating over many donors with a random distribution inside the NW, for example when performing spectroscopy of GaN NW ensembles. In contrast, the bound exciton state in single GaN NWs was found to exhibit a linewidth below $250 \mu\text{eV}$ for specific samples,^[81,84] i. e., in a similar range than what has been observed for bulk GaN. Consequently, it has been pointed out that the optical properties of GaN NWs can be determined by single impurities for typical impurity concentrations if the NW volume is small enough.^[86] This inherent property of NWs is discussed in more detail in Chap. 4.

The low-temperature PL spectrum of typical MBE-grown GaN NWs is dominated by the recombination of the neutral donor-bound exciton, similar to what is observed for planar layers.^[84,87] However, several new, and partially unidentified lines are found in PL spectra of GaN NWs.^[81] In particular, additional transitions have been reported around 3.45 eV,^[88] where the intrinsic two-electron satellite (TES) of the (D^0, X_A) transition in GaN is expected,^[21,70]. In some case they are even dominating the PL spectrum and their origin is thus under debate for over a decade now.^[81,84,87,88] A relation of the lines around 3.45 eV with the NW surface was shown,^[84,87,89] but as the intensity of these lines can vary over orders of magnitude between samples with very similar surface-to-volume ratio, it is likely that more than one origin gives rise to the transition observed at 3.45 eV in GaN NWs. For example, acceptor-bound excitons have been reported in this energy range in planar GaN.^[67,90] For some GaN NW samples, a doublet at 3.452 and 3.458 eV has been observed,^[88] and the energy difference between the two bands as well as very recent results regarding the temperature-induced quenching of the lines suggest a direct connection of these bands with the (D^0, X_A) and X_A states.^[91] Additionally, a frequently observed radiative transition in GaN NW PL spectra occurs around 3.42 eV, and is attributed to the recombination of excitons bound to I_1 -SFs [(I_1, X)]. The various properties of excitons bound to stacking fault in GaN are described in detail in a recent review.^[38] In state-of-the-art MBE-grown GaN NW samples, the PL intensity of this (I_1, X) band is at least two orders of magnitude lower than the near-bandedge luminescence.

Because of the absence of threading dislocations, exciton recombination in GaN NWs is assumed to be predominantly radiative.^[92] However, this expectation is inconsistent with the experimentally observed short decay times of bound excitons in GaN NWs. Even at low temperatures, time-resolved photoluminescence (TRPL) measurements yield typically \parallel decay times in the range of a few tens to about 200 ps,^[79,88,89,94–96] which is significantly shorter than the radiative lifetime of the bound exciton state in bulk GaN of

^{||}With the sole exception of the work by Schlager *et al.*, who determined decay times between 500 ps and 1 ns for GaN NWs with exceptionally large dimensions (up to $22 \times 1.2 \mu\text{m}^2$) and using very high excitation densities (up to $190 \mu\text{J}/\text{cm}^2$).^[93]

2. Fundamentals

at least 1 ns.^[21,22] Since NWs inevitably possess a large surface-to-volume ratio, it is often suspected that nonradiative surface recombination causes these fast decay times.^[89,94–97]

However, photoluminescence (PL) transients obtained for GaN NWs in time-resolved experiments do not generally exhibit a monoexponential decay as expected for a single excitonic transition. Instead, bi- and nonexponential transients were obtained,^[89,96–98] which impede the extraction of a single lifetime.** This nonexponential decay was attributed to surface-related effects by different groups.^[89,94,96,99,100] However, it should be kept in mind that the active surface in the case of a planar GaN layer is the C-plane while the free surface in GaN NWs consists of *M*-plane facets.

Summing up, as of today, there is no satisfactory understanding of the exciton dynamics in GaN NWs at low temperatures which impedes extracting their internal quantum efficiency as will be discussed in the following.

2.2.2. Nonradiative processes and internal quantum efficiency

Besides the various possibilities of radiative recombination in direct semiconductors, there are several nonradiative recombination channels which influence the recombination dynamics of excitons and reduce the quantum yield.^[20] The most important nonradiative processes present at low excitation densities is the undesired transformation of excitation into heat (phonons).

Nonradiative processes are challenging to investigate by means of optical spectroscopy as there is no photon emitted in the process. Nonradiative recombination can occur spontaneously via an Auger process, but is often mediated by a nonradiative defect and is, in its most simple form, called Shockley-Read-Hall recombination.^[101,102] Defect types which cause this nonradiative recombination include structural defects of the material, for example dislocations, deep point defects like vacancies, or surface states. Mid-gap states are particularly efficient centers for nonradiative recombination of excitation.

Depending on its nature and dimension of the nonradiative defect, the nonradiative defects may be directly visualized by spatially resolved cathodoluminescence spectroscopy. For example, by a combined cathodoluminescence and transmission electron microscopy (TEM) study, dislocations were identified as centers of nonradiative recombination in planar GaN.^[103] Consequently, a reduction of the dislocation density in planar GaN layers was pursued for many years in order to improve the quantum yield of these structures. However, if the dislocation density is low enough, nonradiative point defects have been identified to limit the recombination time and thus the internal quantum efficiency of GaN layers.^[61]

In addition to the deep-level recombination at dislocations or nonradiative point defects, an important channel for nonradiative recombination in semiconductor crystals is the surface. At a semiconductor surface, a high density of dangling bonds provides efficient centers for nonradiative recombination. The magnitude of this effect is de-

** Analogous observations were made for ZnO NWs.^[99,100]

2.2. Recombination processes in bulk GaN and GaN nanowires (NWs)

scribed by a surface recombination velocity. To exemplify this phenomenon, let us consider generation, diffusion, and recombination of excitons described by the diffusion-recombination equation

$$\frac{\partial n(\mathbf{x}, t)}{\partial t} = D\Delta n(\mathbf{x}, t) - \gamma n(\mathbf{x}, t) + G\delta(t) \quad (2.7)$$

with the initial condition $n(\mathbf{x}, 0) = 0$ and the boundary condition

$$D \frac{\partial n(\mathbf{x})}{\partial x} \Big|_{x=0} + S n(\mathbf{x}) \Big|_{x=0} = 0. \quad (2.8)$$

Here $n(\mathbf{x}, t)$ is the exciton density, G the generation rate, D the diffusion coefficient and γ the radiative recombination rate. The surface recombination velocity S determines the value of the derivative of the exciton concentration at the surface, i. e., at $x = 0$.

While some semiconductors such as GaAs, have an extremely high surface recombination velocity of $S \approx 10^6$ cm/s,^[64] much lower values are reported for GaN. In C-plane layers, a value of $S = 5 \times 10^4$ cm/s was obtained at 300 K,^[104] while for GaN NWs a value of $S = 9 \times 10^3$ cm/s^[105] was found. At low temperatures (10 K), an effective surface recombination velocity $\tilde{S} = 6 \times 10^3$ cm/s has been derived for donor-bound excitons by time-resolved measurements on thin GaN NWs with diameters between 20 and 80 nm.^[96] While it seems plausible to assume that the luminescence dynamics in thin GaN NWs is governed by nonradiative surface recombination, long carrier lifetimes are expected for thicker NWs as surface recombination causes the lifetime of free excitons to directly scale with the NW diameter.^{††} This effect was confirmed for free excitons at 300 K in GaN NWs with diameters $d > 500$ nm and lengths exceeding 10 μm by one study.^[105]

An indirect way of studying nonradiative recombination in semiconductors is time-resolved photoluminescence (TRPL) spectroscopy. Independent of the origin of the luminescence, we can define an effective decay time $\tau_{\text{eff}} = \gamma_{\text{eff}}^{-1}$ given by the superposition of radiative (denoted by a rate γ_r) and nonradiative recombination (γ_{nr}) of the respective state:

$$\gamma_{\text{eff}} = \gamma_r + \gamma_{\text{nr}} \quad \text{and thus} \quad \tau_{\text{eff}} = \left(\frac{1}{\tau_r} + \frac{1}{\tau_{\text{nr}}} \right)^{-1}. \quad (2.9)$$

The internal quantum efficiency η_{int} is then defined as the ratio of effective and radiative lifetime of a state:^[20]

$$\eta_{\text{int}} = \frac{\gamma_r}{\gamma_r + \gamma_{\text{nr}}} = \frac{\tau_{\text{eff}}}{\tau_r} \leq 1. \quad (2.10)$$

^{††}This fact is derived, for example, in the appendix of Ref. 106

2. Fundamentals

2.3. Absorption and extraction of light in planar layers and NW ensembles

The efficiency of light-emitting devices such as lasers and diodes is not only governed by the internal quantum efficiency of the optically active material, but in addition by the external quantum efficiency η_{ext} of the device. If we consider the external quantum efficiency of a sample in a photoluminescence experiment, we additionally have to take into account the generation of electrons and holes in the material as well as the extraction of photons from the structure. The generation of an excitation can occur either electrically as in light-emitting diodes (LEDs) or lasers, thermally, mechanically or optically. As we investigate GaN NWs with optical spectroscopy within the present thesis, the case of optical excitation shall be investigated in more detail here.

Absorption and extraction in planar layers

The process of absorption, transmission and reflection of light through and around objects whose dimensions are much greater than its wavelength is adequately described by ray optics.^[107] Consequently, all of the above quantities are depending solely on the complex refractive index of the material. For example, the reflection of monochromatic light at the surface of a given material with complex refractive index \tilde{n} embedded in air ($|n| \approx 1$) at normal incidence is given by:

$$R = \left| \frac{\tilde{n} - 1}{\tilde{n} + 1} \right|^2. \quad (2.11)$$

All light which is not reflected is consequently absorbed inside the material or transmitted. The absorption A of monochromatic light with intensity I_0 in opaque materials can be described by Beer's law:

$$I(z) = I_0 e^{-\alpha z} \quad (2.12)$$

where $I(z)$ is the remaining intensity at a depth z inside the material.

The extraction of light from a planar layer into air is typically highly inefficient due to the small escape cone of the emitted photons. The escape cone is defined by the critical angle $\beta = \arcsin(1/n)$ and the extraction efficiency can thus be approximated by:

$$\eta_{\text{extr}} = \frac{1 - \cos(\beta)}{2} \quad (2.13)$$

The extraction efficiency of planar structures can be enhanced in a multitude of ways in order to improve η_{ext} for LEDs. One approach is to choose a device geometry that increases the escape cone of the light, such as hemispherical domes or inverted truncated

2.3. Absorption and extraction of light in planar layers and NW ensembles

pyramids. Other approaches include statistical surface roughening or the use of photonic crystals^[108] to enhance the extraction efficiency of LEDs.^[109]

Absorption and emission of light in NW ensembles

Nanowires exhibit typical cross-sectional diameters between a few tens and several hundred nanometers and lengths of a few hundred nanometers to several micrometers. Their dimensions thus overlap with the wavelength of electromagnetic waves in the near-infrared to near-ultraviolet region. Obviously, ray optics does no longer provide an appropriate description of the interaction of light with these nanostructures.

Under certain conditions, effective medium theory provides a convenient means to simplify the complex behavior of NW-light interaction. In the Maxwell-Garnet effective medium approximation (EMA),^[110] a NW ensemble with filling factor f which consists of NWs with dielectric constant ϵ_{NW} embedded in air (ϵ_{Air}), is described by the homogeneous, effective refractive index n_{eff} :^[111]

$$n_{\text{eff}} = \sqrt{\epsilon_{\text{eff}}}, \quad \text{where} \quad \frac{\epsilon_{\text{eff}} - \epsilon_{\text{Air}}}{\epsilon_{\text{eff}} + \epsilon_{\text{Air}}} = \frac{\epsilon_{\text{NW}} - \epsilon_{\text{Air}}}{\epsilon_{\text{NW}} + \epsilon_{\text{Air}}} f. \quad (2.14)$$

The simplicity of this approximation lies in the fact that f is the parameter fully characterizing the NW ensemble (note that the filling factor is equal to the area coverage of the NW array for vertical, not tapered NWs). It is thus possible to employ standard ray and wave optics formula to calculate the absorbance, reflectance and transmittance of a NW ensemble. The EMA works best for low values of f , but there is no strict limit of validity. The Maxwell-Garnett EMA has been successfully employed to interpret Raman scattering data of spontaneously formed GaN NW ensembles,^[112,113] and to predict the extraction efficiency of a NW ensemble.^[114] However, other reports state that the effective medium description fails to describe important features in the interaction of NWs with electromagnetic waves.^[115,116] For example, it has been demonstrated that light scattering has to be taken into account when the optical wavelength becomes comparable with the diameter of the NWs. The Rayleigh limit is valid for particle diameters $d < \lambda / (\pi n)$, which for $n = 2.6$, sets the critical diameter for GaN NWs to about 50 nm, a typical value for spontaneously grown GaN NWs. For NWs thicker than the critical diameter, light scattering strongly contributes to the nanowire optical properties, which for a dense collection results in diffuse transport of light.^[117] Another recent article describes the interaction of light with NWs by Mie-scattering.^[118]

It is thus not straightforward to decide under which circumstances a given approximation is applicable for the interaction of NWs with optical waves in the visible to near ultra-violet spectrum. In fact, the validity of the various approximations are still under scrutiny. Consequently, the calculation of the absorption and extraction efficiency of NW ensembles in general requires a full three-dimensional solution of the Maxwell equations for the exact geometry of the given NW array. This task which is extremely challenging

2. *Fundamentals*

for spontaneously grown NW samples with broad diameter distributions and a random arrangement of the NWs, but to some extent manageable for strictly ordered NW arrays grown by selective-area growth.

Experimental and numerical methods

The chapter begins with a brief description of the spontaneous formation and selective-area growth of GaN NWs on Si substrates by molecular-beam epitaxy in Sec. 3.1. Subsequently in Sec 3.2 and 3.3, the experimental setups used for continuous-wave and time-resolved micro-photoluminescence spectroscopy of GaN NWs are described, the spectral and spatial resolution of the setups are discussed and the principal data analysis is explained. Finally, in Sec. 3.4 the numerical methods which are the basis for the software tools used to simulate the absorbance and extraction efficiency of ordered GaN NW arrays are introduced.

3.1. GaN NWs fabricated by spontaneous formation and selective-area growth

Spontaneous formation of GaN nanowires

The spontaneous formation of NWs lifts one of the most fundamental constraints of planar epitaxy, namely, finding a suitable substrate for growth. For example, the compound semiconductor GaN can be grown in the form of NWs with a low density of structural defects on a wide variety of substrates such as Si^[73,119–123], diamond^[124], SiC^[125], AlN^[126], amorphous Si_xO_y^[127] and Al_xO_y^[128]. The first demonstration of spontaneously formed GaN NWs by molecular-beam epitaxy (MBE) was reported in 1997 by the groups of K. Kishino^[128] and shortly after by E. Calleja.^[119]

During the last years, the understanding of the underlying mechanism of the formation of GaN NWs by MBE has significantly improved.^[129] Note that some of the groundbreaking investigations during the last years regarding the formation and growth mechanism of GaN NWs have been performed at the *Paul-Drude-Institut*. In contrast to the well-known vapor-liquid-solid growth mechanism of semiconductor NWs,^[130] where the growth is mediated by a metal particle, the nucleation of GaN NWs in MBE occurs

3. Experimental and numerical methods

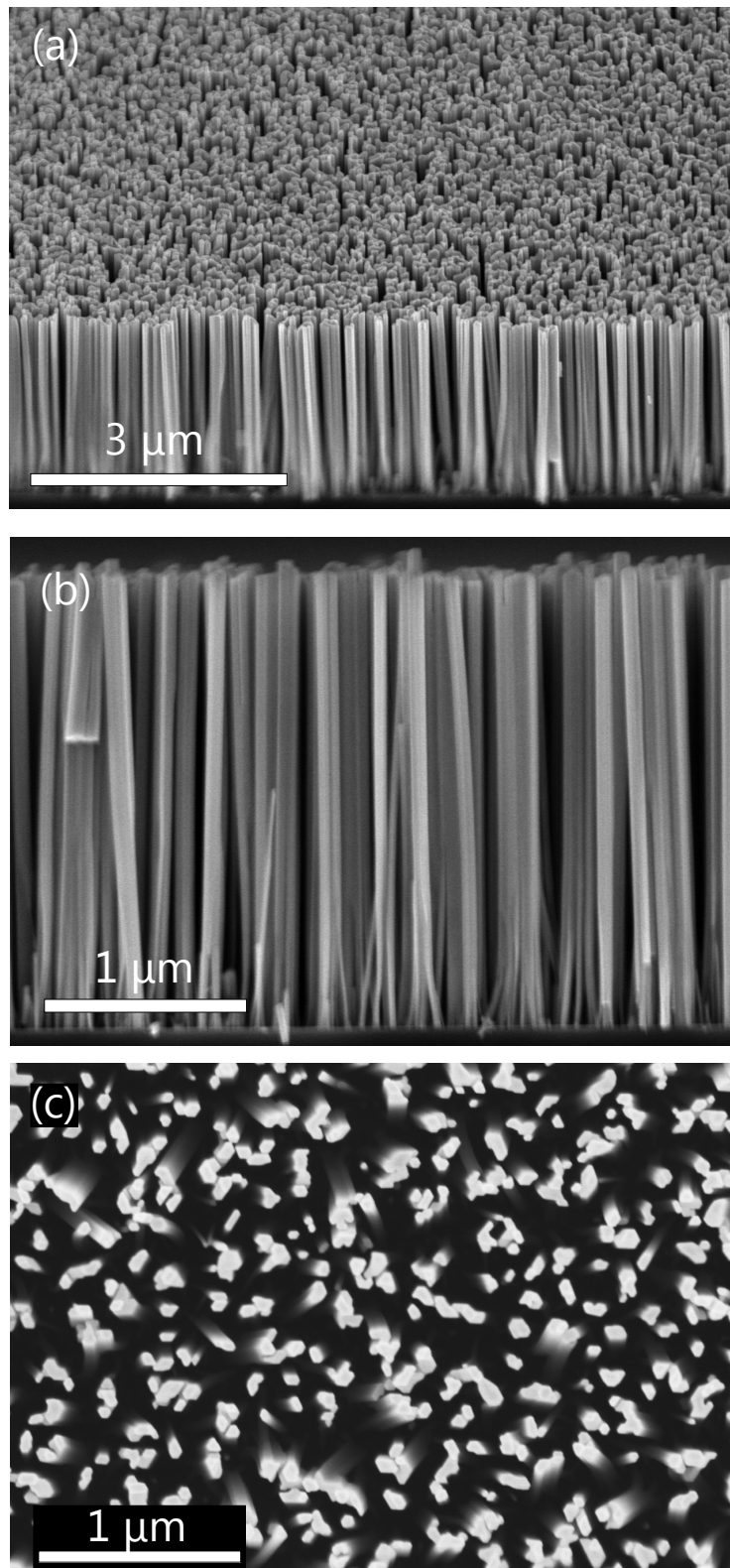


Figure 3.1: Scanning electron micrographs of a typical, spontaneously formed GaN NW ensemble on Si(111) (sample R) taken under different angles: (a) 120° ('bird's eye view'), (b) 90° ('side view') and (c) 180° ('top view') with respect to the growth direction of the wires. The images have been taken by A.-K. Bluhm.

3.1. GaN NWs fabricated by spontaneous formation and selective-area growth

spontaneously under specific conditions.^[122,131] Yet, the nature of this spontaneous formation mechanism is still under investigation. The first growth diagram for GaN NWs was presented in 2009,^[132] and a high substrate temperature and growth under nitrogen excess, i. e., a III/V ratio smaller than one, were identified as the principal requirements for the spontaneous formation of GaN NWs by MBE. It was recently found that GaN NWs grown by MBE are always N-polar when formed in the absence of surface defects.^[131] Since all spontaneously formed GaN NW ensembles investigated in this thesis were grown on Si(111) substrates, we restrict the following description of the nucleation and growth mechanism of GaN NWs to this specific case.

The current understanding of spontaneous GaN NW formation by MBE can be summarized in four steps. During the nucleation stage, the supplied Ga atoms diffuse along the substrate surface, until a certain number of atoms agglomerate and react with the N atoms supplied by the plasma source to form stable GaN nuclei on the surface.^[121,123] Under continuous Ga and N flux, these nuclei undergo a shape transformation once they reach a certain critical radius, forming a hexagonal GaN NW with the $\langle 0001 \rangle$ -direction of the wurzite crystal perpendicular to the substrate surface.^[133] When proceeding with the growth, the NWs start to elongate axially and at the same time grow radially up to a self-limiting diameter which is determined by the III/V-ratio.^[126] Afterwards, the NWs grow mainly axially upon further supply of material, and the final NW length is determined by the growth time. However, due to the statistical nature of the nucleation process^[134] and the influence of collective effects such as desorption and adsorption at the NW sidewalls^[135] as well as shadowing during growth, the final NW ensemble contains a statistical distribution of NW lengths and diameters as can be seen in the scanning electron micrographs depicted in Fig. 3.1. The presented GaN NW ensemble (hereafter called sample R) has a NW density of $5 \times 10^9 \text{ cm}^{-2}$, and the NWs have a length of $(2.3 \pm 0.1) \mu\text{m}$. Employing scanning electron micrographs of the as-grown GaN NW ensembles enables us to extract the NW diameter distribution and the coalescence degree of the ensemble as described in detail in App. A.

All spontaneously formed GaN NW samples investigated in this thesis have been grown at the *Paul-Drude-Institut* using several different MBE machines. An overview of the growth conditions of all NW samples studied in this thesis can be found in App. B.

Selective-area growth of GaN nanowires

The statistical fluctuations in dimensions found for spontaneously formed GaN NW ensembles [cf. App. A] as well as their high density induce a number of difficulties for their integration into optoelectronic devices such as LEDs.^[136,137] It is thus desirable to actively control the nucleation density and diameter of GaN NWs in order to improve, for example, the homogeneity in emission color of NW-based LEDs.^[138]

Selective-area growth (SAG) is one method to achieve large arrays of GaN NWs with controlled dimensions and density. The basic principle of SAG relies on a different nucle-

3. Experimental and numerical methods

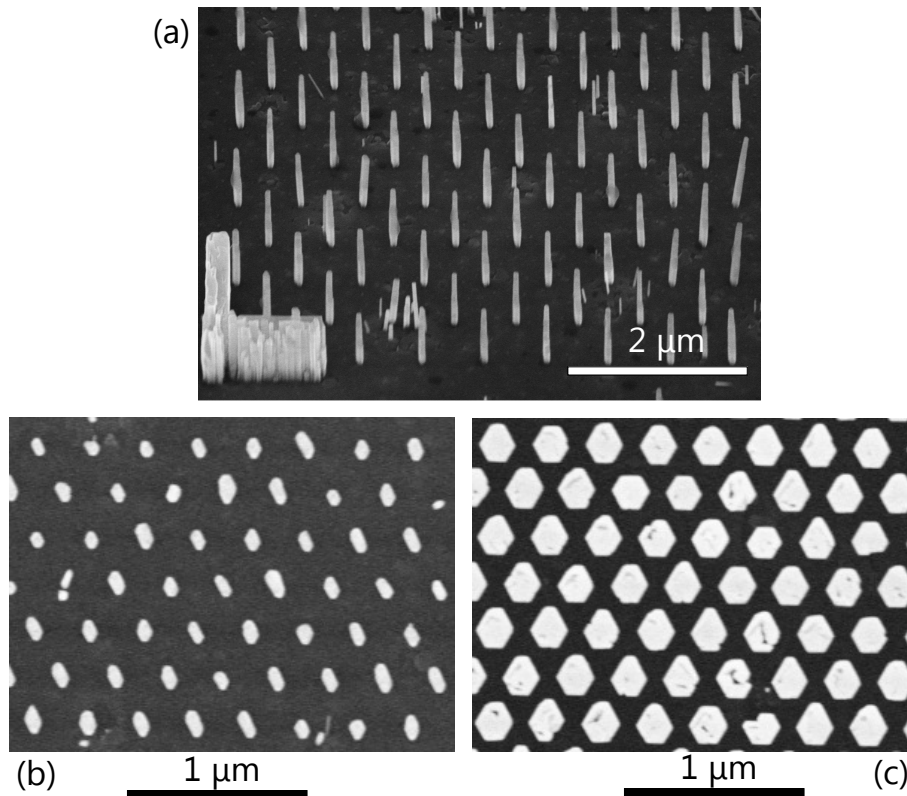


Figure 3.2: (a) Bird's eye view scanning electron micrograph of a NW array grown on a mask with a nominal hole size of 50 nm and a pitch of 700 nm. (b) and (c) Top-view scanning electron micrographs of two SAG NW arrays after growth using a mask pattern with a pitch of 360 nm and holes sizes of 50 and 300 nm, respectively. The images have been taken by A.-K. Bluhm.

ation time of GaN NWs on various materials. This delay is much shorter on GaN, AlN, and Si as compared to Ti_xN_y , Si_xN_y , and Si_xO_y . Consequently, the latter materials have been successfully used as a mask to achieve SAG of GaN NWs on Si substrates.^[139–143] The desired arrangement of the NWs after growth is determined by the pattern which is written into the mask material by, for example, electron-beam lithography (EBL) or nanoimprint lithography.

The SAG samples under investigation in this thesis have been fabricated at the *Paul-Drude-Institut*.^[127] A thin (13 nm) AlN buffer layer has been grown by MBE on a Si(111) substrate before sputtering a Si_xO_y layer onto the surface, which serves as a mask for the NW growth. Subsequently, electron beam lithography has been used to write the desired pattern into the mask. The employed pattern contains nominal hole sizes between 30 and 300 nm and pitches, i. e., hole-to-hole distances, ranging from 0.3 to 3 μm in either a cubic or hexagonal arrangement. For the subsequent GaN NW growth, a substrate temperature of 825 °C and a III/V-ratio of 0.23 has been employed.

In Fig. 3.2(a), a bird's eye view image recorded by SEM of a representative example of

3.2. Continuous-wave μ -photoluminescence spectroscopy

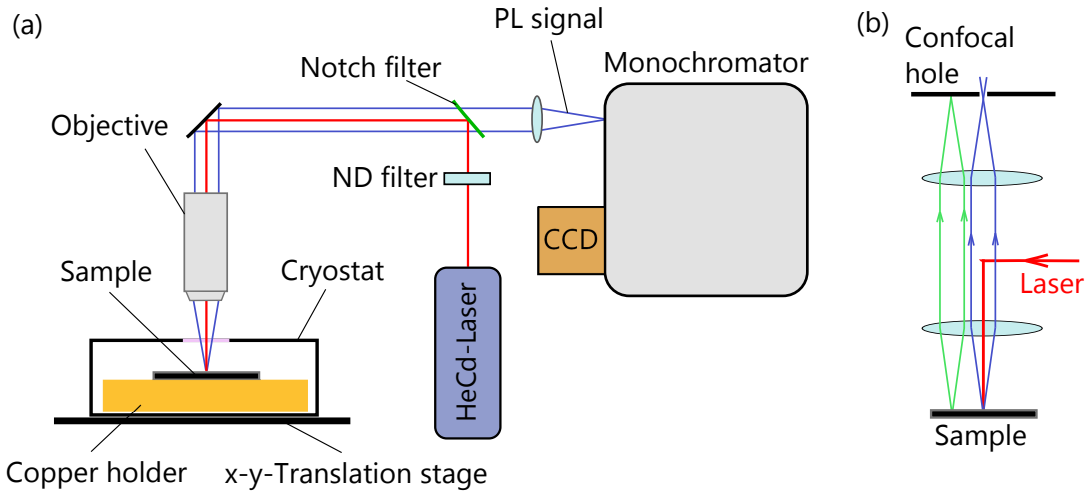


Figure 3.3: (a) Schematic diagram of the μ PL setup. (b) Principle of a confocal setup.

a GaN NW array with a hole size of 50 nm and a pitch of 700 nm is shown. Figure 3.2(b) and 3.2(c) present top-view scanning electron micrographs of two SAG NW arrays after growth using a mask pattern with a pitch of 360 nm and holes sizes of 50 and 300 nm, respectively. For the sample shown in Fig. 3.2, the NWs have a length of about 800 nm, while in general, the length is determined by the growth time. The final NW diameter, which is to some extent controlled by the size of the holes in the mask, has been found to be slightly larger than the nominal hole size due to imperfections in the EBL process and radial growth of the GaN NWs.^[127]

3.2. Continuous-wave μ -photoluminescence spectroscopy

Experimental setup

The cw spectra presented in this work have been measured using a HORIBA JOBIN YVON LABRAM HR 800 UV μ -PL setup, which is depicted schematically in Fig. 3.3(a). For the excitation of the samples, the 325-nm line of a KIMMON IK 3552R-G HeCd laser with a maximum output power of 30 mW is used. The beam is optionally attenuated by neutral density (ND) filters, deflected by a 325 nm-notch filter and focused onto the sample using microscope objectives optimized for the near ultraviolet (NUV) wavelength range. The PL signal is collected by the same objective, transmitted through the notch filter, and focused into a monochromator with a focal length of 80 cm. The monochromator is equipped with two gratings with 600 and 2400 grooves per mm, providing a spectral resolution of 1 and 0.25 meV, respectively, in the energy range of the near-band edge (NBE) luminescence of GaN. The spectrally dispersed PL signal is detected by a liquid nitrogen-cooled charged-coupled device (CCD, ISA SPECTRUM ONE) with 1024×256 pixels.

In order to perform PL measurements at low temperatures, the samples are mounted

3. Experimental and numerical methods

into a KRYOVAC cold finger cryostat, which is fixed on a motorized x-y-stage. If dispersed GaN NWs and samples produced by SAG are investigated, an ozone-cleaning procedure was performed.^[81] During this procedure, strongly oxidizing O radicals are formed, which react with residual hydrocarbons to form CO₂, H₂O, or CO. The method thus prevents the deposition of C from residual hydrocarbons on the sample surface which are cracked by the light of the UV laser. The ozone-cleaning proved to be very important for the samples grown by SAG, as they are exposed to various solvents during the pre-patterning of the mask and the sawing of the wafers into smaller parts after growth. Once the samples were mounted and ozone-cleaned, an isolating high vacuum with a pressure below 10⁻⁵ mbar (measured close to the pump) is generated by a turbo molecular pump. The cold finger inside the cryostat can be cooled with liquid helium to 10 K, and a resistive heating element inside the cryostat allows to continuously adjust the temperature between 10 and 300 K for temperature dependent PL measurements. When the temperature of the cold finger is adjusted, the samples mounted on the copper holder need some time to reach thermal equilibrium again. Consequently, for temperature-dependent measurements, a waiting time of at least 20 min is employed between the individual data acquisitions. This time is sufficiently long for the samples to adopt to the nominal temperature of the cryostat based on our experimental experience.

Excitation density and spatial resolution

Two different objectives were used for the μ -PL measurements, and their properties are summarized in Tab. 3.1. Due to losses in the optical path, the maximum laser power P_0 which can be used for excitation is $P_0 = 0.7$ mW (0.2 mW), measured after the 15 \times (50 \times) objective. The maximum excitation density at the sample surface is then calculated by $I_0 = 2P_0/(\pi\omega_0^2)$. Here, ω_0 denotes the waist of the Gaussian excitation beam, i.e. half the theoretical spot size in Tab. 3.1.

As the width of the HeCd laser beam is only about 2 mm, i.e., four times smaller than the entrance aperture of the 15 \times objective, the actual size of the focus is expected to increase by approximately a factor of 4 (this result is experimentally confirmed in

	Magnification	NA	Working distance (mm)	Theoretical spot size $2\omega_0$ (μm)	Entrance aperture (mm)	Peak excitation density I_0 using P_0 (kW/cm^2)
(1)	15 \times	0.32	8.5	1	8.5	10
(2)	50 \times	0.42	15	0.7	2	100

Table 3.1: Summary of the properties of the two microscope objectives employed for μ -PL measurements in this thesis: (1) Thorlabs LMU-15 \times -NUV and (2) Mitutoyo Plan APO NUV 50 \times . All values except the excitation density are supplied by the manufacturer. Note that I_0 in the case of the 15 \times objective, a more realistic spot size of 4 μm was assumed

3.3. Time-resolved μ -photoluminescence spectroscopy

Sec. 4.3).^[107] Taking the larger spot size into account, the denoted excitation densities in Tab. 3.1 certainly represent an upper limit. The excitation density can be further reduced by neutral density filters by up to seven orders of magnitude if necessary. The typical excitation density used for obtaining the low-temperature PL spectra of GaN NW ensembles presented in this thesis is $10^{-4}I_0$ to $10^{-5}I_0$, i. e., about 10 to 1 W/cm² using the 50 \times objective and assuming an optimal focus. The arrangement of the excitation and detection in the μ PL setup is designed as a confocal setup as depicted schematically in Fig. 3.3(b). The confocal pinhole is set to 100 μ m, and the diameter of the circular detection area is thus equal to 7 and 2 μ m for the 15 \times and 50 \times objective, respectively.

Signal processing and evaluation

The optical grating inside the monochromator correlates the intensity of the PL signal with the wavelength λ of the incident photons. This information is then imaged onto the chip inside the CCD camera. Since the analysis of recombination processes in semiconductors is based on the energy of the respective transition, the wavelength is converted to energy using the relation

$$E [\text{eV}] = \frac{hc}{n_{\text{air}}\lambda} \cong \frac{1239.489}{\lambda[\text{nm}]}, \quad (3.1)$$

where $h = 4.135667516(91) \times 10^{-15}$ eVs is Planck's constant,^[144] $c_0 = 299792458$ m/s the speed of light in vacuum^[144] and $n_{\text{air}} = 1.000285$ the refractive index of air in the NBE region of GaN ($\lambda = 360$ nm).^[145] The conversion factor in Eq. 3.1 provides an accuracy better than 10 μ eV in this energy range, limited by the refractive index of air. However, the accurate determination of transition energies by PL spectroscopy is limited by other factors of the setup. The main error is introduced by the absolute position and dispersion of the grating inside the monochromator. In order to correct this, a Hg and a Ne calibration lamp are used for a spectral calibration. Applying this method, the transition energies can be determined with an accuracy of approx ± 100 μ eV, depending on the full width at half maximum (FWHM) of the transition. Typical values for the dominating line in GaN NWs measured at low temperatures, the donor-bound exciton, are however on the order of 1 meV, thus much larger than the discussed error margins.

3.3. Time-resolved μ -photoluminescence spectroscopy

Experimental setup

Figure 3.4 schematically displays the setup used for TRPL measurements during the course of this thesis. As a main oscillator, a Kerr-lens passively mode-locked COHERENT MIRA 900 femtosecond Ti:sapphire laser pumped by a VERDI V10 solid-state laser is used. The Ti:sapphire laser is tuned to a central wavelength of 850 nm and emits pulses

3.3. Time-resolved μ -photoluminescence spectroscopy

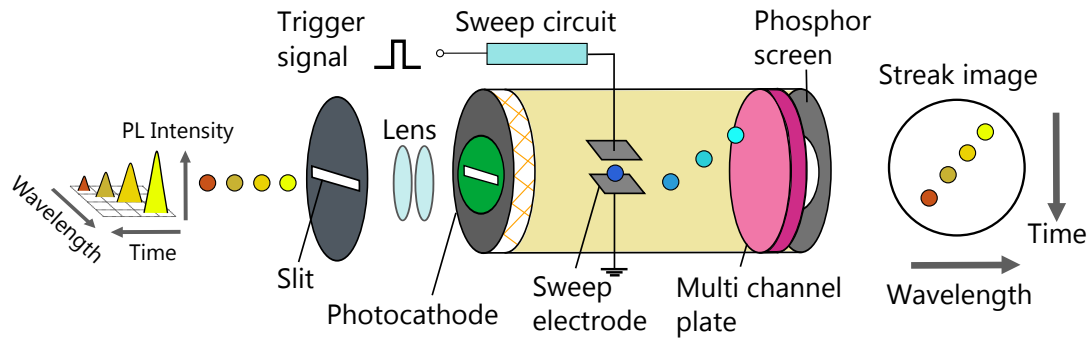


Figure 3.5: Schematic diagram of the concept of a streak camera. Adapted from Ref. 146

a camera and a flip mirror can be inserted into the detection path in order to image the sample surface and the laser spot simultaneously.

Figure 3.5 displays the principle functionality of the SC. The TRPL signal carries information about the intensity, wavelength, and emission time of the incoming photons and is focused onto a photocathode. The emerging electrons are accelerated and pass through the sweep electrodes where they are deflected by an electric field generated by a periodic sawtooth voltage. This voltage is generated by a sweep circuit which is triggered by the signal of a diode placed behind the Ti:sapphire oscillator. In this configuration, the delay at which photons arrive at the photocathode is translated into a time-dependent deflection of the emerging electrons, which pass through a multi channel plate (MCP), before the signal is detected on a phosphor screen. The temporal resolution carried by the incident photons has now been transferred into a spatial information on the phosphor screen. Finally, the streak camera image is generated by imaging the phosphor screen with a two-dimensional CCD array. Figure 3.6 shows an example of an SC image, which contains all relevant information from the incident photons, mapped as wavelength versus time on the x - y -axis and intensity as a color code. In the following section, the processing and evaluation of the images is described, which allows to extract PL transients and time-dependent spectra.

Excitation density

The typical cw equivalent power measured directly after the second SHG is typically about 4 mW at 325 nm. Optical losses between the second SHG and the cryostat limit the maximum fluence Φ_0 which can be used for excitation to about $20 \mu\text{J}/\text{cm}^2$.

3. Experimental and numerical methods

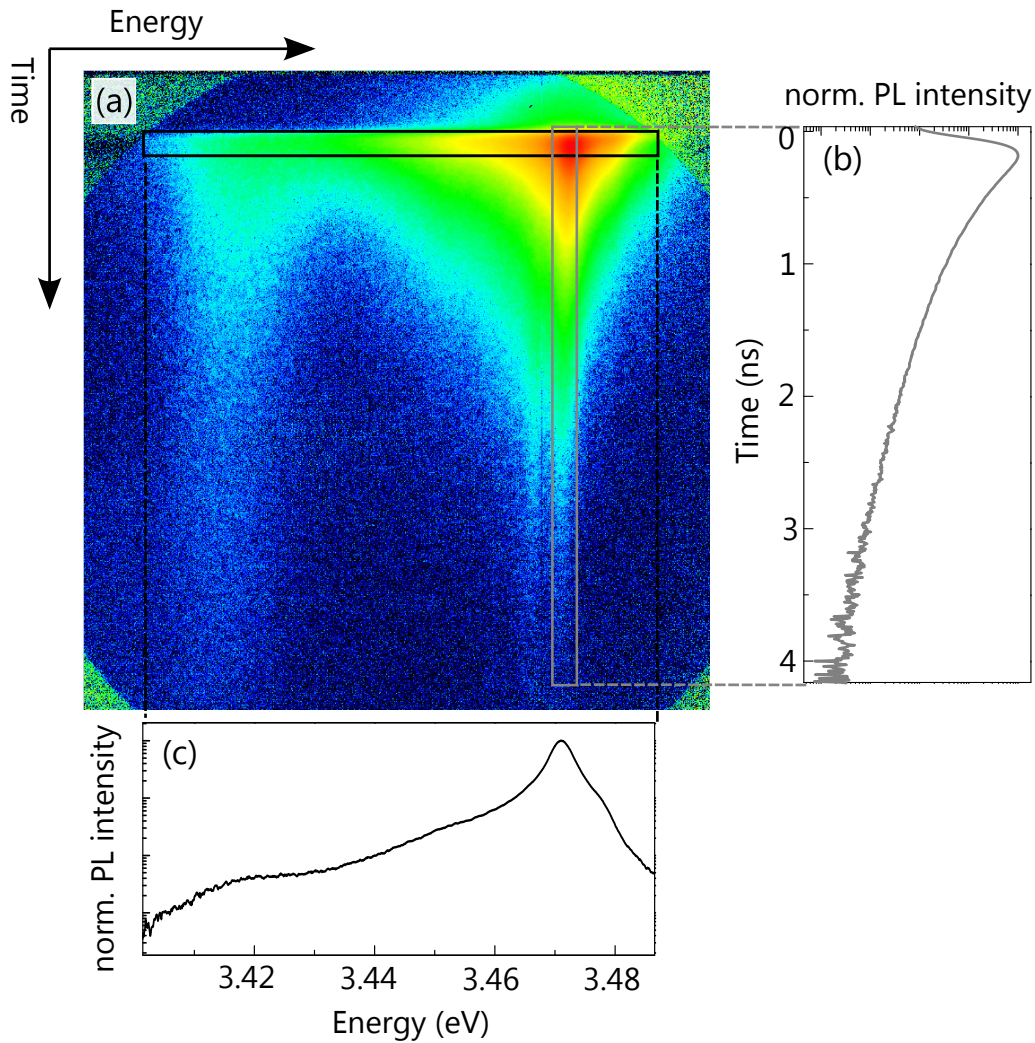


Figure 3.6: (a) Example streak camera image after subtraction of the electronic and optical background, shading correction and conversion from wavelength to energy. The intensity scale is color coded from red (high) to blue (low) intensity on a logarithmic scale. (b) Transient obtained by spectrally integrating the area denoted by the grey box in (a). (c) Spectrum obtained by integrating the area denoted by the black box in (a).

For TRPL measurements on GaN NW ensembles, the fluence is reduced by neutral density filters to a typical value of 0.1 to $1 \mu\text{J}/\text{cm}^2$ in order to remain in the low excitation regime, where the corresponding transient PL spectra are dominated by the recombination of excitons bound to shallow donors. The upper limit for the expected carrier density in a NW array is estimated to $1 \times 10^{16} \text{ cm}^{-3}$ assuming a similar absorption coefficient for GaN NWs as for planar layers. This excitation density is several orders of magnitude below the Mott density in GaN.^[147]

Signal processing and evaluation

As a high dynamic range of the transient PL signal over at least three orders of magnitude and at the same time spectral information of the decay are desired, the analog integration mode was chosen rather than using the single-photon counting mode for detection. Before quantitative data can be extracted from a SC image, several steps of processing are necessary to remove different background contributions. First of all, the electronic background caused by the CCD and MCP is determined by repeating the measurement with a closed shutter in front of the SC. The optical background is determined in an analogous way by blocking the laser and repeating the data acquisition. Finally, the SC image is corrected for inhomogeneities of the phosphor screen inside the streak tube using a correction image measured under full illumination of the phosphor screen. Photoluminescence transients spectra are obtained by integrating a certain area of the SC image as displayed in Fig. 3.6. A PL transient [cf. Fig. 3.6(b)] is obtained by spectrally integrating the SC image using a certain spectral width depending on the FWHM of the investigated transitions. The PL transient data are then fitted by a convolution of the system response function and a sum of exponential decay functions in order to extract the effective lifetime(s) τ_{eff} of the transition. The estimated error for the determination of decay times lies in the range of ± 15 ps for fast decays ($\tau_{\text{eff}} < 200$ ps) and about 50 ps for slower decays with $\tau_{\text{eff}} > 500$ ps. The main contributions to this error originate from the sample inhomogeneity, slight variations of the focus as well as the reduced dynamic range of the signal for slow decay times. The system response function of the setup is determined by measuring a reflection of the excitation pulse using the same temporal resolution as in the actual data acquisition. Integrating a horizontal window of the SC image results in a PL spectrum for the given time frame as depicted in Fig. 3.6(c).

3.4. Introduction to the numerical methods

Two commercially available software packages, JCMSUITE[†] and LUMERICAL FDTD SOLUTIONS,[‡] are used in some parts of this thesis to simulate the interaction of GaN NWs with electromagnetic waves. While the former software is based on the finite element method (FEM), the latter employs the finite-difference time-domain (FDTD) method. In the following, a brief description of these two numerical methods is provided.

3.4.1. Finite-element method

The finite element method is a numerical technique for finding approximate solutions to boundary value problems described by partial differential equations. It calculates variations to minimize an error function and produce a stable solution in many sub-domains, which are generated by the so-called 'meshing', to approximate the equation in a larger

[†]<http://www.jcmwave.com/JCMSuite>

[‡]<https://www.lumerical.com/tcad-products/fdtd/>

3. *Experimental and numerical methods*

domain. The method was first employed in the 1950s for the solution of elasticity problems, but can be used for a wide variety of physical problems, which are described by partial differential equations, for example, by Maxwell's equations.

The software package JCMSUITE is a FEM-based computational tool used for the simulation of electromagnetic waves, elasticity, and heat conduction in three-dimensional geometries. Electromagnetic fields are simulated in the frequency domain by JCMSUITE, i. e., using monochromatic sources and calculating the non-transient part of the electric and magnetic fields. The software deals with three different classes of problems for electromagnetic waves, either propagating modes, resonance modes, or scattering problems. In the latter case, the propagation of an incident electric or magnetic field, for example a plane wave traveling through a given material, is simulated until a steady state condition is reached. The simulation is performed in various iterations, where an adaptive meshing allows for the enhancement of the accuracy in specific domains of the simulation volume.

In a post-process, the software is able to calculate the Poynting vector, i. e., the total energy flux at the boundaries of different material domains, and thus allows one to extract the amount of light which was absorbed, transmitted, and reflected in a certain domain.

3.4.2. Finite-difference time-domain method

The finite-difference time-domain (FDTD) method is a numerical analysis method used for modeling electrodynamics in the time-domain. This means it calculates approximate solutions of a system of differential equations, in the present case, of the time-dependent Maxwell's equations in partial differential form. Since it is a time-domain method, FDTD solutions can potentially cover a wide frequency range with a single simulation run and thus treat nonlinear material properties in a natural way. Maxwell's equations are discretized using central-difference approximations to the space and time partial derivatives. The resulting finite-difference equations are solved in a leapfrog manner: the electric field vector components in a particular volume of space are solved at a given instant in time; then the magnetic field vector components in the same spatial volume are solved at the next instant in time; and the process is repeated over and over again until the desired transient or steady-state electromagnetic field behavior is fully evolved. The FDTD method requires that the entire computational domain is described by a single grid, whose discretization must be sufficiently fine to resolve both the smallest electromagnetic wavelength and the smallest geometrical feature in the model. This requirement results in comparatively long calculations times for three-dimensional geometries.

The commercial software package LUMERICAL FDTD SOLUTIONS [§] is a 3D Maxwell solver based on the FDTD method. It allows one to easily generate various three-dimensional geometries including different types of sources for the electro-magnetic field. Monitor planes (2D) or boxes (3D) are employed to analyze different quantities

[§]<https://www.lumerical.com/tcad-products/fdtd/>

3.4. Introduction to the numerical methods

such as the total energy flux. Furthermore, the analysis capabilities include the calculation of waveguide modes and near-to-far-field projections.

Spectroscopy of NW ensembles and single NWs - a treatise on the benefits of good statistics

When investigating nanostructures such as NWs by means of optical spectroscopy, naturally a series of questions arise: Do all single objects from a sample have similar properties? Is it possible to characterize a sample and find correlations with certain parameters, such as the substrate temperature, by performing the experiment on a number of single dispersed NWs when the sample exhibits a density over 10^9 cm^{-2} objects? In order to tackle these questions, Sec. 4.1 starts with discussing the physical differences of investigating free-standing and single dispersed NWs by optical spectroscopy. Afterwards, Sec. 4.2 and 4.3 provide a treatise on the benefits and drawbacks of single NW and ensemble NW spectroscopy, based on a review of the relevant literature and my own experimental experience using spontaneously and selectively grown GaN NWs. This chapter motivates the decision to perform all experiments presented in the following chapters of this thesis on as-grown NW ensembles rather than dispersed or free-standing single GaN NWs.

4.1. Differences between dispersed and as-grown GaN NW PL measurements

The typical, high density of over 10^9 cm^{-2} found for spontaneously formed GaN NW ensembles on Si substrates prohibits the investigation of single as-grown NWs with optical spectroscopy. In order to investigate single NWs, they can be dispersed onto a foreign substrate by various methods.^[81] However, regardless of the method used, the optical properties of the NW are altered after dispersion. Thus, in the following the consequences of this dispersion process and the physical differences between as-grown and dispersed GaN NWs are shortly discussed.

4. Spectroscopy of NW ensembles and single NWs

Homogeneous and inhomogeneous strain

Due to their ability to relax strain elastically at the sidewalls, as-grown NWs are essentially free of any homogeneous strain.^[75,88,148,149] However, the GaN volume close to the substrate exhibits inhomogeneous strain emanating from locally broken or distorted bonds at the interface to the substrate.^[150] Additional inhomogeneous strain on a microscopic scale, i. e., micro-strain, was detected in GaN NWs by x-ray diffraction experiments.^[149] A recent investigation showed that the main source of this microstrain in GaN NWs is coalescence.^[151] The magnitude of the strain inhomogeneity induced by NW coalescence is not only determined by the coalescence degree, but also by the mutual misorientation of the coalesced NWs. This inhomogeneous microstrain manifests itself in an increase of the FWHM of the (D^0, X_A) transition obtained by μ -PL spectroscopy.^[151]

When as-grown GaN NWs are dispersed onto a foreign substrate the situation becomes more complex. A known consequence of the dispersion process is the generation of additional, adhesion-induced, homogeneous and inhomogeneous strain.^[81] Furthermore, the different thermal expansion coefficient of GaN and the (typically Si) substrate can induce homogeneous strain when the sample is cooled to low temperatures. Spectroscopic investigations of dispersed GaN NWs have revealed that the majority of the NWs exhibit much broader and shifted PL lines caused by the described interaction between the NW and the underlying substrate.^[81,84]

Excitation geometry and dielectric mismatch

Another important difference between (TR)-PL measurements on single dispersed NWs and as-grown NW ensembles is the change in excitation and emission geometry. In the former case the wavevector k is perpendicular to the c -axis of the wurtzite crystal structure of GaN, while it is the electric field vector E of the emitted light which is perpendicular to the c -axis in the latter case. It was recently shown that this change in experimental geometry leads to profound changes in the relative intensities of different transitions, for example, the (D^0, X_A) and (U, X) lines in GaN NWs.^[152]

Furthermore, the dielectric environment of dispersed NWs, i. e., lying flat on a substrate such as Si with a dielectric constant of $\epsilon = 30$, is very different to the one of as-grown NW ensembles, where the NWs stand upright and are surrounded by air ($\epsilon = 1$). As the dielectric environment has a direct impact on the free electrons and holes inside a NW due to the interaction with image charges,^[153] a change of the dielectric environment will necessarily affect the electron and hole wavefunctions. Such a change will ultimately manifest itself in a change of the binding energy of the free exciton.^[152] Consequently, even the PL spectrum of the *same* NW is inevitably altered after it has been dispersed onto a substrate due to the change of the local dielectric environment and experimental geometry. These differences were experimentally also confirmed for single CdSe NWs by measuring the absorption cross-section, polarization dependence and exciton dynamics compared with the ensemble using single NW extinction spectroscopy.^[154]

4.2. Role of statistics in optical spectroscopy of GaN NWs

Last but not least, the dielectric contrast between a GaN NW and its surroundings induces the NW to act as an optical waveguide if the NW diameter is large enough to support a guided mode of the emitted light.^[25,155–157] Together with the differences in experimental geometry discussed above, it is possible that light in a certain spectral range is thus guided away from the objective and can no longer be detected in a PL experiment. More details on the waveguiding properties of GaN NWs are provided in Sec. 7.4.1.

4.2. Role of statistics in optical spectroscopy of GaN NWs

A priori, one might assume that all NWs in an ensemble have equal structural and optical properties. However, considering their typical small volume of about 10^{-16} cm^3 , their PL spectra are determined by a few impurity atoms, such as donors and acceptors, which has been confirmed by Pfüller *et al.*, performing a statistical analysis of the optical transitions in single free-standing GaN NWs.^[86] Hence, their optical properties are inevitably subject to intrinsic statistical fluctuations if the NW volume is on the same order of magnitude as the reciprocal density of donor and acceptor atoms, as the incorporation of these impurities follows Poisson statistics.^[81,86] The effect of NW-to-NW fluctuations in optical properties is not exclusive to the GaN material system, and similar results were found in μ -Raman spectra on single InN NWs.^[158] Concerning the exciton dynamics, time-resolved photoluminescence spectroscopy on single GaN NWs^[96] and CdSe NWs^[153] revealed significant wire-to-wire fluctuations in effective exciton lifetimes.

If the differences in wire-to-wire PL spectra would be only caused by statistical fluctuations of single impurities, the effect is expected to vanish for much larger NWs, causing the NW to contain a large number of impurities. For a typical density of neutral donors of about 10^{16} cm^{-3} , a GaN NW with a volume of $1 \times 10^{-14} \text{ cm}^3$ contains on average about 100 donor atoms. Although some of those are ionized due to internal electric fields caused by the Fermi-level pinning,^[81] one might expect that these NWs have rather similar PL spectra at low temperatures as their spectra should no longer be determined by single impurities.

Figure 4.1 presents a comparison of the low temperature μ -PL spectra of three randomly selected, single NWs and two random positions of the corresponding spontaneously grown NW ensemble. These NWs have a length of $5 \mu\text{m}$ and a volume of approximately 10^{-14} cm^3 . The grey and blue shaded areas in Fig. 4.1 depict the spectral regions attributed to the recombination of the denoted transitions, e.g. free A and B excitons (X_A , X_B), neutral donor-bound excitons [(D^0, X)], neutral acceptor-bound excitons [(A^0, X)], excitons bound to unknown structural or point defects [(U, X)] and I_1 basal plane stacking faults (I_1 -SF). Strong differences between the PL spectra of the single dispersed NWs are observed although they originate from the same sample. While 'NW 1' and 'NW 3' are dominated by the recombination of the (D^0, X) , 'NW 2' is dominated by narrow lines between 3.445 and 3.465 eV, which are attributed to the (U, X) transition.^[84,87]

4. Spectroscopy of NW ensembles and single NWs

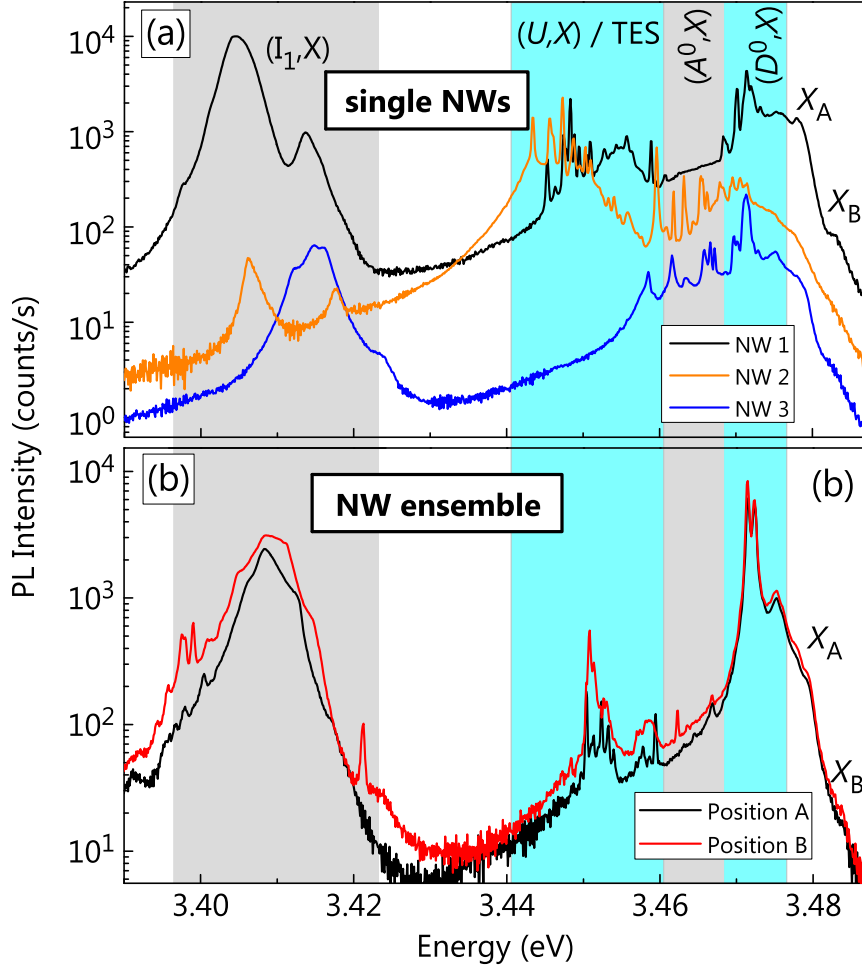


Figure 4.1: (a) Low-temperature PL spectra of three randomly chosen, single dispersed NWs (vertically shifted for clarity) from sample M9959. (b) Low-temperature PL spectra taken at two random positions of the corresponding NW ensemble. The shaded areas depict the spectral regions associated with the denoted transitions, which are explained in detail in the text and Sec. 2.2. The employed excitation density is $10^{-3}I_0$ for the single NWs [(a)] and $10^{-4}I_0$ for the NW ensemble [(b)].

Very pronounced are also the differences in the I_1 -SF emission intensity which is two orders of magnitude larger in 'NW 1' as compared to the other two. In contrast, if one measures low-temperature PL spectra on the as-grown NW ensemble at several random positions [of which two are presented in Fig. 4.1(b)], these spectra nicely overlap even on a logarithmic intensity scale. The ensemble spectra are dominated by the recombination of the (Si^0, X_A) and (O^0, X_A) states, but also show an intense and broad (I_1, X) emission band. Furthermore, a set of narrow, closely spaced lines at 3.45 and 3.46 eV attributed to the (U, X) transition.^[84,87] However, the intensity of the latter is much weaker in the ensemble than for the single dispersed NWs, as discussed above. Additionally, one expects the overlap with the intrinsic two-electron satellite transition (TES) in GaN^[21,70] at this

4.2. Spectroscopy of single, free-standing NWs in samples grown by SAG

spectral position, as discussed in Sec. 2.2.1. It is clear that the observed differences between the PL spectra from single NWs and NW ensembles stem from the better statistics of the latter. Exciting a single dispersed NW of this size probes about 100 donor atoms, and it is not clear if the collection efficiency of the microscope objective is equal for every NW as discussed in the previous section. Measuring the PL spectrum of the NW ensemble (in this case the $50\times$ objective was used) results in exciting at least 20 NWs in the case of an optimum focus and about 150 NWs in a realistic scenario, i. e., a slightly larger laser focus, as presented in Tab. 4.1. Consequently, far more impurity atoms (i. e., neutral donors in this case) are probed at the same time, which explains the homogeneity of the ensemble PL spectra presented in Fig. 4.1.

The number of excited NWs in an ensemble measurement deduced in Tab. 4.1 is even larger using the $15\times$ objective, and up to 1,000 NWs are excited simultaneously assuming a reasonable spot size of $5\ \mu\text{m}$ [cf. Sec. 4.3].* For TRPL measurements, the spot size is roughly $3\times 11\ \mu\text{m}$ causing over 1,500 NWs being excited simultaneously. Despite the strong differences of exciton lifetimes found in single free-standing GaN NWs,^[96] we thus expect a very good statistics for the determined effective lifetimes of as-grown GaN NW ensembles.

Summing up, experimental as well as theoretically expected effects cause the results of optical investigations on single dispersed NWs and as-grown NW ensembles to be naturally different. Yet, single NW spectroscopy remains a very powerful tool to investigate fundamental properties of individual NWs. For example, when studying single NWs by optical spectroscopy and correlate the results with their structural properties explored by SEM,^[159,160] and STEM-CL.^[161] However, results based on single NW experiments should not be extrapolated to represent the properties of the NW ensemble. It is thus questionable how relevant results are, which are based on investigating a single NW if one seeks for general properties of a material system.^[162] For the course of this thesis, it is hence advantageous to perform the (TR)PL measurements on as-grown GaN NW ensembles and benefit from the inherent better statistics in order to compare the optical properties of many different spontaneously grown NW ensembles.

*Note that the confocal PL setup limits the detection area of the luminescence signal to 2 and $7\ \mu\text{m}$ when the $50\times$ and $15\times$ objective are used, respectively.

spot size (μm)	corresponding area (μm^2)	approx. # of excited NWs
PL (optimum): 0.7	0.4	20
PL (realistic): 2–5	3–20	150–1,000
TRPL: 3×11	33	1,650

Table 4.1: Spot size, corresponding excitation area on the sample and approximate number of NWs being excited during PL and TRPL measurements for an as-grown NW ensemble with a typical NW density of $5 \times 10^9\ \text{cm}^{-2}$.

4.3. Spectroscopy of single free-standing GaN NWs in samples grown by selective-area epitaxy

Selective-area growth provides advantages in controlling the NW density and diameter compared with the spontaneous formation of GaN NWs [cf. Sec. 3.1]. The set of SAG samples fabricated at the *Paul-Drude-Institute* by T. Gotschke during his PhD thesis^[127] includes a sample where the properties of single, free-standing GaN NWs fabricated by SAG can be investigated. The growth time for this particular sample is 60 min, and the yield of NWs in the pre-patterned holes is nearly 100%. Only very few NWs formed on the SiO_x-mask for the present sample, which makes it suitable for single NW investigations. However, in general, samples fabricated by SAG exhibit strong parasitic growth of GaN NWs on the mask for large pitches $a > 1 \mu\text{m}$ and a growth duration above 60 min.^[127] These parasitic NWs limit the significance of μ -PL measurements as the resulting spectra represent an overlap between parasitic NWs and SAG NWs.

Figure 4.2(a) depicts the pattern written by electron-beam lithography (EBL) into the SiO_x-mask for one specific NW array of the field 'D3' on the sample [for more details cf. Ref. 127]. It includes 120 holes (red circles) with a nominal diameter of 50 nm and a center-to-center distance of 3 μm between the holes. At the corners of the array, four edge-like structures are written by EBL as openings in the mask as markers. The same method is used to write the label '3.0 μm ' below the array. Figure 4.2(b) presents a scanning electron micrograph of the top right edge of the same area after MBE growth. The desired NW arrangement is clearly recognized and further emphasized by the dashed lines. The NWs grown inside the holes have a length of about 300 nm and are slightly tapered with a diameter of 100 nm at the base and 60 nm at the top. The tapering is probably caused by the fact that the sample was not rotated during growth. The NW diameter is larger than expected, possibly due to imperfections in the EBL process and a radial overgrowth of GaN material over the hole.^[127] The marker at the top right corner is recognized as a wall of coalesced GaN material.

Figure 4.2(c) presents a low-temperature μ -PL map of the area depicted in Figure 4.2(a). The map consists of $115 \times 111 = 12,765$ single spectra, each integrated for 0.5 s. The step size of the translation stage was 400 nm in the x - and y -direction, and the excitation density was set to $10^{-3} I_0$. The PL map is color coded from blue (low) to green (high) intensity and spectrally integrated from 3.460 to 3.475 eV, i. e., covering the bound exciton lines of GaN. The hexagonal arrangement of the NWs is easily observed in the PL map, although it is convoluted with the laser profile caused by the LMU-15 \times -objective, which has a maximum intensity in the center surrounded by a ring-like intensity profile.[†] Due to their nanoscopic diameter, each single free-standing GaN NW maps the laser profile in this measurement.

[†]c. f. the technical data sheet of the used LMU-15 \times -NUV objective found at: <http://www.thorlabs.de/>

4.3. Spectroscopy of single, free-standing NWs in samples grown by SAG

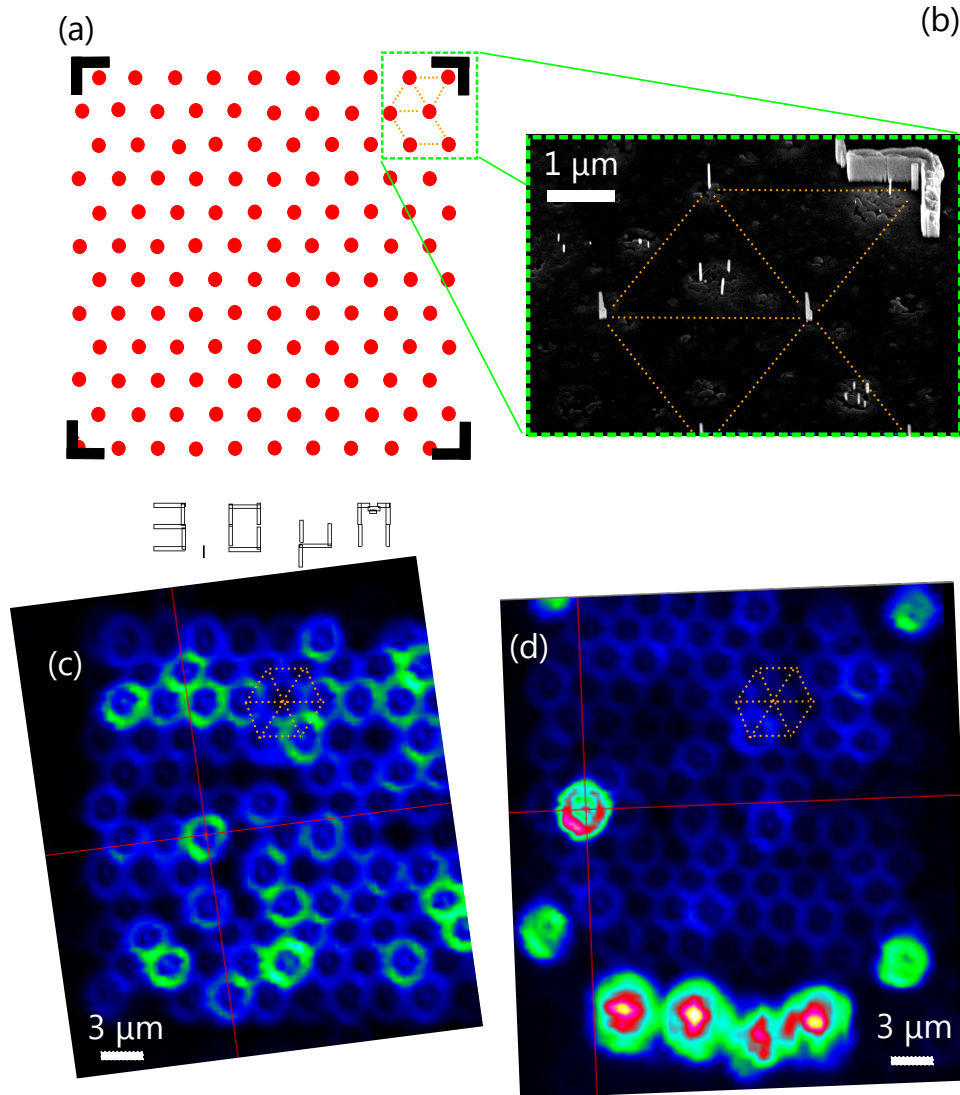


Figure 4.2: (a) Schematic EBL mask pattern of a single array of the field 'D3' in sample M81228. (b) Scanning electron micrograph (taken by A.-K. Bluhm) of the top right corner of this array after NW growth. For clarity, the arrangement of individual NWs grown inside the holes of the mask is emphasized by dashed lines. (c) Low-temperature cw PL map consisting of 12,765 single μ -PL spectra obtained by mapping the area depicted in (a) with the x-y-translation stage. The intensity is color coded from blue (low) to high (green) intensity and spectrally integrated between 3.460 and 3.475 eV. (d) A PL map from the same array as in (c), but now spectrally integrated over the spectral region from 3.40 to 3.43 eV. The markers at the corners and the label below the field (as well as one single NW inside the field) are now clearly identified as GaN material exhibiting a high density of I_1 -stacking faults.

We can thus conclude that the diameter of the laser focus was about 5 μm during the measurement, confirming the estimation from Sec. 3.2. Since the radius of the excitation spot is still smaller than the wire-to-wire distance (2.5 vs. 3 μm), it is possible to correlate

4. Spectroscopy of NW ensembles and single NWs

each PL spectrum with the respective single free-standing GaN NW. This correlation is further simplified by the fact that clear differences between the PL spectra of neighboring GaN NWs are observed (discussed below), while the PL spectra obtained around one single NW only differ in their intensity due to a changing excitation density when the excitation laser is scanned over the NW.

Figure 4.2(d) presents a similar PL map as in (c), but now displaying the spectrally integrated intensity between 3.40 and 3.43 eV, i. e., the region associated with the recombination of excitons bound to I_1 basal plane stacking faults.^[38,40,87,163] Note that the PL intensity represented by the color scale cannot be directly compared to Fig. 4.2(c). The most prominent observation is that the markers at the four corners and the label below the field have a much stronger PL signal in this spectral region, together with one single, exceptional NW inside the field. The higher SF-related intensity of the corners and the label can be easily understood. The pattern written by EBL into the mask at these specific points consists of large openings in the mask. During the growth of the GaN NWs, these areas form heavily coalesced regions of GaN material shaped accordingly to the mask opening [cf. the marker in the top right corner of Fig. 4.2(b)]. Coalescence is known to be one of the reasons for the formation of different types of stacking faults in GaN NWs.^[40,87] The clear visibility of the hexagonal NW arrangement in Figs. 4.2(c) and 4.2(d) verifies that the photoluminescence signal is dominated by the GaN NWs grown in the desired holes of the mask. The PL intensity of parasitically grown GaN NWs between the holes is negligible in this case.

Figure 4.3 displays the low-temperature (10 K) PL spectra of four exemplary single GaN NWs grown by SAG extracted from the PL map displayed in Fig. 4.2(c). It is immediately clear that their PL spectra differ significantly both in intensity and spectral features. The μ -PL spectrum of 'Nanowire 1' is dominated by several narrow transitions in the energy range of the (D^0, X_A) , each exhibiting a linewidth limited by the spectral resolution of 250 μ eV. These lines thus very likely stem from the recombination of single impurities in this particular NW. 'Nanowire 2' exhibits a broader (D^0, X_A) transition with a linewidth of 3.5 meV. The FWHM of the dominate transition in 'Nanowire 3' is even larger (10 meV) and blueshifted by 3 meV with respect to the first NW. The PL spectrum of 'Nanowire 4' does not exhibit any distinct spectral features, and its PL intensity is overall much weaker compared to the others. Given the very different FWHM of the (D^0, X_A) line in these single NWs, it is likely that the individual NWs exhibit different degrees of coalescence-induced inhomogeneous strain.^[151] In summary, one can state that although the individual NWs have been grown close-by in a single growth experiment and might look very similar imaged by a scanning electron microscope [cf. Fig. 4.2(b)], their μ -PL spectra reveal severe differences from NW-to-NW. As the excitation configuration was identical for each wire in this case, it is unlikely that the observed differences stem from extrinsic effects such as differences in excitation density and absorption or collection efficiency. However, considering the relatively small volume of the NWs of about $1 \times 10^{-15} \text{ cm}^{-3}$, an influence of statistical effects such as a different incorporation of im-

4.3. Spectroscopy of single, free-standing NWs in samples grown by SAG

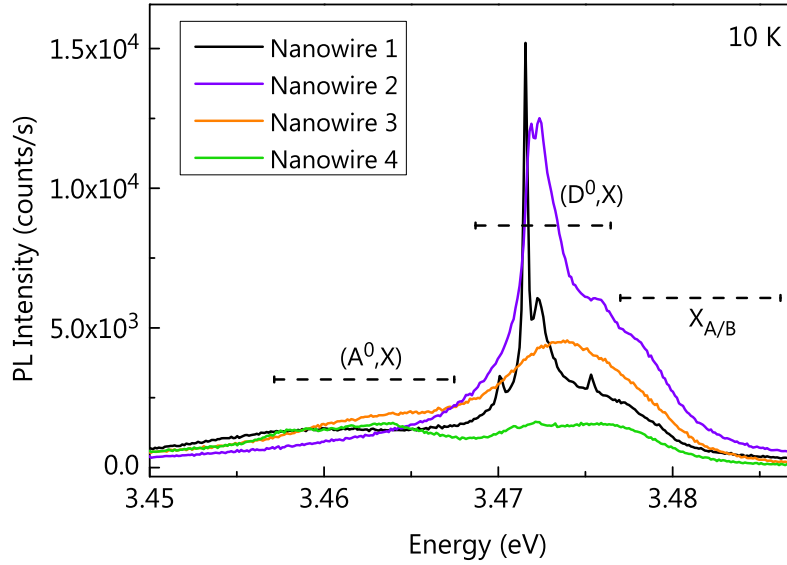


Figure 4.3: Four exemplary low-temperature (10 K) μ -PL spectra of single NWs from sample M81228, extracted from the PL map in Fig. 4.2(c). The dashed lines represent the spectral range associated with the recombination of the denoted free and bound excitonic states.

purities is expected [cf. Sec. 4.2]. Note that essentially every single PL spectrum for the 120 NWs in the present array is different. While some similarities appear, there is no correlation between, for example, linewidth of the (D^0, X_A) and position of the NW inside the array.

Unfortunately, in samples with much larger NWs (i. e. longer growth time), the arrays with large NW-to-NW distances exhibit a noticeable higher degree of parasitic growth, whose contribution to the PL spectra can no longer be neglected. Consequently, the experiments involving samples grown by SAG in this thesis focus on larger NWs with a volume $> 10^{-16} \text{ cm}^{-3}$ in closely spaced arrays with NW-to-NW distances of $1 \mu\text{m}$ at most. Using the $15\times$ objective for the PL measurements on SAG GaN NW arrays then causes still a sufficiently large number (> 30) of NWs to be excited simultaneously, which results in measuring essentially identical PL spectra at different positions of the array. This ensures that the obtained (TR)-PL spectra can be used to characterize the array without being dominated by statistical fluctuations of single impurities.

Investigating the origin of the fast decay of bound excitons in GaN nanowires

The transient photoluminescence of various GaN NW ensembles is investigated and a biexponential decay is observed at low temperatures. At first glance, it is tempting to attribute the fast decay component to nonradiative surface recombination and the long component to radiative recombination in the bulk. However, applying a model based on this assumption cannot explain the experimental data for GaN NW ensembles with different average diameters. Thus, the origin of the dominating short component of the decay is explored at first, and the experimental results show that it is governed by a nonradiative decay channel other than the surface, between 10 and 300 K. Additionally, the donor-bound and free exciton states are found to exhibit a common effective lifetime, revealing an efficient coupling of both states even at low temperatures. The consequences of this coupling for the exciton dynamics in GaN NWs are explored by solving a rate equation model. It turns out that the nonradiative decay may occur via either the bound or the free state of the exciton resulting in the same dynamics of the system. Finally, the effective lifetimes at low temperatures are determined for GaN NW ensembles with different surface-to-volume ratios and coalescence degrees. No systematic variation with either of these quantities is observed, suggesting that the dominating nonradiative channel in the investigated GaN NWs is neither related to the surface nor to coalescence-induced defects. Note that some of the results presented in this chapter have been published in Refs. 106 and 164.

5.1. Introduction

Based on the many reports that state that GaN NWs are free of extended structural defects such as dislocations,^[40,73–75] it is commonly assumed that their internal quantum efficiency η_{int} is close to one at low temperatures (10 K).^[92] Consequently, the room-temperature quantum efficiency of GaN NW-based devices is then approximated by the ratio between low-temperature and room temperature PL intensity. Yet, to our knowl-

5. Investigating the origin of the fast decay of bound excitons in GaN nanowires

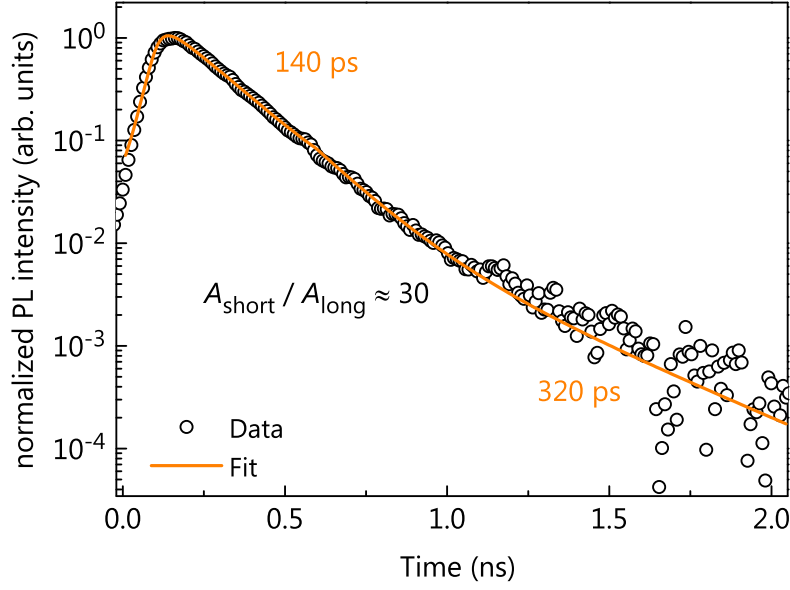


Figure 5.1: Low-temperature (10 K) TRPL transient of the (D^0, X_A) for a spontaneously grown GaN NW ensemble (sample R). The decay times given next to the transient has been extracted by a fit (solid line) of the experimental data with a phenomenological biexponential decay convoluted with the system response function. Additionally, the ratio of the amplitudes for the fast and slow decay components are given.

edge, a pure radiative decay of the states which give rise to the luminescence in GaN NWs has not been observed yet. In order to rigorously deduce and compare η_{int} for GaN NW ensembles grown under different experimental conditions, we first need a thorough understanding of the PL transient, as η_{int} depends on the ratio of the effective to the radiative lifetime as described in Sec. 2.2.2. Such an understanding may help to further improve the internal quantum efficiency of GaN NWs and hence pave the way for the development of efficient optoelectronic devices based on GaN NWs.

An exemplary PL transient of a typical GaN NW ensemble (sample R) grown on Si(111) under N-rich conditions and a substrate temperature of 835 °C is shown in Fig. 5.1. More specifically, this transient displays the luminescence decay of the (D^0, X_A) state after pulsed excitation using an excitation density of about 1 $\mu\text{J}/\text{cm}^2$ at $T = 10$ K. Evidently, the PL transient is not monoexponential, which inhibits the extraction of a unique lifetime of this state and similarly to what has been found by other groups.^[89,96–98] Instead, the time-dependent PL intensity is well represented by a biexponential decay $I(t) = A_{\text{short}} \exp(-t/\tau_{\text{short}}) + A_{\text{long}} \exp(-t/\tau_{\text{long}})$ convoluted with the system response function of the excitation pulse. The PL transient exhibits short and long decay times of 140 ps and 320 ps, respectively. The decay is dominated by the short component, which is expressed by the large ratio between the short and long component of the biexponential decay $A_{\text{short}}/A_{\text{long}} = 30$. Evidently, neither of the two observed decay times is close to

5.2. Considering an enhanced radiative recombination rate of bound excitons

the expected radiative lifetime of 1 ns for this state.^[21,22] The PL decay of the (D^0, X_A) state is thus affected by nonradiative recombination under the employed experimental conditions for the present sample. While similar decay times for the short component of the (D^0, X_A) are observed for various samples, the longer decay time fluctuates strongly from sample to sample as will be discussed in Sec. 5.3.

5.2. Considering an enhanced radiative recombination rate of bound excitons

The observed effective lifetimes of the (D^0, X_A) complex in the GaN NW sample R in the previous section are much shorter than expected for a purely radiative recombination process of this complex in the bulk. In free-standing, bulk-like GaN, values in excess of 1 ns have been measured for the effective lifetime of this transition at low temperatures.^[21,22] This value should thus be considered as a lower limit for the radiative lifetime of the (D^0, X_A) in GaN. However, similar values as the one presented in the previous section for the (D^0, X_A) decay time have been reported by different groups in GaN NWs,^[88,89,94-96] while no agreement has been reached on whether this decay time signifies a radiative or nonradiative decay of this state.

As a GaN NW represents in principle an optical microcavity,^[165] one could argue that the spontaneous emission rate of bound excitons may be enhanced by the Purcell effect.^[166] A necessary prerequisite for this effect is that the cavity formed by the NW supports a mode (i) matching the frequency of the investigated transition and (ii) having a spatial overlap with the position of the emitter.^[26] Quantitatively, however, a Purcell factor $f_P > 6$ would be required in order to enhance the radiative rate from 1 ns^{-1} in the bulk^[21,22] to 6 ns^{-1} in the NWs, i. e. values of $\tau_{\text{short}} \approx 150$ as observed experimentally.^[88,89,94-96] Yet, calculated and experimentally determined values of f_P averaged over the random position of the emitters in NWs are in the range of $1 < f_P < 2$,^[167-169] mainly due to the low Q -factor of GaN NWs and the random position of the donor atoms with the NWs. In addition, for the Purcell effect to result in the mono-exponential decay over roughly two orders of magnitude observed experimentally [cf. Fig. 5.4(b)], where over 100 NWs are probed simultaneously, f_P would have to be essentially identical for the vast majority of NWs despite their highly irregular shapes [cf. Fig. 5.2] and the variations in their length ($\pm 100 \text{ nm}$) [cf. Fig. 3.1]. It thus seems exceedingly unlikely that the short decay time τ_{short} of the (D^0, X_A) complex is related to a purely radiative process. The long decay time τ_{long} , however, varies between ≈ 300 and 850 ps ^[170] and could be considered to be radiative at first glance. Let us, for a moment, assume that the required Purcell factor between 1.2 and 3 is not entirely unlikely for a GaN NW and that the longer decay component thus represents the radiative decay of the (D^0, X_A) complex inside the GaN NWs. In the following section we investigate this hypothesis by correlating the magnitude of the respective amplitudes with structural parameters of the GaN NW ensembles.

5.3. A first step towards understanding the PL transient of GaN NWs

As discussed in Sec. 2.2.1, the PL decay in planar GaN is also not completely understood yet. However, one group has attributed the occurrence of a short decay time to nonradiative surface recombination, while the long component has been ascribed to the decay of (D^0, X_A) states inside the bulk.^[22]

At first glance, it seems plausible to transfer this idea of the exciton dynamics in planar layers onto GaN NWs and attribute the fast decay component to nonradiative recombination at the NW surface.^[89,94–97] A second possibility is to question the assumed structural perfection of GaN NWs which is commonly taken for granted, and attribute the short PL decay to nonradiative recombination at crystal defects. Given that the NW density in spontaneously formed GaN NW ensembles is on the order of 10^9 to 10^{10} cm^{-2} , coalescence of adjacent NWs during their formation is inevitable. Basal plane stacking faults^[40,171] and very recently, chains of dislocations^[171] have been observed as consequences of the coalescence of GaN NWs. The former defects capture free excitons efficiently, but manifest themselves by characteristic radiative transitions at specific energies.^[38,48,87,163] In contrast, the latter were found to act as efficient nonradiative centers for excitons.^[40]

Description of the model

In order to evaluate the two possibilities of nonradiative recombination we employ a straightforward model to simulate the expected PL transient for both cases. The model postulates two classes of (D^0, X_A) states, one in close proximity to a defect, i. e., either the NW surface or a coalescence-induced dislocation causing the (D^0, X_A) to decay with a fast decay time, and the other unaffected by this nonradiative channels and thus decaying with the experimentally determined longer decay time, which we assume for this moment to be radiative and shorter than 1 ns due to a possible Purcell effect. The two classes are motivated by the biexponential PL decay of GaN NWs observed experimentally [cf. Fig. 5.1].

Influence of the surface

The (D^0, X_A) complex in GaN is a spatially localized state, but even its ground state has a spatial extent much larger than the lattice spacing in GaN. It has been shown that the ground state energy of free Wannier excitons is significantly influenced by a nearby surface within a distance of approximately two times the exciton Bohr radius (a_B),^[85,172] which translates into a value of about 10 nm for the (D^0, X_A) complex in GaN^[49,173] [cf. Sec. 2.2.1]. For a spatially uniform distribution of donors, a certain fraction α will be located within this distance relative to the NW surface and thus experience nonradiative surface recombination.^[96] If we assume that the GaN NWs are otherwise free of

5.3. A first step towards understanding the PL transient of GaN NWs

nonradiative defects, one would also expect that excitons bound to the fraction $(1 - \alpha)$ of donors exhibit a lifetime corresponding to the long decay time determined in the experiment. Consequently, we employ a core-shell model analogous to that proposed by Corfdir *et al.*^[89] to describe the PL transient. In the following, we assume that the decay rate of the (D^0, X_A) complex is equal to $\gamma_1 = \tau_{\text{long}}^{-1}$ for all donors in the core of the NW and to $\gamma_s = \tau_{\text{short}}^{-1}$ for all donors in the 10 nm thick shell. Although the decay rate is expected to increase for the (D^0, X_A) state with decreasing distance to the surface,^[96] the assumption of a constant γ_s is a reasonable approximation motivated by the clear biexponential PL transient [cf. Fig. 5.1]. Within this model, the time-dependent PL intensity $I(t)$ resulting from the decay of the (D^0, X_A) state in an ensemble of N NWs is given by

$$I(t) = \sum_j^N [\alpha_j e^{-\gamma_s t} + (1 - \alpha_j) e^{-\gamma_1 t}] = \alpha e^{-\gamma_s t} + (1 - \alpha) e^{-\gamma_1 t}, \quad (5.1)$$

since γ_s and γ_1 are constants in our model which we extract directly from the experimental data. Within this approximation, a biexponential PL transient is expected for the (D^0, X_A) transition when integrating over many NWs and thus donors. In order to calculate the value of α for a given NW sample, it is required that the NW cross-section does not change with its length. Furthermore, since the length of the investigated NWs is much larger than their diameter [cf. Fig. 3.1], the surface-to-volume ratio of a NW is well described by the perimeter-over-area ratio of its top facet. Usually, the average disk diameter $d_{\text{disk}} = 2\sqrt{A/\pi}$ is employed to calculate a NW diameter from the area A of its top facet. However, it is shown in App. A that one should consider the non-circular shape and thus larger perimeter P of the NW cross section for the same A of highly coalesced NW aggregates [cf. Fig. 5.2(a)]. This is achieved by defining the effective NW diameter $d^* = 4A/P$, i. e., explicitly considering both, the area and perimeter as derived in App. A. For NWs with d^* much larger than $2a_B$, α is easily obtained by considering the ratio of the NW core area to the total cross-section of each NW:

$$\alpha = \frac{1}{N} \sum_{j=1}^N \alpha_j \approx \frac{2a_B}{N} \sum_{j=1}^N \frac{4}{d_j^*} = \frac{2a_B}{N} \sum_{j=1}^N \frac{P_j}{A_j}. \quad (5.2)$$

Influence of coalescence

In a similar fashion, one can assume a worst case scenario where the decay of *every* (D^0, X_A) complex in a coalesced aggregate is governed by a nonradiative channel with an effective lifetime of $\tau_{\text{short}} = \gamma_s^{-1}$, again taken to be equal to the short component of the experimental PL transient for the respective sample. Furthermore, we assume that all donor-bound excitons in single, uncoalesced NWs decay with a possibly enhanced radiative lifetime of this state $\tau_{\text{long}} = \gamma_1^{-1}$ equal to the long decay time determined experimentally. Once again, all donor-bound excitons in a GaN NW ensemble are separated into two distinct classes, this time according to the coalescence degree σ , which gives rise

5. Investigating the origin of the fast decay of bound excitons in GaN nanowires

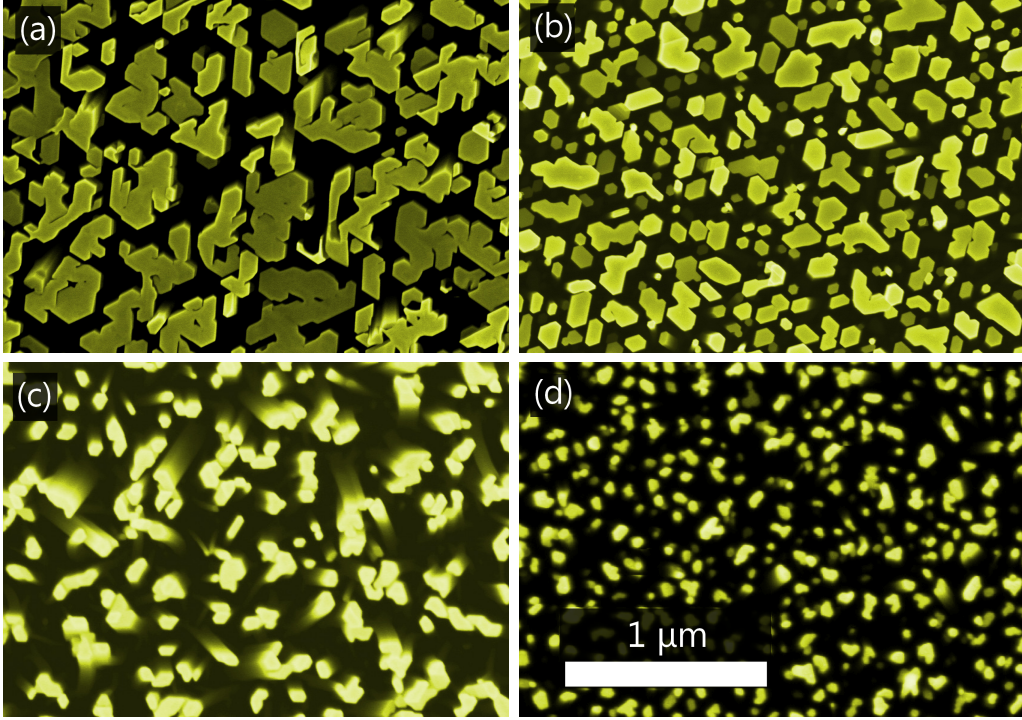


Figure 5.2: Top-view scanning electron micrographs for (a) sample A, (b) sample B, (c) sample R and (d) sample D. The scale bar in (d) applies to all images. The coalescence degree σ of the samples was determined from these micrographs according to the method described in Sec. A and summarized together with the parameter α in Tab 5.1. The images have been taken by A.-K. Bluhm.

to the following biexponential decay:

$$I(t) = \sigma e^{-\gamma_s t} + (1 - \sigma) e^{-\gamma t}. \quad (5.3)$$

Comparison of the model with experimental data

Four spontaneously formed GaN NW ensembles with different average NW diameters and coalescence degrees are now analyzed and their experimentally obtained PL transient compared with both models. Figure 5.2 presents top-view scanning electron micrographs of the four samples named A, B, R and D. The coalescence degree of the samples is calculated based on a geometric analysis of the shape of the top facets of the individual wires as explained in detail in Sec. A. For the depicted samples, the coalescence degree σ and the ratio of surface-near donors to the total number of donors α are summarized in Tab. 5.1.

Figure 5.3 shows a comparison of the experimentally obtained PL transient data of the (D^0, X_A) complex at 10 K (symbols) and the simulated PL transients of the model con-

5.3. A first step towards understanding the PL transient of GaN NWs

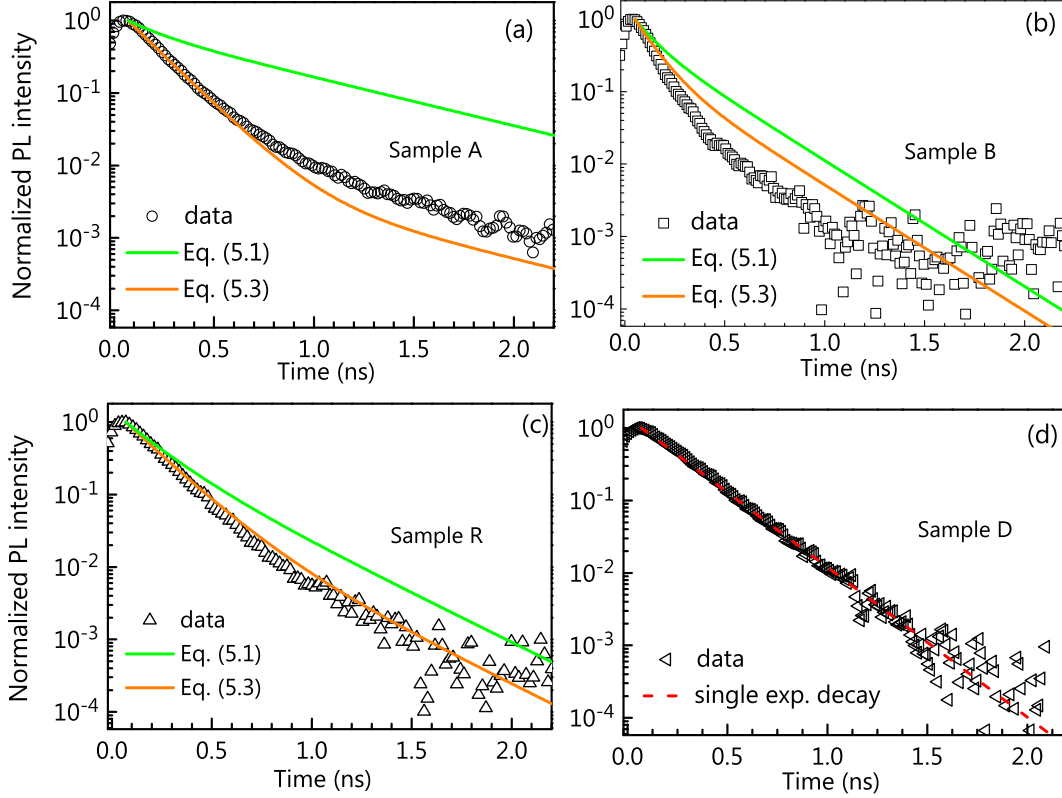


Figure 5.3: TRPL transients of the (D^0, X_A) transition for (a) sample A, (b) sample B, (c) sample R and (d) sample D integrated over a 5 meV wide spectral window centered at the maximum of the transition. The solid lines show the simulated transients predicted by models taking into account the impact of the surface [Eq. (5.1)] and the degree of coalescence [Eq. (5.3)], respectively.

considering either nonradiative recombination at the surface (green lines) or at coalescence-induced defects (orange lines) using Eqs. (5.1) and (5.3), respectively. Evidently, none of the models can consistently describe the experimental PL transient for all samples. While the model considering nonradiative recombination of (D^0, X_A) states at coalescence-induced defects [cf. Eq. (5.3)] seems to describe well the PL transient of sample R, it fails to reproduce the decay for samples A and B. The model assuming the surface as the origin of the short component of the TRPL transient is obviously also not able to explain the experimental data as the amplitude of the short component is much larger than the determined ratio of surface-near (D^0, X_A) states [cf. also Tab. 5.1].

The comparison between the experimentally determined amplitudes of the short and long components of the (D^0, X_A) transient and the values predicted by the models is also presented in Tab. 5.1. It is evident that the normalized amplitude of the short component ($A_{\text{short}} / (A_{\text{short}} + A_{\text{long}})$) neither correlates with the coalescence degree σ of a GaN NW ensemble nor with the average effective NW diameter $\langle d^* \rangle$. While both parameters vary

5. Investigating the origin of the fast decay of bound excitons in GaN nanowires

Sample	σ	$\langle d^* \rangle$ (nm)	α	$A_{\text{short}} /$ $(A_{\text{short}} + A_{\text{long}})$	τ_{short} (ns)	τ_{long} (ns)
A	$0.99^{+0.01}_{-0.1}$	102 ± 60	0.31 ± 0.1	>0.96	0.16 ± 0.02	0.65 ± 0.02
B	0.7 ± 0.1	80 ± 40	0.52 ± 0.1	>0.97	0.09 ± 0.02	0.25 ± 0.02
R	0.9 ± 0.1	72 ± 25	0.62 ± 0.1	>0.96	0.14 ± 0.02	0.32 ± 0.02
D	0.5 ± 0.1	53 ± 20	0.91 ± 0.1	>0.99	0.21 ± 0.02	–

Table 5.1: Summary of various parameters of the investigated GaN NW samples in the present section. Coalenscence degree σ of the ensemble, average effective diameter $\langle d^* \rangle$, and ratio of surface-near to total donors α . The ratio of the amplitude of the short decay time $A_{\text{short}} / (A_{\text{short}} + A_{\text{long}})$ of the total decay and the values of the short and long decay times τ_{short} and τ_{long} have been extracted from a biexponential fit to the data presented in Fig. 5.3, convoluted with the system response function (not shown).

significantly between the four samples, the short component of the decay dominates the decay with an amplitude of over 96% in *all* samples. The observation is most prominent for sample D, where over 99% of all (D^0, X_A) states are found to decay with the short decay time resulting in a single-exponential decay over at least three orders of magnitude [cf. Fig. 5.3(d)]. This is a clear indication that a different origin for the nonradiative decay given by the short decay time is present in this sample as it is highly improbable that $>99\%$ of all (D^0, X_A) states are by coincidence in a distance closer than 10 nm to the surface or dislocations in this NW ensemble.

Summing up, it can be concluded that the amplitude ratio between the short and long decay components of the PL transients cannot be consistently described within the framework of the presented models. The disagreement between the simulated PL transients and the experimental data is not a question of minor deviations in σ or d^* , but caused by large discrepancies in the expected amplitudes of the two decay components. Even considering both effects at the same time does not explain the magnitude of the short component of the decay in a consistent way.^[106] The result from this section thus raises two questions: (i) what is the origin of the short component of the decay and (ii) what causes the biexponential decay which is observed for most of the samples. The first question is addressed in the following Sec. 5.4, and the origin of the biexponential decay will be discussed in Chap. 6.

5.4. Investigating the origin of the short component of the bound exciton decay

Obviously, the two models used in the previous section cannot explain the origin of the two decay components in the (D^0, X_A) PL transients of GaN NW ensembles. Especially, the amplitude of the short decay is found to dominate the PL transient of the (D^0, X_A) state for GaN NW ensembles regardless of their morphological properties. Thus, a more detailed investigation of this decay component is necessary. In this section, the origin of the short component is explored by a combination of temperature-dependent cw and TRPL spectroscopy. The investigation focuses first on the GaN NW reference sample R which was already discussed in the previous section. Afterwards, in Secs. 5.4.4 and 5.4.5, the exciton lifetimes of 19 different GaN NW samples (including sample A and B from the previous section) are compared and discussed.

5.4.1. Observation of identical lifetimes of the free and donor-bound exciton

Figure 5.4(a) presents the low-temperature cw PL spectrum of sample R, which exhibits the typical excitonic transitions of GaN NW ensembles described in Sec. 2.2. The spectrum is dominated by the recombination of A excitons bound to neutral donors $[(D^0, X_A)]$ at (3.4707 ± 0.0001) eV with a full-width at half-maximum of 1 meV. On the high-energy side of this transition, a shoulder is visible at (3.4742 ± 0.0005) eV, which stems from the recombination of B excitons bound to neutral donors $[(D^0, X_B)]$. The transition arising from the recombination of free A excitons (X_A) is centered at (3.4780 ± 0.0005) eV. Between 3.445 and 3.455 eV, several narrow lines forming the (U, X) band are observed. The origin of these lines is still under investigation and discussed in detail in Sec. 2.2.1. Finally, several lines originating from the recombination of excitons bound to I_1 basal-plane stacking faults $[(I_1, X)]$ are detected around 3.41 eV.^[38,40,48,87,163]

Figure 5.4(b) depicts the short component of the PL transient for the X_A and (D^0, X_A) transitions of sample R extracted from streak camera images and integrated over a 3 meV wide spectral window centered on the respective transition. The temperature of the cryostat is $T = 10$ K and the excitation density set to $1 \mu\text{J}/\text{cm}^2$. A fit of the data within the first ns with a single exponential decay reveals an effective decay time of $\tau_{\text{eff}} = (0.164 \pm 0.001)$ ns for the (D^0, X_A) and (0.167 ± 0.003) ns for the X_A . Note that only the first ns of each decay is displayed here. After about 1 ns, the transients deviate from a single exponential decay [cf. Fig. 5.1]. This slow component of the decay, which was already discussed in Sec. 5.3, will be investigated in detail in Chap. 6. The important result here is the parallel PL decay of the X_A and (D^0, X_A) transitions within the first ns after the excitation. However, since the X_A and (D^0, X_A) transitions in GaN are only separated by 7 meV, a spectral overlap between the respective PL lines is inevitable if we take into account the spectral resolution of the TRPL setup of 2.3 meV [cf. Sec. 3.3] and the width of both lines in the present case. Consequently, before concluding that the two

5. Investigating the origin of the fast decay of bound excitons in GaN nanowires

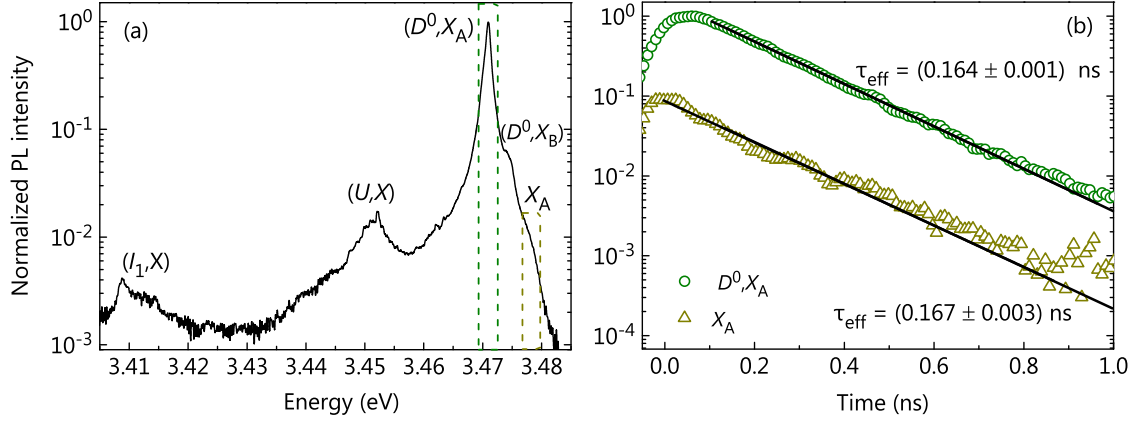


Figure 5.4: (a) Low-temperature (10 K) cw PL spectrum of sample R. The dashed lines indicate a 3 meV wide spectral window centered around the (D^0, X_A) and X_A transitions in the respective TRPL spectrum, which were used to spectrally integrate the low-temperature TRPL transients depicted in (b). (b) Photoluminescence decay of the (D^0, X_A) and X_A transitions within the first ns after excitation. The solid lines represents a fit to the data of a single exponential decay yielding the denoted effective decay times.

states truly have the same effective lifetime, the impact of this spectral overlap has to be considered.

Spectral deconvolution

In order to investigate whether the common lifetime of the X_A and (D^0, X_A) transitions is caused by their apparent spectral overlap, a detailed analysis of the TRPL data is performed. Figure 5.5(a) depicts a set of PL spectra extracted from the respective streak camera image, each integrated over a temporal window of 50 ps centered at different times after the excitation [cf. Sec. 3.3]. The spectra are normalized to the intensity of the (D^0, X_A) transition and displayed on a logarithmic scale to enhance the visibility of the X_A transition. It is seen that the intensity ratio of the (D^0, X_A) and X_A transition remains constant with time, while the relative contribution of the (U, X) transition to the spectrum increases with time. The former is a clear indication for a common decay time of the (D^0, X_A) and X_A . In contrast, a change in the relative PL intensity with time indicates a different decay time of the two states. In the present case, the (U, X) transition has a longer decay time than the (D^0, X_A) and X_A transitions. This qualitative impression is now quantified by performing a spectral deconvolution of each PL spectrum as shown in Fig. 5.5(b) for two exemplary spectra. The spectrum is fitted by a set of lineshape functions, which allows for a separation of the contributions of the individual transitions. The resulting, deconvoluted intensities of the X_A and (D^0, X_A) transitions are displayed in Fig. 5.5(c) with respect to time. Due to the decreasing signal-to-noise ratio at longer times, the deconvolution is only performed for the first 0.6 ns after the excitation. Yet, the result confirms that the two transitions exhibit the same effective lifetime. This com-

5.4. Investigating the origin of the short component of the bound exciton decay

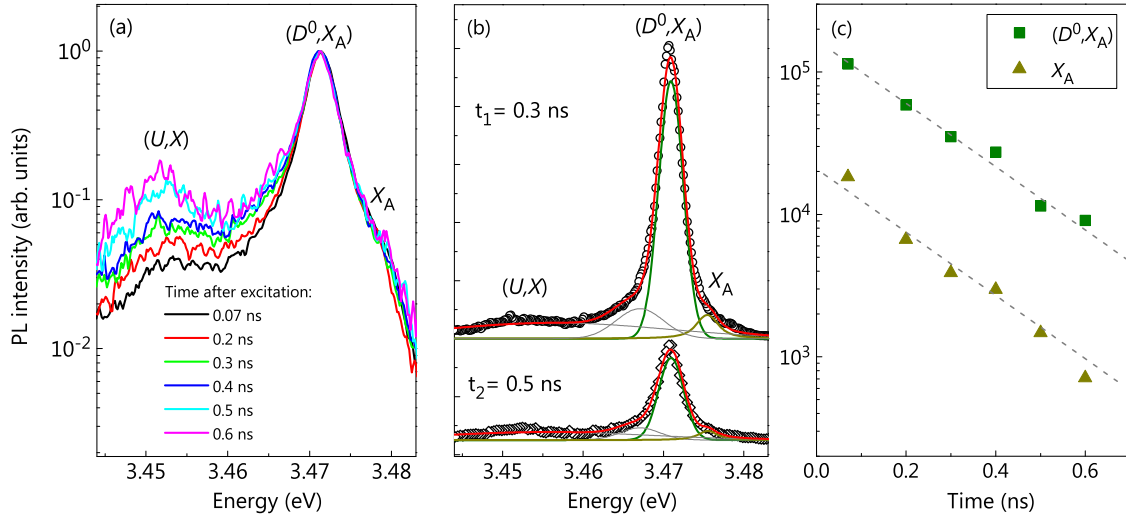


Figure 5.5: (a) PL spectra of sample R at different times after the excitation (normalized onto the (D^0, X_A) line). (b) Fit of the spectra at $t_1 = 0.3$ ns and $t_2 = 0.5$ ns after the excitation by a sum of several lineshape functions. The green lineshape represents the (D^0, X_A) , the yellow lineshape the X_A , while additional transitions are represented by the grey lineshapes. The sum of all lineshapes is depicted by the red solid line. (c) Time-dependent intensities of the (D^0, X_A) and X_A transitions as extracted from the spectral deconvolution of the spectra shown in (a). The dashed lines are a guide to the eye.

mon decay time suggests a coupling between these two exciton states as observed in a previous study for GaN NWs^[89] and under certain conditions also for planar GaN layers.^[22,174]

5.4.2. Temperature dependence of the PL intensity and exciton lifetimes

Figure 5.6(a) displays the evolution of the cw PL spectra of sample R with increasing cryostat temperature T . The vertically shifted PL spectra show that the bound excitons are progressively delocalized. Hence the relative contribution from the recombination of free A excitons is continuously increasing. At 300 K, the spectrum is eventually dominated by the recombination of free A excitons at 3.41 eV. In Fig. 5.6(b), the cw PL intensity spectrally integrated over the bound and free exciton states is plotted versus the temperature T . The PL intensity starts to quench already upon an increase of T to 15 K, evidencing the presence of a nonradiative channel even for the lowest temperature and follows a $T^{-3/2}$ dependence between 15 and 300 K.

In order to understand the origin of this quenching, temperature-dependent TRPL measurements are performed. Figure 5.6(c) depicts the effective decay time τ_{eff} (black squares) of the (D^0, X_A) and X_A transitions extracted from single-exponential fits to the short component of the PL transient integrated spectrally over both transitions.

5. Investigating the origin of the fast decay of bound excitons in GaN nanowires

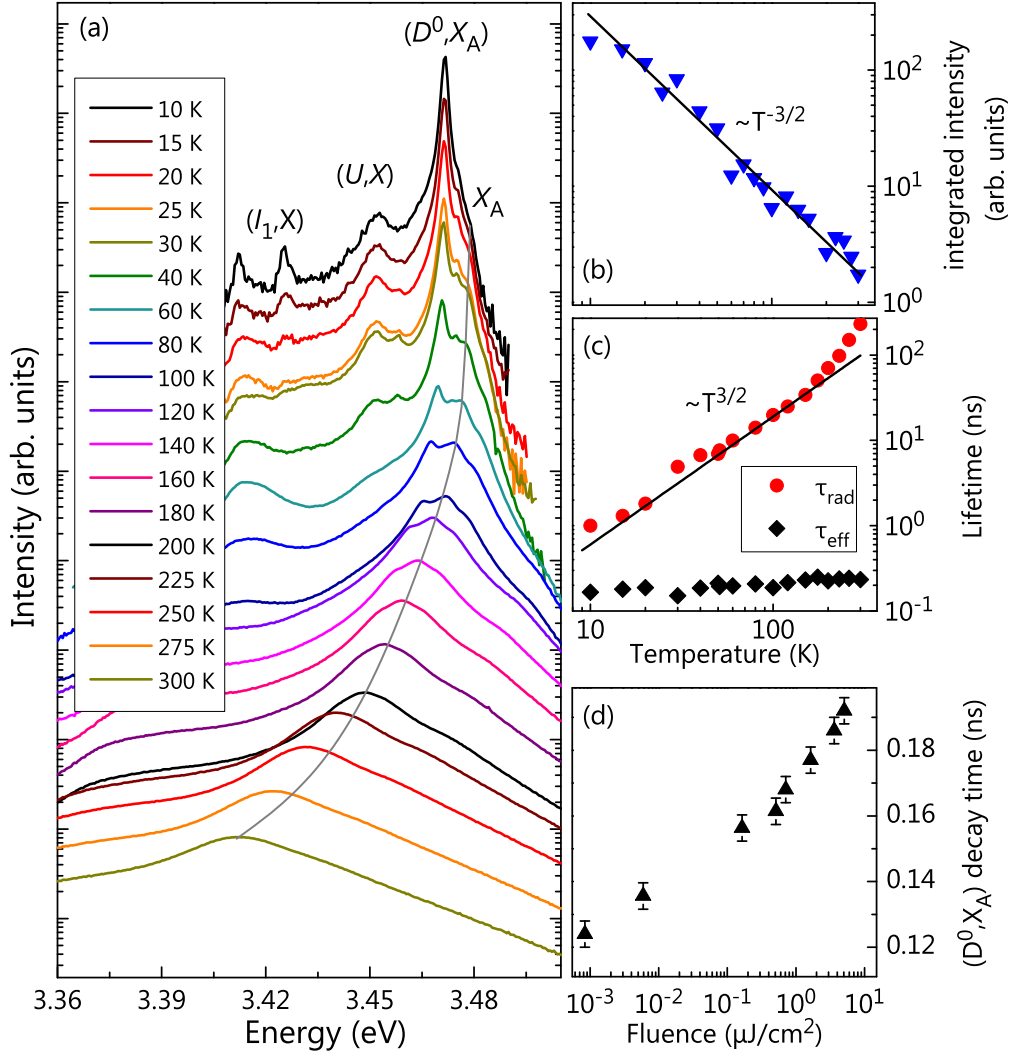


Figure 5.6: (a) Temperature-dependent cw PL spectra of sample R (the spectra have been shifted vertically for clarity). With increasing temperature, the bound exciton states are progressively delocalized, until the spectrum is dominated by the recombination of free A excitons (X_A) at room temperature (300 K). The grey line is a guide to the eye and highlights the spectral shift of the X_A transition with increasing temperature. (b) Evolution of the spectrally integrated PL intensity of the donor-bound and free exciton states between 10 and 300 K. The straight line shows that the integrated intensity decreases proportional to $T^{-3/2}$ with increasing T . (c) Effective (τ_{eff}) and radiative (τ_{rad}) lifetime obtained from temperature-dependent PL transients. The calculated values for τ_{rad} increase proportional to $T^{3/2}$, while τ_{eff} remains almost constant between 10 and 300 K. (d) Dependence of τ_{eff} on the excitation fluence at $T = 10$ K. [Reprinted figure with permission from Hauswald *et al.*^[164]. Copyright 2014 by the American Physical Society.]

This procedure is justified since the two states exhibit a common lifetime already at 10 K [cf. Figs. 5.4(b) and 5.5]. It is found that τ_{eff} does not decrease with increasing temperature, but instead slightly increases from 0.16 ns at $T = 10$ K to 0.23 ns at $T = 300$ K. This behavior clearly shows that there is no further, thermally activated nonradiative decay

5.4. Investigating the origin of the short component of the bound exciton decay

channel for the investigated sample.

Figure 5.6(c) shows the evolution of the radiative lifetime τ_{rad} (red circles) with increasing temperature normalized to 1 ns at 10 K. As the excitation pulse is much shorter than the recombination time, τ_{rad} is proportional to the inverse of the spectrally integrated PL peak intensity [cf. Eq. (A6) in Ref. 175]. The radiative lifetime is proportional to $T^{3/2}$ as expected for free excitons from theoretical grounds.^[60] The quenching of the PL intensity [cf. in Fig. 5.6(b)] is thus caused predominantly by the increase in the radiative lifetime, since the effective lifetime is essentially constant and equal to the nonradiative lifetime [cf. Fig. 5.6(c)]. The increase of the radiative lifetime for temperatures above 10 K supports the conclusion from Sec. 5.4.1 that the X_A and (D^0, X_A) states are already coupled in this regime. The deviation from the $T^{3/2}$ dependence at temperatures above 200 K is due to the increasing participation of free carriers in the recombination process.^[176]

Figure 5.6(d) depicts the dependence of the effective lifetime of the (D^0, X_A) on the fluence of the pulsed excitation at 10 K. The effective lifetime τ_{eff} is found to increase by less than a factor of two when the excitation fluence is varied over roughly four orders of magnitude. This suggests that the nonradiative channel responsible for the quenching of the PL intensity and the short effective lifetimes [cf. Fig. 5.6] is highly efficient and cannot be saturated under the experimental conditions employed. Additionally, the weak dependence guarantees that different excitation densities caused, for example, by a varying NW coverage for different samples do not lead to pronounced changes in τ_{eff} . This result, which is typically observed for GaN NWs, therefore allows for a comparison of the effective lifetime of GaN NW ensembles with different morphological properties and will be used in Secs. 5.4.4 and 5.4.5 to systematically investigate the dependence of τ_{eff} on the surface-to-volume ratio and the coalescence degree.

The combination of the experimental results presented in Fig. 5.6 shows unambiguously that the effective lifetime of the coupled system $(D^0, X_A) \rightleftharpoons X_A + D^0$ is dominated by a nonradiative decay channel over the whole investigated temperature range. Furthermore, the results imply that the free and bound exciton states are coupled even at low temperatures. Note that a similar behavior of the PL intensity and TRPL lifetimes as presented in this section was independently obtained for different GaN NW ensembles confirming that the described effects for sample R are not restricted to this sample. In the following section, the coupling of the (D^0, X_A) and X_A states is modeled and further investigated regarding its influence on the PL transients of GaN NW ensembles.

5.4.3. Rate equation model describing the coupling of free and bound excitons

An energy scheme of the coupled $(D^0, X_A) \rightleftharpoons X_A + D^0$ system, which is described by the following set of linear rate equations in the limit of low excitation densities, is displayed in Fig. 5.7:

5. Investigating the origin of the fast decay of bound excitons in GaN nanowires

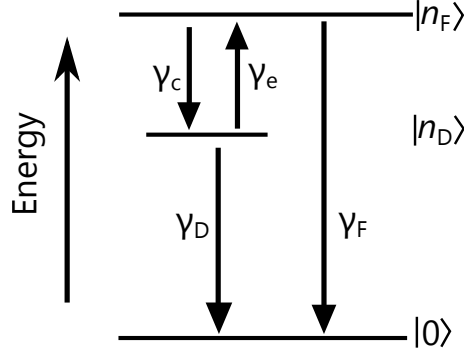


Figure 5.7: Schematic energy diagram visualizing Eqs. (5.4) and (5.5). The two states involved are denoted by $|n_i\rangle$, and the crystal ground state is represented by $|0\rangle$. The arrows represent the effective transitions rates between the different states.

$$\frac{dn_F}{dt} = -\gamma_c n_F + \gamma_e n_D - \gamma_F n_F \quad (5.4)$$

$$\frac{dn_D}{dt} = \gamma_c n_F - \gamma_e n_D - \gamma_D n_D. \quad (5.5)$$

Here, n_F and n_D denote the time-dependent densities of free and donor-bound excitons with the initial densities $n_F(0) = n_F^0$ and $n_D(0) = 0$, respectively, while γ_F and γ_D represent the sums of the respective radiative ($\gamma_{i,r}$) and nonradiative rates ($\gamma_{i,nr}$) with $i = \{F, D\}$. The coupling is represented by γ_c , the capture rate of free to bound excitons, and γ_e , the rate for the dissociation of the (D^0, X_A) complex and the subsequent return of the exciton to its free state. This rate equation system can be solved analytically, which yields the time-dependent densities for both states:

$$n_F(t) = \frac{n_F^0}{2\beta} \left[(\beta - \delta) e^{-\frac{1}{2}(\alpha - \beta)t} + (\beta + \delta) e^{-\frac{1}{2}(\alpha + \beta)t} \right] \quad (5.6)$$

$$n_D(t) = \frac{\gamma_c n_F^0}{\beta} \left[e^{-\frac{1}{2}(\alpha - \beta)t} - e^{-\frac{1}{2}(\alpha + \beta)t} \right], \quad (5.7)$$

with

$$\alpha = \gamma_c + \gamma_e + \gamma_D + \gamma_F, \quad (5.8)$$

$$\beta = \sqrt{\alpha^2 - 4[\gamma_e \gamma_F + \gamma_D(\gamma_c + \gamma_F)]}, \quad (5.9)$$

$$\delta = \gamma_c - \gamma_e - \gamma_D + \gamma_F. \quad (5.10)$$

The time-dependent densities [Eqs. (5.6)–(5.7)] are governed by two exponentials with

5.4. Investigating the origin of the short component of the bound exciton decay

different decay constants. The terms proportional to $\exp[-\frac{1}{2}(\alpha + \beta)t]$ describe the increase of the donor-bound exciton population n_D and the simultaneous fast decrease of the free exciton population n_F directly after excitation. At longer times, the system reveals its coupled nature by exhibiting a common effective decay rate, which is represented by the terms proportional to $\exp[-\frac{1}{2}(\alpha - \beta)t]$ in Eqs. (5.6) and (5.7). If donor-bound and free excitons do not couple (i. e., $\gamma_e = 0$), the common decay rate of both states naturally disappears, since $|\beta| - |\delta| = 0$, and the effective decay rates of the free and bound exciton states are given by $\gamma_c + \gamma_F$ and γ_D , respectively, as expected for the uncoupled system.

The solutions of this rate equation system are now employed to gain a deeper understanding of experimental results, especially the magnitude of the effective lifetime, obtained in Secs. 5.4.1 and 5.4.2. For this purpose, two explicit solutions motivated by the experimental results are discussed in the next section.

Explicit solution of the rate equation system for two limiting cases

The dynamics of the coupled system (D^0, X_A) \rightleftharpoons $X_A + D^0$ is invariant with respect to a transformation of the transition rates $(\gamma_c, \gamma_e, \gamma_D, \gamma_F) \rightarrow (\gamma'_c, \gamma'_e, \gamma'_D, \gamma'_F)$, if α , β , and δ remain constant [cf. Eqs. (5.6) and (5.7)]. Such a transformation (apart from the trivial one where all rates remain constant) always exists, and a particular example representing two limiting cases is now discussed.

Let us first consider the situation depicted in Fig. 5.8(a) (hereafter referred to as 'case A'). The free exciton is assumed to have an effective decay rate of $\gamma_F = \gamma_{F,r} = 0.1 \text{ ns}^{-1}$, i. e., equal to its radiative decay rate $\gamma_{F,r}$ estimated in Ref. 59. To account for the experimentally observed rapid decay [cf. Fig. 5.4], the effective decay rate of the donor-bound exciton is set to 7 ns^{-1} , i. e., its decay is mostly nonradiative. The rates determining the coupling are set to $\gamma_c = 40 \text{ ns}^{-1}$ and $\gamma_e = 2 \text{ ns}^{-1}$, representing a comparatively weak coupling (i. e., $\gamma_e \ll \gamma_c$) between the two states.^[170] The resulting time-dependent intensity $\gamma_{F,r}n_F(t)$ of the free exciton and $\gamma_{D,r}n_D(t)$ of the donor-bound exciton are depicted in Fig. 5.8(c). Already 0.1 ns after the generation of free excitons, the (D^0, X_A) and X_A states decay with a common lifetime of about 0.15 ns, in agreement with the experimental result presented in the inset of Fig. 5.4. Note that the time resolution of 50 ps impedes the observation of the fast capture process of the free excitons.

Next, it is assumed that the (D^0, X_A) decay is purely radiative, implying that $\gamma'_D = \gamma_{D,r} = 1 \text{ ns}^{-1}$ (hereafter referred to as 'case B'). It is also demanded that the effective rate

	γ_F	γ_D	γ_c	γ_e	α	β	δ
Case 'A'	0.1	7	40	2	49.1	35.9	31.1
Case 'B'	30.1	1	10	8	49.1	35.9	31.1

Table 5.2: Parameters used in the rate equation model [Eqs. (5.4)–(5.5)] to compute the PL transients shown in Fig. 5.8(b) and the effective rate constants given by Eqs. (5.6)–(5.7), all in ns^{-1} .

5. Investigating the origin of the fast decay of bound excitons in GaN nanowires

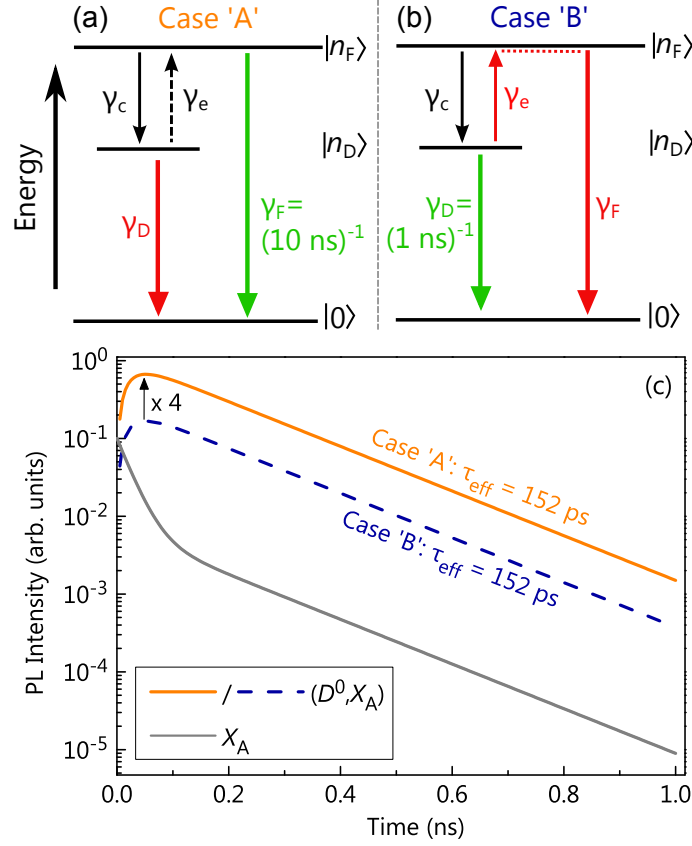


Figure 5.8: (a) and (b) Schematic energy diagrams visualizing Eqs. (5.4) and (5.5) for the two different cases 'A' and 'B', respectively. The two states involved are denoted by $|n_i\rangle$, and the crystal ground state is represented by $|0\rangle$. The red arrows symbolize the effective decay channel, which dictates the dynamics of the coupled system, while green arrows represent purely radiative transitions. (c) Simulated TRPL transients of the (D^0, X_A) and X_A transition given by their respective time-dependent PL intensity $\gamma_{i,r}n_i$, employing the effective decay rates γ_i as summarized in Tab. 6.1 and radiative decay rates $\gamma_{i,r}$ for the free and bound exciton of 0.1 and 1 ns^{-1} , respectively. [Reprinted figure with permission from Hauswald *et al.*^[164]. Copyright 2014 by the American Physical Society.]

constants α , β , and δ have to remain constant, which yields three algebraic equations for the three remaining rates γ'_c , γ'_e , and γ'_F . The resulting equation system has one and only one solution, which is given in Table 5.2. As expected from the equal values for the effective rate constants α , β , and δ , the decay times obtained are identical for cases 'A' and 'B' as illustrated by the simulated transients in Fig. 5.8(c). However, the system of case 'B' is now strongly coupled (i. e. $\gamma_e \lesssim \gamma_c$), and the nonradiative recombination takes place indirectly via the free exciton state as $\gamma_F \approx \gamma_{F,\text{nr}} = 30.1 \text{ ns}^{-1}$ [cf. Fig. 5.8(b)].

The two limiting cases 'A' and 'B' are mathematically distinguishable, since the intensity ratio of the free and bound exciton transitions changes. This change is due to the fact that $n_D(t)$ is proportional to γ_c . However, distinguishing cases 'A' and 'B' (or any of the infinitely many solutions between these two limiting extremes of purely radiative

5.4. Investigating the origin of the short component of the bound exciton decay

recombination of either the free or the bound exciton) based only on the investigated of the (D^0, X_A) and X_A states will be difficult in practice, if not impossible. The reason for this fact is that the experimentally accessible PL intensity is proportional to the *external* quantum efficiency. The intensity ratio of the free and bound exciton transitions is thus influenced by the different extraction efficiencies for the emission from free and bound excitons, which in turn are caused largely by the reabsorption of the free-exciton emission, but also by the different spatial distributions of the emitters.^[26] Additionally, the collection efficiency will be affected by the different far-field patterns of the respective modes within the NWs^[27,156] [cf. also Sec. 7.4.1].

In general, one will thus not be able to determine the individual decay rates of the states participating in recombination, but is left with the effective decay rate of the coupled system. Particularly, the coupled system may decay via either of its constituent states (or even a combination of both) without giving the experimentalist the possibility to decide which path was actually taken. In other words, the $(D^0, X_A) \rightleftharpoons X_A + D^0$ coupled system should be viewed as one entity, and a distinction between the free and bound states based on their dynamics is not physically meaningful. It is now clear why the intuitive model presented in Sec. 5.3 was predicting a very different amplitude for the short decay component as it was assuming the (D^0, X_A) state has a strictly independent dynamics merely determined by its immediate surrounding without taking into account that the (D^0, X_A) effectively probes a much larger volume of the crystal due to the coupling with the free exciton state. Given this result, a revision of the influence of the surface-to-volume ratio on the PL transients in GaN NWs is needed and will be performed in the following Sec. 5.4.4.

At first glance, the apparent coupling of the exciton states suggested by the results of the previous sections is surprising given the low measurement temperature of 10 K. Corfdir *et al.*^[89] attributed the parallel temporal evolution of the X_A and (D^0, X_A) states in GaN NWs at a nominal lattice temperature of 8 K to an enhanced thermal dissociation of bound excitons due to an electronic (carrier) temperature of 35 K deduced from the high-energy tail of the transient spectra. Despite the low excitation density used in the present experiments, similar values are obtained from the exponential high-energy tail of the transient PL spectra immediately after excitation [cf. Sec. 6.4]. However, it is not possible to extract the actual ratio of the rates γ_e and γ_c , i. e., to quantify the strength of the coupling at this point due to the discussed degree of freedom in the coupled system. A quantitative discussion of the origin of the coupling is thus postponed to the following Chap. 6.

5.4.4. Dependence of the effective lifetime on the surface-to-volume ratio

The discussion in the previous Sec. 5.4.3 has important consequences, particularly with regard to the question of the origin of the nonradiative channel dominating the exciton decay in GaN NWs. In case 'A', the wavefunction of the majority of donor-bound excitons

5. Investigating the origin of the fast decay of bound excitons in GaN nanowires

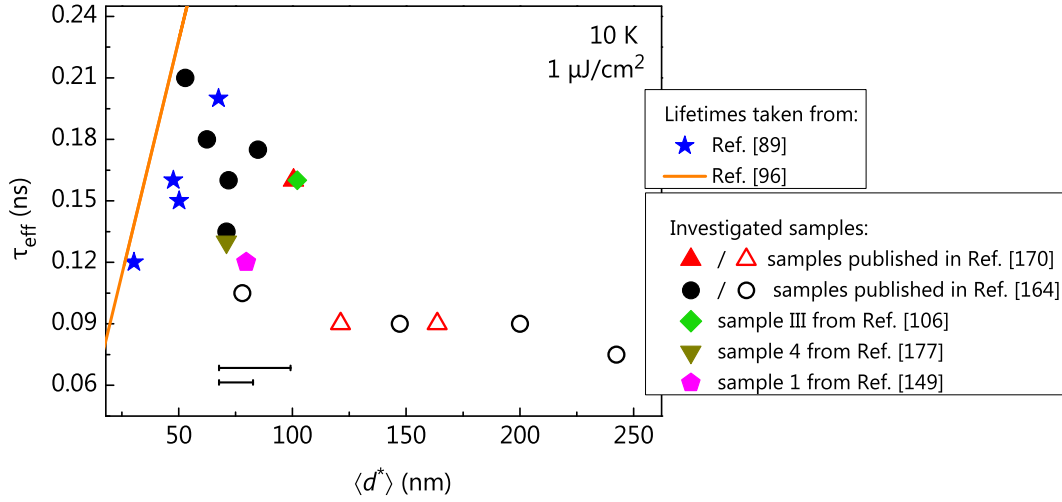


Figure 5.9: Overview of the effective (D^0, X_A) lifetime obtained by fitting the short component of the respective TRPL transient recorded at low temperatures with a single-exponential decay for 19 different GaN NW ensembles and its dependence on the parameter $\langle d^* \rangle$. Solid symbols represent samples grown using the self-induced growth mode, while the open symbols are samples grown by SAG. The horizontal bars indicate the typical standard deviation of the d^* distribution in the NW ensemble for the self-induced growth (upper bar) and SAG (lower bar). The sum of systematic and statistical errors in the determination of the effective lifetimes is estimated to ± 15 ps. The solid line shows the expected dependence with a surface recombination velocity $\tilde{S} = 6.32 \times 10^3$ cm/s as derived in Ref. 96. Besides the investigated samples from Refs. 106, 149, 164, 170, and 177, published values for the (D^0, X_A) lifetime were added from Ref. 89. [Reprinted figure with permission from Hauswald *et al.*^[164]. Copyright 2014 by the American Physical Society.]

has to overlap a nonradiative center to explain the experimentally observed transients, thus requiring fairly high densities of these centers since the (D^0, X_A) complex is a localized state with a small spatial extent.^[106] In contrast, the nonradiative decay in case 'B' occurs via the free exciton, which is principally a coherent excitation of the entire NW,^[86] but is also from a classical point of view a spatially delocalized state, which experiences its surroundings on the scale of its diffusion length of 50–200 nm.^[46–48] Considering that these values are actually larger than the radii of the NWs under investigation, it is interesting to compile the decay times of the (D^0, X_A) state for different GaN NW samples and examine the data for a correlation with the mean surface-to-volume ratio.

In the following, the effective lifetime of the coupled (D^0, X_A) \rightleftharpoons X_A system, i. e., the lifetime of the short component of the decay, are compared for a number of GaN NW ensembles with varying $\langle d^* \rangle$ grown in several different MBE machines using different plasma sources. All GaN NW samples were grown on Si(111) substrates relying on either their spontaneous formation [cf. Sec. 3.1] or employing selective-area growth [cf. Sec. 3.1]. The substrate temperatures were in the range of 780 to 835 °C and the Ga/N flux ratio was chosen accordingly to facilitate the growth of NWs.^[126,143] The results

5.4. Investigating the origin of the short component of the bound exciton decay

are displayed in Fig. 5.9 together with data reported previously by Corfdir *et al.*^[89] It is found that the effective lifetimes measured for the samples at low temperatures remain short regardless of the value of $\langle d^* \rangle$. Samples grown in the self-induced growth mode *do not* show a clear trend towards longer lifetimes with increasing $\langle d^* \rangle$, instead the determined lifetimes scatter randomly around 0.16 ns. For samples grown by SAG, an almost constant lifetime of about 90 ps is found independently of their effective diameter d^* . If the effective lifetime τ_{eff} were fundamentally limited by surface recombination of free excitons, the resulting values would be expected to linearly increase with $\langle d^* \rangle$ as explained in Sec. A and mathematically derived in the appendix of Ref 164. The solid line shows the expected dependence with an effective surface recombination velocity of $\tilde{S} = 6.32 \times 10^3$ cm/s as reported by Gorgis *et al.*^[96]. Note that we have not yet observed decay times longer than expected from this value, but only shorter ones. For thin NWs, surface recombination may therefore be the limiting process after all, but for thicker ones, it is clear that a process not related to the surface determines the exciton decay rate within the first ns after excitation.

5.4.5. Dependence of the effective lifetime on the coalescence degree

As pointed out in Sec. 2.2.1, the coalescence of adjacent GaN NWs may introduce structural defects such as basal plane stacking faults and chains of dislocations into the material. In Sec. 5.3, no clear correlation between the *amplitude* of the short decay of the donor bound exciton decay and the coalescence degree of the NW ensemble was found.

Given the new insight obtained in Sec. 5.4.3, it will now be investigated whether a clear correlation exists between the value of the effective *decay time* of the coupled $(D^0, X_A) \rightleftharpoons X_A + D^0$ system and the coalescence degree of the respective GaN NW ensemble. As explained in detail in Sec. A, the coalescence degree σ_C for spontaneously formed GaN NW ensembles is determined based on an analysis of the shape of the top facet of the individual wires. However, this analysis fails for samples grown by selective-area growth as the top facet of these NWs always adopts the shape of the pre-patterned hole in the underlying mask [cf. Sec. A]. Based on the fact that multiple NW nucleation is inevitable for hole sizes larger than 50 nm,^[143] the coalescence degree is set to $\sigma_C = 1$ for samples grown by SAG, although this may overestimate the influence of coalescence for these samples.

Figure 5.10 plots the effective lifetime τ_{eff} of the $(D^0, X_A) \rightleftharpoons X_A + D^0$ system for 13 different GaN NW ensembles versus their coalescence degree σ_C . The determined effective lifetime of spontaneously grown GaN NW ensembles scatters around 150 ps and does not show any obvious trend towards shorter values for higher coalescence degrees. The GaN NW arrays fabricated by SAG exhibit a slightly shorter lifetime between 75 and 105 ps. Samples with a low degree of coalescence are very rarely found,^[178] which means it is hard to judge as this point whether it is not merely coincidence that the sample with the lowest value of σ_C exhibits the longest lifetime. At the same time, samples with very

5. Investigating the origin of the fast decay of bound excitons in GaN nanowires

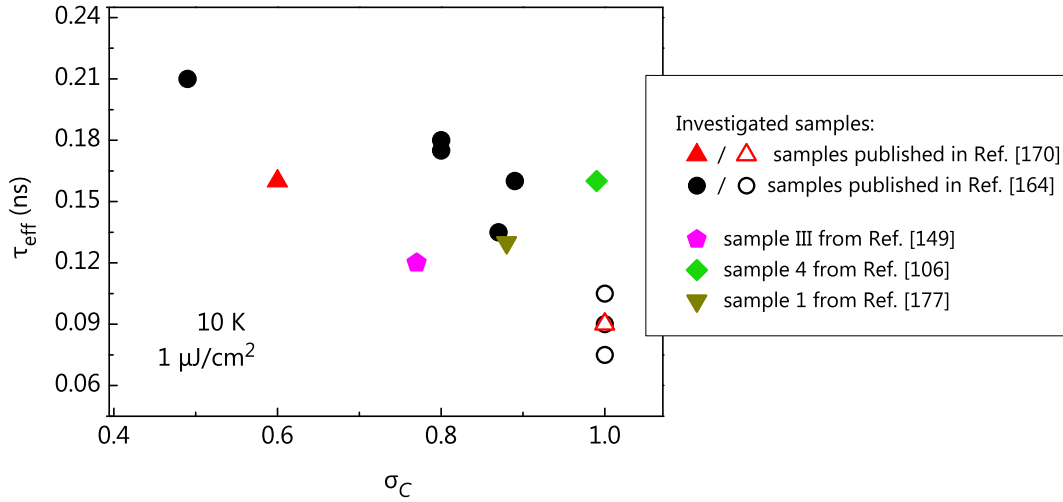


Figure 5.10: Overview of the effective (D^0, X_A) lifetime obtained by fitting the short component of the respective TRPL transient recorded at low temperatures with a single-exponential decay for 12 different GaN NW ensembles in dependence of their coalescence degree σ_C . Solid symbols represent samples grown using the self-induced growth mode, while the open symbols are samples grown by SAG. The sum of systematic and statistical errors in the determination of the effective lifetimes is estimated to ± 15 ps. The investigated samples are described in Refs. 106, 149, 164, 170, and 177. [Reprinted figure with permission from Hauswald *et al.*^[164]. Copyright 2014 by the American Physical Society.]

different σ_C were found to exhibit the same effective decay time. It would certainly be interesting to investigate more GaN NW ensembles with a low degree of coalescence $\sigma_C < 0.5$. However, such samples typically have very small effective diameters around 20 nm, and the recombination of the (D^0, X_A) state is then governed by nonradiative surface recombination.^[96]

5.5. Conclusion

The experimentally observed biexponential PL decay of the (D^0, X_A) state in the investigated GaN NW ensembles cannot be explained by just considering the surface-to-volume ratio or coalescence degree of the NW ensembles. The results of the temperature-dependent cw and TRPL measurements presented in this chapter conclusively show that the dominating, short component of the exciton lifetime in GaN NW ensembles is limited by nonradiative recombination between 10 and 300 K. It is found that this lifetime is independent of the ensembles mean surface-to-volume ratio and coalescence degree, implying that the nonradiative process is neither caused by surface recombination nor by dislocations formed due to NW coalescence. In addition, a combination of both effects seems unlikely as none of the investigated samples exhibits a lifetime longer than 0.21 ns, regardless of its average effective diameter or coalescence degree. The remaining possi-

bility for the origin of this nonradiative channel are point defects. In fact, given that the substrate temperatures used in the MBE growth of GaN NWs are low compared to those used in both metal-organic and hydride vapor phase epitaxy, the point defect density in these NWs is necessarily higher than for state-of-the-art GaN layers, which are grown closer to equilibrium. A straight forward explanation for the fast decay of the localized (D^0, X_A) would be a point defect density above $5 \times 10^{17} \text{ cm}^{-3}$ in the present sample, i. e., the presence of a defect in the vicinity of every (D^0, X_A) state. However, the point defect density does not need to be excessively high for dominating the exciton decay. We demonstrated that bound and free excitons in the investigated GaN NWs are coupled even at low temperatures, and the nonradiative decay may thus take place via the free state if the coupling between the two states is strong enough. Given that the diffusion length of free excitons in GaN is larger than 50 nm, a density as low as 10^{15} cm^{-3} may suffice to introduce an effective nonradiative decay channel.

The origin of the slower, much weaker component of the biexponential PL decay in GaN NW ensembles remains elusive at this point and will thus be investigated in more detail in the following chapter together with a quantitative analysis of the strength of the observed coupling between different excitonic states in GaN NWs.

Origin of the biexponential exciton decay transient in GaN nanowires

The origin of the slow component of the biexponential PL decay observed for GaN NW ensembles is investigated. At long times, the individual donor- and acceptor-bound exciton transitions decay with a common lifetime at low temperatures. After a spectral overlap of neighboring transitions is excluded as the origin of this effect, a coupling between those states, facilitated by the coupling of free and donor-bound excitons discussed in the previous chapter, is considered. A system of non-linear rate equations taking into account this coupling directly reproduces the experimentally observed biexponential decay transients. The magnitude and origin of the coupling is discussed in detail, and it is shown that the presence of this coupling at low temperatures depends on the binding energy of the excitonic complex. Finally, we conclude that the donor-bound exciton complex in GaN NWs is not decaying nonradiatively at point defects in its direct vicinity, but the nonradiative decay occurs indirectly, mediated via its strong coupling to the free exciton state. Some of the results presented in this chapter have been published in Ref. 170.

6.1. Motivation: PL transients of the investigated GaN NW ensembles

In Chap. 5, a biexponential decay behavior of the (D^0, X_A) complex for GaN NW ensembles was found [cf. Fig. 5.3]. The dominating fast component of this biexponential decay is attributed to nonradiative recombination at point defects, either *directly* via a defect in the vicinity of every (D^0, X_A) complex or *indirectly* via the X_A state. The origin of the slower component of the (D^0, X_A) decay, which was observed also by other groups,^[89,97,98] remains unclear up to this point and is investigated now in detail.

We choose three different GaN NW ensembles (hereafter called samples I, II, and III) which exhibit a pronounced biexponential decay of the (D^0, X_A) state with strongly differing short and long decay times for the two components for the analysis. Note that a large signal-to-noise ratio is required to observe the slower component of the decay, which typically has an intensity two orders of magnitude lower than the dominating

6. Origin of the biexponential exciton decay transient in GaN nanowires

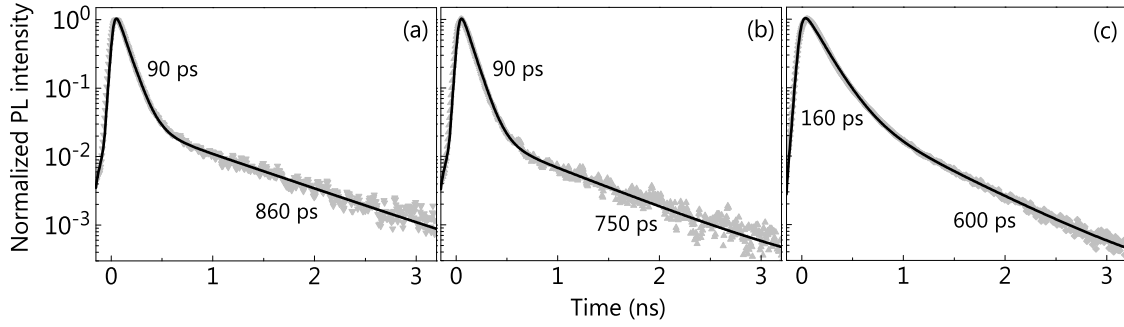


Figure 6.1: Low-temperature PL transient of the (D^0, X_A) transition obtained for (a) sample I, (b) sample II, and (c) sample III [cf. the corresponding SEM images in Fig. 6.2]. The decay times given next to the transients have been extracted by a fit (solid line) of the experimental data with a biexponential decay convoluted with the system response function. [Reprinted figure with permission from Hauswald *et al.*^[170]. Copyright 2013 by the American Physical Society.]

short component. This can be achieved by employing the described post-process methods for the streak camera images described in Sec. 3.3 to remove the contributions from various background signals and enhance the signal-to-noise ratio.

Figure 6.1(a)–6.1(c) display the PL transients of the three GaN NW ensembles integrated over a spectral window of 5 meV width centered at the (D^0, X_A) transition energy. The PL intensity follows a clear decay and remains virtually unchanged when varying the width of the spectral window between 2 and 20 meV. The two components of the transients differ significantly in their decay time and the integrated intensity is dominated by the short component, accounting for 85%, 90%, and 85% of the total intensity for samples I, II, and III, respectively.

The three GaN NW ensembles were synthesized by plasma-assisted molecular-beam epitaxy on Si(111) substrates and Fig. 6.2 displays top-view scanning electron micrographs of the GaN NW ensembles. Samples I and II were obtained by selective-area growth [cf. Sec. 3.1] and contain spatially ordered arrays of GaN NWs with a pitch of 360 nm and well-defined diameters $\langle d^* \rangle$ of 121 and 164 nm, respectively. Sample III is a representative example of a self-induced GaN NW ensemble characterized by a high density of NWs with random position and a broad diameter distribution with a mean of 100 nm. Taking into account the average NW diameter of the three ensembles, and comparing the determined effective decay times of the short component [cf. Fig. 6.1], confirms again the result from Chap. 5, namely, that the NW surface is not the origin of the fast decay component. Moreover, the decay time of the long component does also not correlate with the average diameter for the investigated samples.

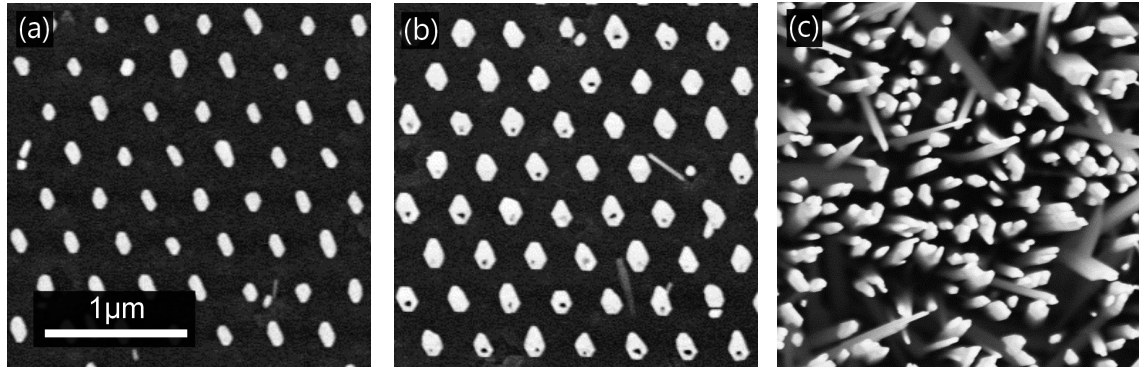


Figure 6.2: Top-view scanning electron micrographs of (a) sample I, (b) sample II, and (c) sample III exhibiting average NW diameters $\langle d^* \rangle$ of 121, 164, and 100 nm, respectively. The images have been taken by A.-K. Bluhm.

6.2. Spectral properties in cw and transient photoluminescence spectroscopy

We investigate the cw and transient spectral properties of these three GaN NW ensembles. Figures 6.3(a)–6.3(c) show the cw μ -PL spectra of the three samples on a logarithmic intensity scale. The dominant transitions in all spectra originate from the recombination of A excitons bound to neutral O and Si donors at (3.4713 ± 0.0001) [(O⁰, X_A)] and (3.4721 ± 0.0001) eV [(Si⁰, X_A)], respectively. As expected for the comparatively large NW diameters, we do not observe a contribution from excitons bound to surface donors.^[84] The observed linewidth of about 1 meV for both transitions is thus determined by the residual microstrain within the GaN NWs.^[150,151] In addition to these dominant (D⁰, X_A) transitions, all three samples exhibit a narrow line at 3.467 eV stemming from the recombination of A excitons bound to neutral acceptors [(A₁⁰, X_A)].^[21,30] Samples I and II exhibit an extra set of lines between 3.455 and 3.463 eV [(A₂⁰, X_A)], which we attribute to the recombination of excitons bound to the deeper acceptor states identified recently.^[21,90,179] The origin of this deep acceptor in the present samples is unknown, but is possibly related to a contamination of the substrates during the process of pre-patterning. Finally, a shoulder due to the recombination of B excitons bound to neutral donors [(D⁰, X_B)] at 3.475 eV and of free A excitons (X_A) at 3.478 eV is observed in all samples.

We next examine the transient PL spectra of the samples. Figures 6.4(a)–6.4(c) show the respective streak camera images obtained after pulsed excitation. The images are color-coded on a logarithmic scale, where a red (blue) color corresponds to a high (low) intensity, respectively. Immediately after excitation and up to a time of about 0.5 ns, the (D⁰, X_A) transition clearly dominates all three spectra. For longer times, luminescence originating from the recombination of excitons bound to neutral acceptors dominate the spectra, i. e., their decay is significantly slower than that of the (D⁰, X_A) transition.

6. Origin of the biexponential exciton decay transient in GaN nanowires

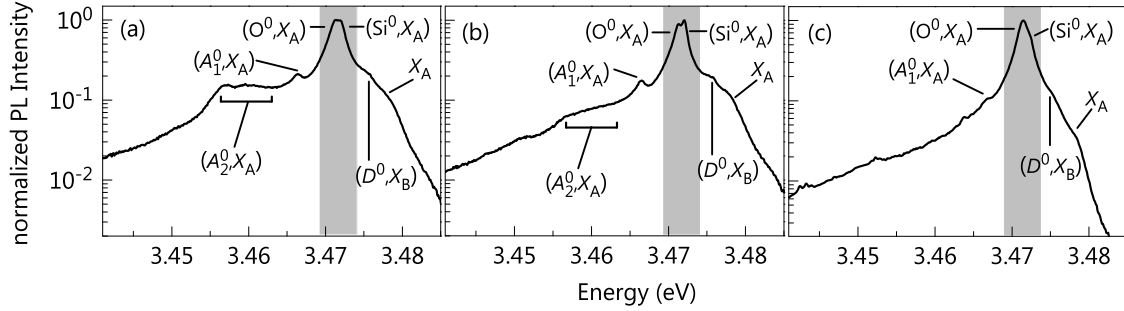


Figure 6.3: Low-temperature cw μ -PL spectrum of (a) sample I, (b) sample II, and (c) sample III. The spectra in (a)–(c) are dominated by transitions due to donor-bound excitons $[(D^0, X_A)]$, but also acceptor-bound $[(A^0, X_A)]$ and free (X_A) exciton transitions are observed. The shaded areas indicate the spectral range of integration used for obtaining the TRPL transients displayed in Fig. 6.1. [Reprinted figure with permission from Hauswald *et al.*^[170]. Copyright 2013 by the American Physical Society.]

This result can be inspected more closely in Figs. 6.4(d)–6.4(f), which display transient spectra extracted from the streak camera images at three different times after excitation, namely, at $t_1 = 180$, $t_2 = 500$, and $t_3 = 1,350$ ps. Between t_1 and t_2 , the (D^0, X_A) transition for samples I and II decreases in intensity by an order of magnitude with respect to the (A_2^0, X_A) transition. Between t_2 and t_3 , however, the intensity ratio between these two transitions remains the same, i. e., they decay with a common time constant at long times. For sample III [Fig. 6.4(f)], we observe a qualitatively similar behavior, but the (A_1^0, X_A) transition becomes comparable in intensity with the (D^0, X_A) transition only at longer times (> 3 ns). The transient spectra shown in Figs. 6.4(d)–6.4(f) reveal a significant spectral overlap of the (D^0, X_A) and (A^0, X_A) lines. Even with the narrow spectral window used to obtain the transients shown in Figs. 6.1(a)–6.1(c), it is inevitable that we monitor a superposition of the corresponding transitions. Since the (A^0, X_A) transitions have a longer decay time than the (D^0, X_A) state, which is visible in Fig. 6.4, the biexponential decay may thus be interpreted as being simply due to the spectral overlap of these lines. The decay times of the two components of the transient would then correspond to the lifetime of the transition dominating the spectrum in a given time interval.

To examine this interpretation, we extract a series of transient spectra from the streak camera images and fit them by a sum of Voigt functions (three for samples I and II, four for sample III) as shown by the black lines in Figs. 6.4(d)–6.4(f). This spectral deconvolution allows us to explore the decay dynamics of each radiative recombination channel *separately* [cf. Sec. 5.4.1]. The data presented in Fig. 6.5(a)–6.5(c) shows the time-dependent intensities of each transition as obtained by the deconvolution. While the (A_1^0, X_A) and (A_2^0, X_A) transients are monoexponential, the (D^0, X_A) transient is still clearly biexponential. This behavior is thus *not* caused by the spectral overlap, and the above naive interpretation of the decay times of the two components of this transient is incorrect.

6.3. Modeling with a system of nonlinear rate equations

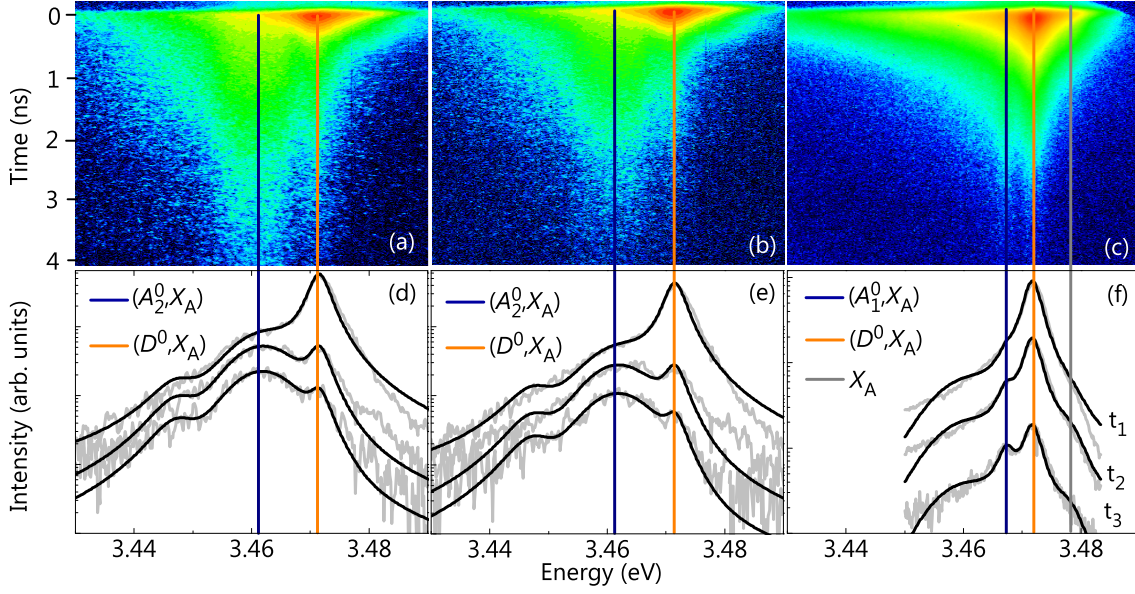


Figure 6.4: Streak camera image and transient PL spectra of sample I [(a) and (d)], sample II [(b) and (e)], and sample III [(c) and (f)], respectively. The intensity in the streak camera images (a)–(c) is displayed on a logarithmic scale from blue (low intensity) to red (high intensity). The spectra [gray lines in (d)–(f)] are extracted from these images at times $t_1 = 0.18$, $t_2 = 0.5$, and $t_3 = 1.35$ ns after excitation and are also displayed on a logarithmic intensity scale. Lineshape fits (black lines) to the experimental data allow us to perform a spectral deconvolution of the transitions (the X_A transition can be reliably fit only for sample III, for which its signal-to-noise ratio is comparatively high). The vertical lines represent the spectral positions of the individual transitions determined from the PL measurements presented in Fig. 6.3. [Reprinted figure with permission from Hauswald *et al.*^[170]. Copyright 2013 by the American Physical Society.]

Evidently, the PL decay of the (D^0, X_A) and (A^0, X_A) states is parallel at long times, suggesting that these states are coupled. Furthermore, for sample III the strong coupling between the (D^0, X_A) and X_A states found in the previous chapter is confirmed by their parallel PL decay. Note that the signal-to-noise ratio of the X_A transition in samples I and II is too low to reliably extract its intensity by a deconvolution.

6.3. Modeling with a system of nonlinear rate equations

The deconvolution of the different PL transitions revealed that the (D^0, X_A) and (A^0, X_A) transients are strictly parallel at long times. In Sec. 5.4.1, a parallel decay was found for the X_A and (D^0, X_A) states in sample R and is reproduced here for sample III. These transitions thus exhibit a common decay time, suggesting a coupling between all states participating in radiative recombination. To facilitate a quantitative analysis of the data,

6. Origin of the biexponential exciton decay transient in GaN nanowires

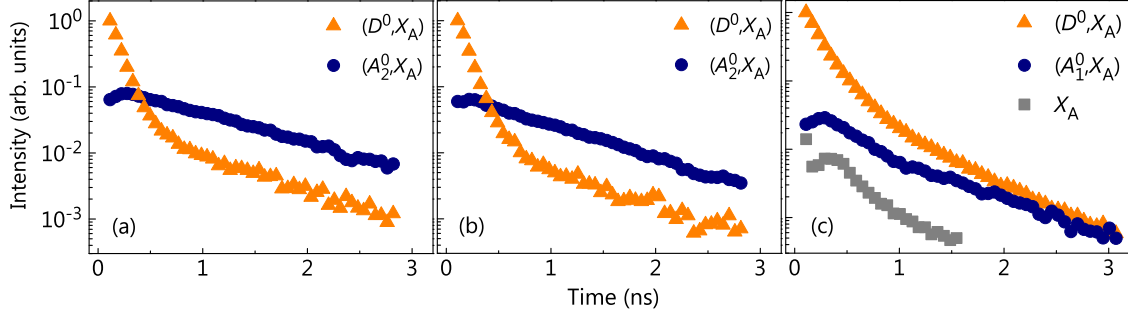


Figure 6.5: PL transients for the (D^0, X_A) (triangles), (A_1^0, X_A) and (A_2^0, X_A) (dots), and X_A [(squares, only in (c))] transitions obtained by the spectral deconvolution of the transient spectra [Fig. 6.4(a)–6.4(c)] for (a) sample I, (b) sample II, and (c) sample III. Each data point corresponds to the deconvoluted PL intensity within a temporally integrated time frame of 50 ps.

now including the (A^0, X_A) state,* and to extract the actual lifetimes of these states, we model the time-dependent densities of the X_A (n_F), (D^0, X_A) (n_D), and (A^0, X_A) (n_A) states by a set of coupled, nonlinear rate equations:†

$$\frac{dn_F}{dt} = -b_D n_F (N_D - n_D) - b_A n_F (N_A - n_A) + \hat{\gamma}_D n_D + \hat{\gamma}_A n_A - \gamma_F n_F, \quad (6.1)$$

$$\frac{dn_D}{dt} = b_D n_F (N_D - n_D) - \hat{\gamma}_D n_D - \gamma_D n_D, \quad (6.2)$$

$$\frac{dn_A}{dt} = b_A n_F (N_A - n_A) - \hat{\gamma}_A n_A - \gamma_A n_A, \quad (6.3)$$

with the initial densities $n_F(0) = n_F^0$, and $n_D(0) = n_A(0) = 0$.

The first terms of Eqs. (6.1)–(6.3), which are illustrated in the scheme displayed in Fig. 6.6, describe the capture of free excitons by neutral donors and acceptors with a total density N_D and N_A , respectively, and their respective rate coefficients b_D and b_A . The

*To be more specific, (A^0, X_A) from now on represents the (A_2^0, X_A) transition for samples I and II and (A_1^0, X_A) for sample III

†The complexity of the analytical solution of the corresponding system of linear rate equations describing the coupling of three states prohibits an analysis similar to the one performed in Sec. 5.4.3. Thus, we choose the more general approach of a nonlinear system of rate equations here and employ its numerical solution in the following.

	γ_F	γ_D	γ_A	$\hat{\gamma}_D$	$\hat{\gamma}_A$	$b_D N_D$	$b_A N_A$
Sample I	8	11	0.5	10	0.65	20	2.8
Sample II	8	11	0.6	10	0.60	20	2.0
Sample III	3	7.5	0.4	10	1.3	26	2.8

Table 6.1: Summary of the free parameters, all in units of ns^{-1} , of the rate equation model [Eqs. (6.1)–(6.3)] used for computing the PL transients shown in Fig. 6.7.

6.3. Modeling with a system of nonlinear rate equations

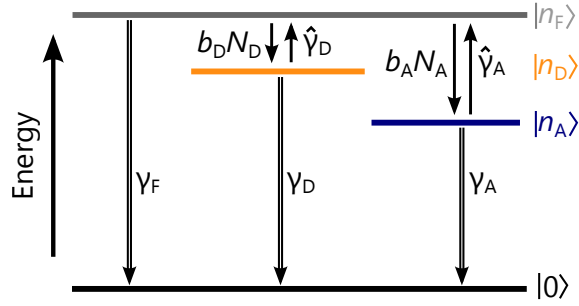


Figure 6.6: Schematic energy diagram visualizing Eqs. (6.1)–(6.3). The involved states are denoted by $|n_i\rangle$, and the crystal groundstate is represented by $|0\rangle$. [Reprinted figure with permission from Hauswald *et al.*^[170]. Copyright 2013 by the American Physical Society.]

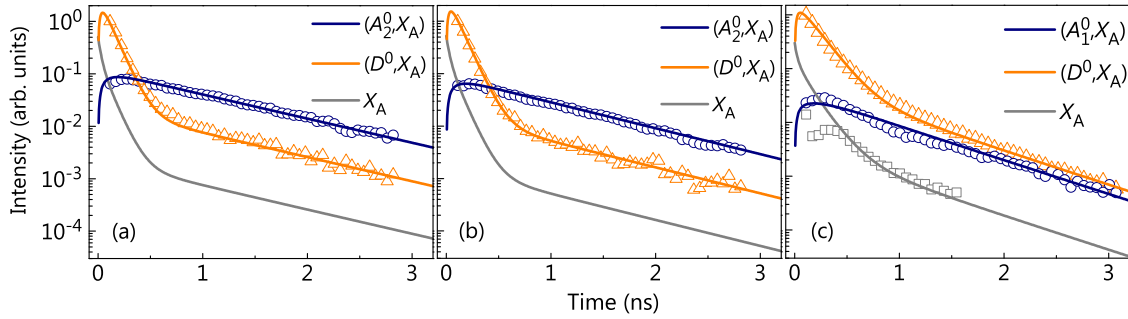


Figure 6.7: The same data as displayed in Fig. 6.5, now overlapping with one solution of the rate equation model Eqs. (6.1)–(6.3) representing the decay of these transitions. The fast initial decay (50 ps) of the free exciton is caused by its capture by neutral donors and acceptors. Note the common decay time of all transitions at longer times, which is a signature of their coupling. [Reprinted figure with permission from Hauswald *et al.*^[170]. Copyright 2013 by the American Physical Society.]

second terms account for the dissociation of the bound excitons with the rate constants $\hat{\gamma}_D$ and $\hat{\gamma}_A$ and the third ones for the recombination of free and bound excitons with the rate constants γ_F , γ_D , and γ_A . These rate constants implicitly contain radiative ($\gamma_{i,r}$) and nonradiative ($\gamma_{i,nr}$) contributions.

The PL intensity of each transition is then given by $\gamma_{i,r} n_i$ as the radiative rate constant $\gamma_{i,r}$ directly determines the peak intensity of the transient [cf. Sec. 5.4.3].^[175] To reproduce the experimentally observed peak intensities of the different transitions for each sample, we again assume a radiative lifetime for the (D^0, X_A) of $\gamma_{i,r}^{-1} = 1$ ns, which in turn sets the radiative lifetimes for the X_A , (A_1^0, X_A) , and (A_2^0, X_A) transitions to 10, 7.7, and 5.5 ns, respectively.^[59] The free parameters of our model are the rate constants γ_i for recombination, $\hat{\gamma}_i$ for the dissociation of bound excitons, and the rate constants for the capture of free excitons ($b_i N_i$). The solid lines in Fig. 6.7 depict the simulated PL transients based on a numerical solution of Eqs. (6.1)–(6.3) using values for the free parameters as summarized in Tab. 6.1. Evidently, the rate equation model is able to reproduce the experimental PL transients for all samples.

6. Origin of the biexponential exciton decay transient in GaN nanowires

The (D^0, X_A) , (A_1^0, X_A) , and (A_2^0, X_A) states can be depopulated not only by recombination, but also by dissociation of the bound into the free state as depicted in Fig. 6.6. The experimentally observed decay times are thus not necessarily equal to the actual lifetimes of these states. The fast component of the PL decay of the (D^0, X_A) state is again determined by the effective decay rate of the $(D^0, X_A) \rightleftharpoons X_A + D^0$ system [cf. Sec. 5.4.3]. The slow component in the PL transient of the (D^0, X_A) and X_A transitions is caused by a re-population of these states due to their coupling with acceptor-bound excitons, resulting in the common lifetime of all states at longer times. In this particular case, the decay rate of the (A^0, X_A) state is approximately given by $\gamma_A + \hat{\gamma}_A$ and thus results from the simultaneous dissociation and recombination of the (A^0, X_A) complex. The results from the numerical solution of the model and the origin of this coupling are discussed in detail in the following section.

6.4. Discussion of the simulation results and origin of the coupling

In order to elucidate the origin of the observed coupling, we now investigate the particular solution found for the coupled rate equation system given by the parameters summarized in Tab. 6.1 and compare the result to estimations based on classical approximations. Due to the low excitation density in the experiment, we remain in the small-signal regime such that $N_i > n_i$. Assuming that all incident light is absorbed by the NWs, the upper limit of the photogenerated carrier density in all samples is estimated to be about 10^{16} cm^{-3} . Thus, the product $b_i N_i$ approximates the capture dynamics of free excitons very well. To estimate this capture rate, we approximate the rate coefficient b_D by the product of the scattering cross section σ_D of a neutral donor and the thermal velocity v_{th} of free excitons:

$$b_D \approx \sigma_D v_{\text{th}} = \pi a_B^2 \sqrt{\frac{3kT}{M}}. \quad (6.4)$$

Here, $a_B = 5 \times 10^{-7} \text{ cm}$ is the exciton Bohr radius of the (D^0, X_A) state, $M = m_0$ the sum of effective electron ($0.2 m_0$) and hole ($0.8 m_0$) masses and k_B the Boltzmann constant. Assuming a temperature of $T = 10 \text{ K}$ and a concentration of neutral donors $N_D = 2 \times 10^{16} \text{ cm}^{-3}$, the capture rate is $b_D N_D = 4 \times 10^{11} \text{ s}^{-1}$, which corresponds to a capture time of 25 ps. This classical estimation is of the same order of magnitude as the experimentally observed rise times of the respective (D^0, X_A) PL lines of about 50 ps. In order to bind to a neutral impurity, the free exciton has to lower its energy by an inefficient scattering process with acoustic phonons. To form the (A^0, X) complex, a larger number of those scattering processes is necessary, and accordingly we expect longer rise times for the acceptor-bound complex. Additionally, the expected density of neutral acceptors inside

6.4. Discussion of the simulation results and origin of the coupling

the NW is lower than the one of donors.[‡] This estimation is in qualitative agreement with both the experimentally obtained data [cf. Fig. 6.7] as well as the result of the numeric solution [cf. Tab. 6.1], where the capture time is found to be longer for the (A^0, X_A) state.

Furthermore, as the (D^0, X_A) and X_A states are strongly coupled [cf. the strictly parallel PL transients in Fig. 6.7], we can consider both states to be in quasi thermal equilibrium. A detailed balance consideration [Eq. (6.5)] then yields the ratio χ between free exciton capture ($b_D N_D$) and bound exciton release ($\hat{\gamma}_D$):^[176]

$$b_D N_D n_F = \hat{\gamma}_D n_D \quad (6.5)$$

$$\Leftrightarrow \frac{b_D N_D}{\hat{\gamma}_D} = \frac{n_D}{n_F} = \frac{2N_D}{N_F} \exp\left[\frac{E_D}{kT}\right] := \chi \quad (6.6)$$

Here, the factor two originates from the spin degeneracy, and N_F is the free exciton density of states approximated as a Boltzmann distribution:

$$N_F = \frac{1}{\sqrt{2}} \left(\frac{MkT}{\pi\hbar^2} \right)^{3/2} \quad (6.7)$$

Furthermore, E_D denotes the binding energy of the (D^0, X_A) complex.[§] Considering $E_D = 7$ meV and a sample temperature of 10 K (which is the nominal temperature measured by the thermocouple inside the cryostat), the expected ratio between exciton capture and release at neutral donors is $\chi \approx 10^3$ as depicted in Fig. 6.8. The numerical solution presented in Tab. 6.1, however, predicts a ratio of $\chi = b_D N_D / \hat{\gamma}_D \approx 2$ for all three samples, which is a clear disagreement. According to the calculated ratio presented in Fig 6.8, $\chi \approx 2$ is expected for a temperature of $T \approx 24$ K, which would be significantly higher than the nominal sample temperature of 10 K. Besides the sample temperature, a reduction of the binding energy for the (D^0, X_A) could facilitate the enhanced coupling, a possibility which we will discuss in Sec. 6.4.1. Yet some uncertainty remains as both the capture time and the ratio χ are linear in the concentration of neutral donors, a parameter which is very difficult to access for GaN NWs and can only be estimated for the present samples. The chosen value of $N_D = 2 \times 10^{16} \text{ cm}^{-3}$ is motivated by a planar reference GaN sample grown in the same MBE system, for which an oxygen concentration of $3 \times 10^{16} \text{ cm}^{-3}$ was determined by secondary ion mass spectrometry.

At first glance, a sample temperature higher than the nominal one is the most probable explanation for the determined enhanced dissociation rate of bound excitons. As

[‡]The present GaN NWs are unintentionally doped, but the neutral acceptors in the present GaN NW samples most likely stem from the incorporation of residual Mg atoms which remained in the MBE chamber from previous growth experiments.

[§]The detailed balance consideration (Eq. 6.5) is based on the Saha–Langmuir equation, which describes the likelihood of ionization as a function of the temperature and ionization energy. It was originally developed to explain the spectral classification of stars,^[180] but later also applied to various physical phenomena in condensed matter systems,^[181] including excitons.^[182]

6. Origin of the biexponential exciton decay transient in GaN nanowires

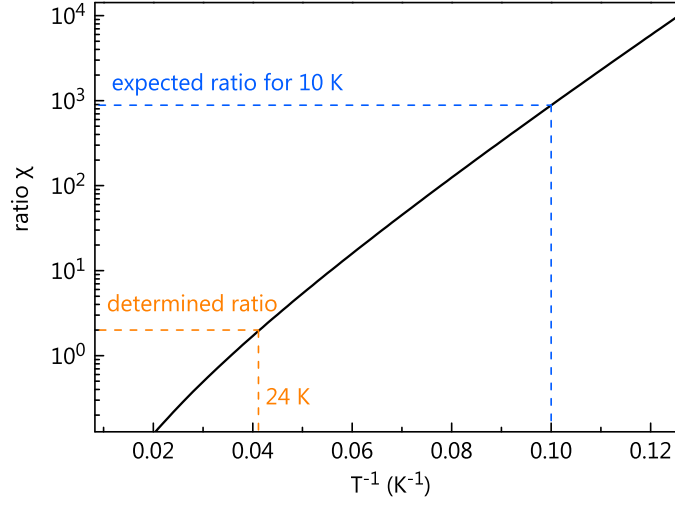


Figure 6.8: Calculated ratio χ between free exciton capture and bound exciton release for the (D^0, X_A) state obtained from a detailed balance consideration of the donor-bound and free exciton populations at quasi thermal equilibrium. The calculation has been performed assuming a concentration of neutral donors of $N_D = 2 \times 10^{16} \text{ cm}^{-3}$ in the GaN NWs.

the latter is expected to change with the binding energy of the respective bound exciton complex, we can employ the ratio

$$\frac{\hat{\gamma}_D}{\hat{\gamma}_A} = \frac{\exp\left(\frac{E_A}{k_B T}\right)}{\exp\left(\frac{E_D}{k_B T}\right)} \quad (6.8)$$

to calculate the necessary temperature which is compatible with the results of the simulation given in Tab. 6.1. In samples I and II, the deep acceptor bound exciton (A_2^0, X_A) with a binding energy of $E_A = 18 \text{ meV}$ is considered, while in sample III the slow decay of the (A_1^0, X_A) state with a binding energy of $E_A = 11 \text{ meV}$ causes the biexponential decay of the (D^0, X_A) . The required sample temperatures are 47, 45, and 23 K for samples I, II, and III, respectively. Again, this temperature is much higher than the nominal temperature of the samples of 10 K.

Unfortunately, the sample temperature is difficult to access directly in the experiment with sufficient accuracy. However, as donor-bound and free excitons are in quasi thermal equilibrium, we can study the carrier temperature T_{carrier} of the latter. The free exciton population is described by a Maxwell-Boltzmann distribution, which is directly accessible investigating the high energy side of the PL spectra $I(E)$ using an exponential decay to fit the data:

$$I(E) = y_0 + I_0 \exp\left[\frac{-(E - E_0)}{k_B T_{\text{carrier}}}\right] \quad (6.9)$$

6.4. Discussion of the simulation results and origin of the coupling

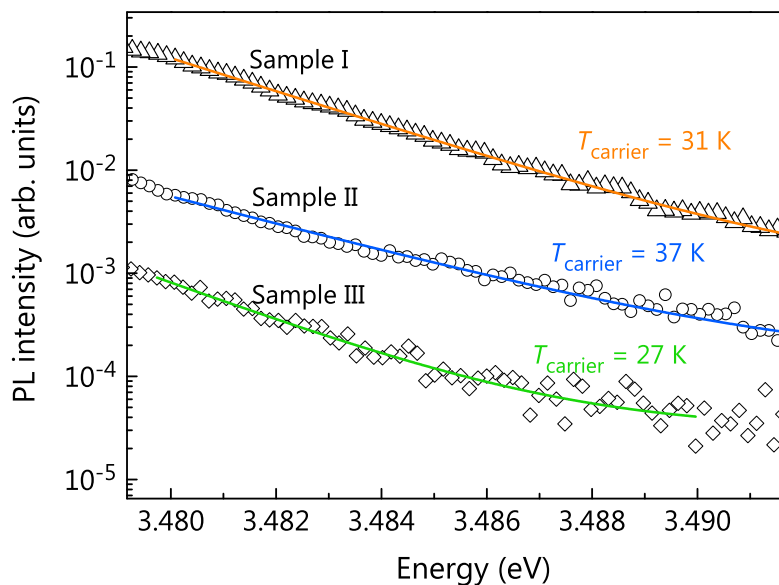


Figure 6.9: High-energy part of the time-integrated PL spectra of sample I, II and III. The solid lines represent a fit to the data using an exponential decay [Eq. (6.9)] yielding the denoted values for the carrier temperature T_{carrier} of the free exciton population.

Here, E_0 and y_0 represent the offsets on the x- and y-axis, respectively, while I_0 denotes the maximum of the PL intensity within the interval of the fit. All three are free parameters for the fit. Figure 6.9 shows a fit to the PL spectra of the three samples under investigation using Eq. 6.9. The obtained values for T_{carrier} of 31, 37, and 27 K for samples I, II, and III, respectively, are indeed significantly higher than the nominal temperature of the cryostat of 10 K. Yet, a sample temperature in the same range was suggested previously for GaN NWs^[89] and also planar GaN^[183] when a cold-finger cryostat was used. Even mounting a sample in a bath cryostat and immersing it in liquid helium resulted a minimum carrier temperature of 25 K for CdSe, independently of the excitation density.^[184]

The deduced values for the carrier temperature agree reasonably well with the predicted temperatures from the model discussed above. Furthermore, the carrier temperature for samples I and II was found to be higher than for sample III, in agreement to the result of the modeling. It thus seems plausible that the enhanced coupling of bound exciton states is caused by an increased sample or carrier temperature during low-temperature PL measurements at nominally $T = 10$ K. While no influence of the excitation density was found, several other possible origins for the increased sample temperature can be imagined. First of all, the samples exhibit strong nonradiative recombination even at these low temperatures [cf. Sec. 5]. Second, the excitation energy of the laser (3.81 meV) is several hundred meV above the bandgap of GaN, thus a large number of longitudinal optical phonons is generated during the cooling of free carriers [cf. Sec. 2.2.1]. Additionally, a technical reason is possible, for example the radiation from the close-by (≈ 5 mm) cryostat window which is at room temperature might slightly heat up the samples.

6. Origin of the biexponential exciton decay transient in GaN nanowires

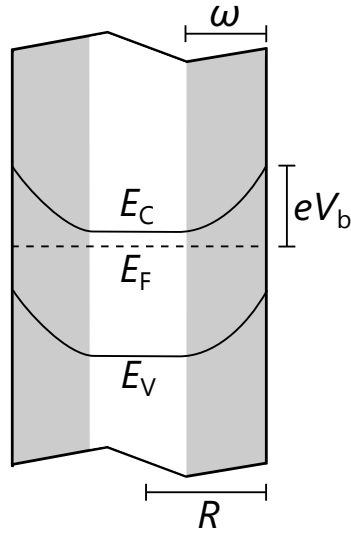


Figure 6.10: Schematic representation of the conduction band (E_C) and valence band (E_V) profiles across a NW induced by the Fermi level E_F pinning at eV_b below the conduction band edge at the NW sidewalls. R is the radius of the NW and ω the width of the depletion region due to the electric field. The latter is visualized by the gray areas.

Another physical reason for the enhanced dissociation rate of bound excitons in GaN NWs is discussed in the following section: the presence of electric fields within the NWs.

6.4.1. Possible impact of the electric fields in GaN NWs

As discussed already in Sec. 2.2.1, GaN NWs exhibit an internal electric field which arises from the pinning of the Fermi level 0.6 eV below the conduction band edge at the NW sidewall M -plane surfaces.^[80,185] It has been shown recently that the corresponding electric potential can be considered parabolic for NWs with a diameter of 80 nm and a donor density of 10^{16} cm^{-3} .^[82] A schematic representation of the conduction and valence band profiles across a GaN NW is shown in Fig. 6.10. The width of the depletion region ω depends on the NW diameter and the density of donors, and the strength of the field amounts to 10 to 17 kV/cm for a moderate doping density of $2 \times 10^{16} \text{ cm}^{-3}$ for the present range of NW diameters.^[62] Fields of this magnitude are theoretically expected to directly ionize the (D^0, X_A) complex^[49,186,187] and have been experimentally found to quench the (D^0, X_A) line in GaN layers due to the dissociation of donor-bound excitons by impact ionization.^[49] In any case, the presence of this electric field lowers the ionization energy of the donor and consequently the binding energy of the (D^0, X_A) complex ('Haynes rule',^[63] cf. Sec. 2.2.1). Thus, the electric field is expected to enhance the dissociation rate $\hat{\gamma}_D$. Note that the magnitude of these fields depends linearly on the NW diameter and doping concentration. Yet, further experiments are necessary to clarify the exact influence of electric fields. However, their effect on the exciton dynamics in these NWs must not be ignored since they are an inherent property of GaN NWs.

6.5. Coupling between other bound exciton states

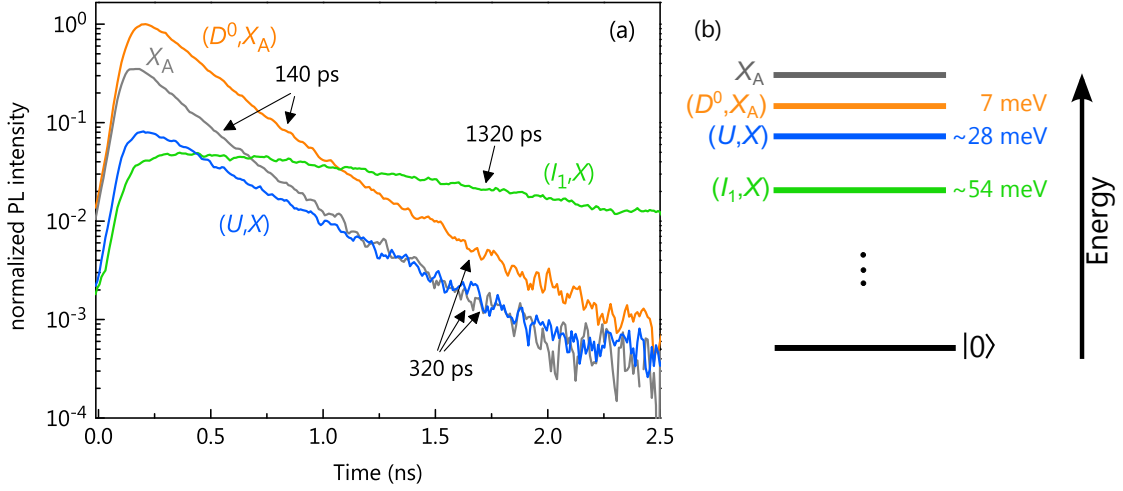


Figure 6.11: (a) Low-temperature PL transients and lifetimes for the denoted transitions of sample R. (b) Schematic energy diagram displaying the energy levels of these transitions. The given values denote the energy difference between the observed recombination energy of the bound and free exciton.

6.5. Coupling between other bound exciton states

Besides the (D^0, X_A) and (A^0, X_A) states, low-temperature PL spectra of GaN NW ensembles reveal the presence of other bound exciton states such as the (U, X) and (I_1, X) [cf. Fig. 5.4.1]. We will now investigate the PL dynamics of these states after pulsed excitation and clarify whether they are also coupled to the X_A state at low temperatures.

Figure 6.11 depicts the low-temperature PL transients of several excitonic transitions in sample R. As already pointed out in Sec. 5.4.1, the decay of the strongly coupled $(D^0, X_A) \rightleftharpoons X_A + D^0$ system is biexponential with a short decay time of 140 ps and a longer component of 320 ps. The PL transient of the (U, X) transition is well described by a monoexponential decay with an effective decay time of 320 ps. This common lifetime at longer times strongly suggests that the slow component of the decay of the $(D^0, X_A) \rightleftharpoons X_A + D^0$ system is caused by a re-population of these states by the (U, X) complex in this specific sample, similarly to what has been found for the (A^0, X_A) state in other GaN NW ensembles in Sec. 6.3. However, the origin of the (U, X) line is not completely clarified yet and several different transitions are overlapping at this energy [cf. Sec. 2.2.1]. Thus, a quantitative investigation of the coupling of the (U, X) state is rather speculative for the present sample. Yet, exploring the coupling of the (U, X) and X_A states in samples where the separate contributions to the 3.45 eV-band are better resolved^[91] can potentially shed new light on the origin of this still elusive transition.

Notably, the PL transient of the (I_1, X) complex in sample R exhibits a monoexponential decay with an effective decay time of 1,320 ps as shown in Fig. 6.11. This value is almost ten times larger than the effective lifetime of the coupled $(D^0, X_A) \rightleftharpoons X_A + D^0$ system, which suggests that the (I_1, X) are much less affected by the nonradiative chan-

6. Origin of the biexponential exciton decay transient in GaN nanowires

nel. Indeed, a constant emission intensity of the (I_1, X) accompanied with an increase of the effective decay time for this state between 10 and 60 K in GaN NWs has been recently observed.^[91] The simultaneous occurrence of these two effects indicates that the recombination of the (I_1, X) is dominated by radiative phenomena in this temperature range.^[188] Between 10 and 60 K, localized excitons inside the stacking fault are subsequently delocalized and can then move freely along the plane of the SF. Above $T = 60$ K the thermal escape of charge carriers from the SF into the wurtzite matrix of the GaN NWs is activated, and an activation energy of 54 meV was determined for this process.^[91]

According to the model presented in Sec. 6.3, the strength of the coupling between a bound exciton state and the free X_A state is expected to depend on the binding energy of the excitonic complex. Consequently, a larger binding energy will reduce the dissociation rate of the complex at a given temperature as discussed in Sec. 6.4. Furthermore, observing a radiative decay of the (I_1, X) state and, at the same time, strongly nonradiative decay of the (D^0, X_A) state in the same GaN NW ensemble^[91] has important consequences for the nonradiative channel revealed in Chap. 5. Up to this point, it was not clear whether the (D^0, X_A) state decays nonradiatively via a point defect in its direct vicinity [cf. case 'A' in Sec. 5.4.3] or indirectly via the free exciton due to a strong coupling with the X_A state [cf. case 'B' in Sec. 5.4.3].

Between 10 and 60 K excitons localized at the SF are free to move along the SF plane which extends through the whole GaN NW, i. e., corresponding to a disk with a thickness of about 8 nm.^[91] As the decay of the (I_1, X) state is purely radiative in this temperature range, this volume must be consequently free of any nonradiative defects. Hence, assuming a random distribution of nonradiative point defects inside the GaN NWs, the radiative decay of the (I_1, X) state sets an upper limit for the density of these point defects to about $6 \times 10^{16} \text{ cm}^{-3}$. Yet, such a low density of point defects cannot explain the nonradiative decay of *every* localized (D^0, X_A) complex, which then excludes case 'A'. We thus conclude that case 'B' represents the more accurate description of the exciton dynamics in GaN NWs under the given experimental conditions, which means the (D^0, X_A) state is strongly coupled to the X_A state for the present sample.

The dominating nonradiative channel in GaN NWs is thus introduced by the X_A state, and a reduced coupling with the X_A state naturally leads to a longer effective lifetime for the respective bound complex, in good agreement with the experimental results found for the different transitions in GaN NWs in this chapter and in Fig. 6.11. In the extreme case of a vanishing coupling probability, a purely radiative decay is expected and observed here for the (I_1, X) state.^[91] Consequently, the (I_1, X) state does not couple to the X_A state under the given experimental conditions in contrast to what is observed for the (D^0, X_A) , (A^0, X_A) , and (U, X) states.

6.6. Conclusion

The detailed investigation of the PL transients of different GaN NW ensembles in this chapter provides an understanding of the origin of the biexponential decay of the (D^0, X_A) transition in these samples. The slow component of the PL decay is caused by a re-population of the (D^0, X_A) state by the (A^0, X_A) complex, which has a longer effective lifetime. The coupling between the two states occurs via the X_A state.

The numerical solution of the rate equation system describing this coupling offers the possibility to quantitatively examine the strength of the coupling. By comparing the rate of free exciton capture to bound exciton release for the different excitonic complexes, we come to the conclusion that the sample temperature in the employed, continuous flow cryostats, is probably higher than the nominal value of 10 K determined by the thermocouple. Besides an enhanced sample temperature, the presence of the electric field inside the GaN NWs can also influence the rate of bound exciton release and thus gives rise to the observed coupling. To unambiguously determine which mechanism is dominant in the present samples, further experiments are necessary. Using lower cryostat temperatures in a defined, thermalized environment might resolve whether technical reasons cause an enhanced lattice temperature in the GaN NWs.[¶] By tuning the energy of the excitation laser, it might be possible to investigate the influence of the hot carriers on the coupling or even minimize the required number of scattering processes with acoustic phonons by exciting the sample exactly at 92 meV (i. e., the energy of a longitudinal optical phonon in GaN) above the bandgap.

Nevertheless, the obtained results allow us to clarify the unresolved question from Chap. 5, namely, whether the observed nonradiative decay of the (D^0, X_A) occurs directly via a defect in its vicinity or indirectly via the free exciton state. While the (D^0, X_A) and X_A states are found to be dominated by a nonradiative channel, the (I_1, X) complex decays purely radiatively in GaN NWs at sample temperatures below 60 K.^[91] This finding sets an upper limit for the density of point defects in GaN NWs to about $6 \times 10^{16} \text{ cm}^{-3}$.^[91] Since such a low density of point defects cannot lead to a nonradiative decay of every (D^0, X_A) complex, the fast recombination dynamics of the latter are caused by its *indirect nonradiative decay at point defects mediated via a strong coupling with the X_A state* for the present samples.

[¶]A defined sample temperature of 2 and 4 K can be achieved using an active bath cryostat where the sample is in direct contact with ^4He in its superfluid (so called λ -point) or liquid phase, respectively.

Internal and external quantum efficiency of ordered arrays of GaN nanowires

In contrast to planar layers, for which the absorbance and extraction efficiency are easily calculated and comparable from sample to sample, both parameters depend strongly on the specific arrangement and dimensions of the nanowires (NWs) and are thus essentially unknown for NW arrays as discussed in Sec. 2.3. Consequently, the PL intensity alone is not a meaningful measure for the internal quantum efficiency of (ordered) GaN NW arrays, and the external quantum efficiency should be considered. Indeed, low-temperature PL investigations on ordered GaN NW arrays reveal puzzling results at first. The obtained PL intensity of the arrays depends strongly on the NW diameter, and surprisingly, arrays with smaller average diameter exhibit the highest PL intensity, while a strong quenching is observed with increasing NW diameter. In order to unravel the origin of this unexpected behavior, we first investigate the internal quantum efficiency of the different ordered GaN NW arrays in Sec. 7.2 and show that it does not depend on the NW diameter in agreement with the results obtained in the previous chapters. We then focus on the investigation of the external quantum efficiency by performing numerical simulations to access the light absorption of regular NW arrays in Sec. 7.3. Finally, the diameter-dependent wave-guiding properties of GaN NWs and the resulting extraction efficiency are explored in Sec. 7.4.

7.1. Motivation: Photoluminescence intensity of ordered GaN NW arrays with different NW diameters

Although several research groups worldwide are working on the selective-area growth of GaN NWs,^[142,143,189,190] only little is known so far about the optical properties of these ordered GaN NW arrays. As of today, only one room-temperature PL spectrum has been published,^[139] but, to our knowledge, low-temperature PL or TRPL data and information regarding the experimentally obtained intensity of different ordered GaN NW arrays grown by MBE or their internal quantum efficiency have not been published so far.

In this chapter, the optical properties of ordered GaN NW arrays of which some are

7. Internal and external quantum efficiency of ordered arrays of GaN nanowires

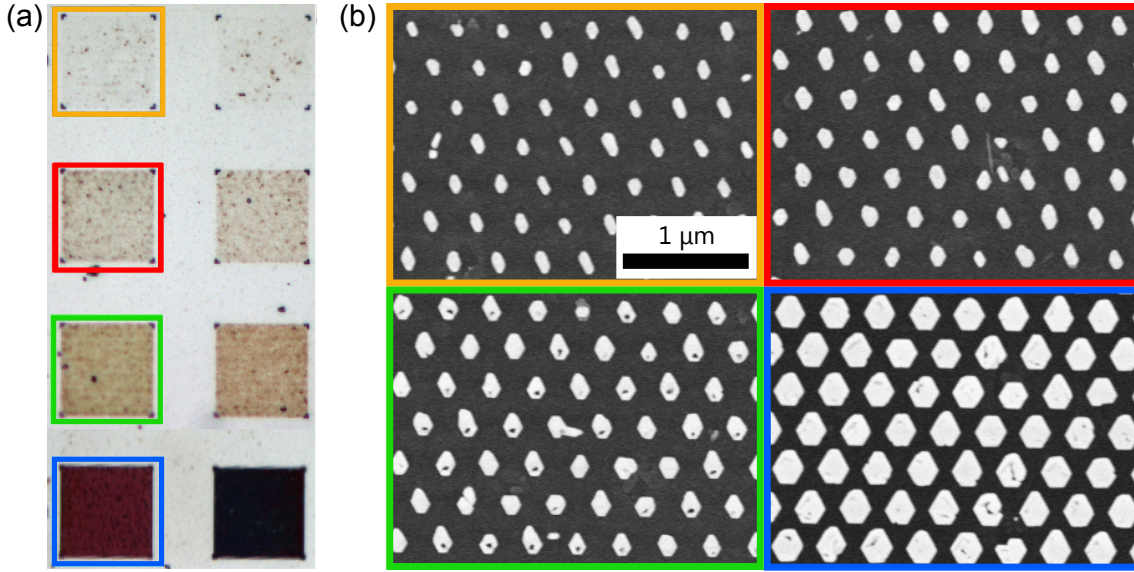


Figure 7.1: (a) Bright-field optical microscope image of ordered GaN NW arrays. Each array has a size of $30 \times 30 \mu\text{m}^2$. (b) Top-view scanning electron micrographs of four of the investigated ordered NW arrays exhibiting average diameters $\langle d^* \rangle$ of 121 nm (marked yellow), 147 nm (red), 164 nm (green) and 242 nm (blue). The pitch $a = 360$ nm between two neighboring NWs is constant for all displayed arrays. The images displayed in (b) have been taken by A.-K. Bluhm.

displayed in Fig. 7.1 are studied. Figure 7.1(a) shows exemplary bright-field optical microscope images of GaN NW arrays which were fabricated by selective-area growth as described in Sec. 3.1. Each array has a size of $30 \times 30 \mu\text{m}^2$, which means that their optical properties need to be investigated with μ -(TR)PL. The pitch between the NWs is $a = 360$ nm in this particular case and an analysis of the top facet of several hundred NW reveals average diameters $\langle d^* \rangle$ of (121 ± 15) nm, (147 ± 14) nm, (164 ± 13) nm and to (242 ± 13) nm for the arrays displayed in the scanning electron micrographs in Fig. 7.1(b). As explained in App. A, the effective diameter d^* is very similar to the equivalent disk diameter of the NWs here due to their hexagonal top facet. The colored frames around the scanning electron micrographs in Fig. 7.1(b) indicate the corresponding bright-field optical microscope image and the same colors are used during the whole chapter to identify the respective NW arrays.

Figure 7.2(a) depicts the low-temperature (10 K) PL spectra of the four ordered GaN NW arrays displayed in Fig. 7.1 and one additional array with the same NW pitch a but $\langle d^* \rangle = 200$ nm. The PL spectra are dominated by the (D^0, X_A) transition, and the separate contributions from O and Si donors are resolved for NWs with $\langle d^* \rangle < 200$ nm. Additionally, the (A^0, X_A) transition is observed at 3.467 eV, and a broad band is found around 3.46 eV, which we attribute to the (A_2^0, X_A) transition [cf. Sec. 6.2].^[21,72,179] The X_A transition is visible as a shoulder at 3.478 eV. The (I_1, X) transition at 3.42 eV is not observed in any of these spectra, indicating that the NWs are essentially free of I_1 stacking

7.1. Motivation: Photoluminescence intensity of ordered GaN NW arrays

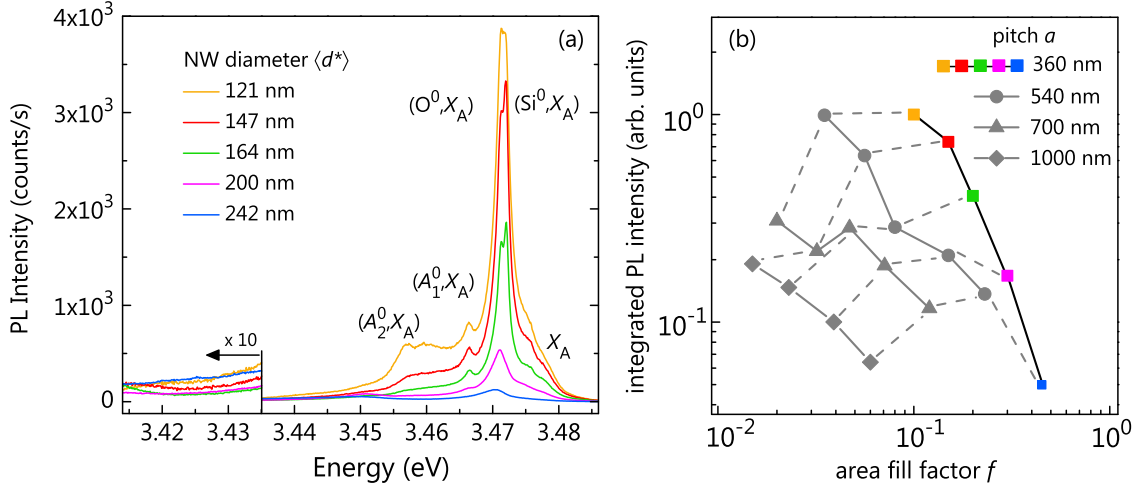


Figure 7.2: (a) Low-temperature (10 K) PL spectra of ordered GaN NW arrays with different average NW diameters. (b) Integrated PL intensity vs. the area fill factor f for 19 different ordered GaN NW arrays. Symbols connected with a solid line represent arrays with a constant pitch a , while dashed line connect arrays with a similar average diameter $\langle d^* \rangle$. The colors indicate the respective arrays from (a).

faults. Evidently, the measured PL intensity is quenched monotonously with increasing NW diameter.

As mentioned in Sec. 2.3, effective medium theory was successfully employed for GaN NW ensembles for the interpretation of experimental data obtained by Raman spectroscopy.^[112,113] Figure 7.2(b) displays the integrated PL intensity (normalized for the array with $a = 360$ nm and $\langle d^* \rangle = 121$ nm) for 19 ordered GaN NW arrays vs. their respective area fill factor f . Evidently, no direct correlation between the integrated PL intensity and the area fill factor f is found, which means that the ordered NW arrays cannot be treated as an effective medium with f as the sole parameter in the present case. Recent studies on the interaction of light with ordered InAs NW^[115] and InP NW arrays^[116] came to the same conclusion. If one considers the excitation and emission wavelength of 325 and 357 nm, respectively, in relation to the NW diameters of about 121 to 242 nm, it makes sense that effective medium theory is not suitable to describe the interaction of light with the NW arrays in the present case.

Measuring a lower PL intensity for arrays with larger NW diameters is somewhat counterintuitive as the PL intensity is expected to scale with the excited volume and should thus increase with the diameter, rather than decrease as observed here. In order to elucidate the origin of this unexpected effect, we consider the different contributions to the measured PL intensity in the experiment. The PL intensity I_{PL} is in general proportional to the external quantum efficiency η_{ext} of the sample:

$$I_{\text{PL}} \propto G\eta_{\text{ext}} = G\eta_{\text{int}}\eta_{\text{extr}}\eta_{\text{coll}} \quad (7.1)$$

7. Internal and external quantum efficiency of ordered arrays of GaN nanowires

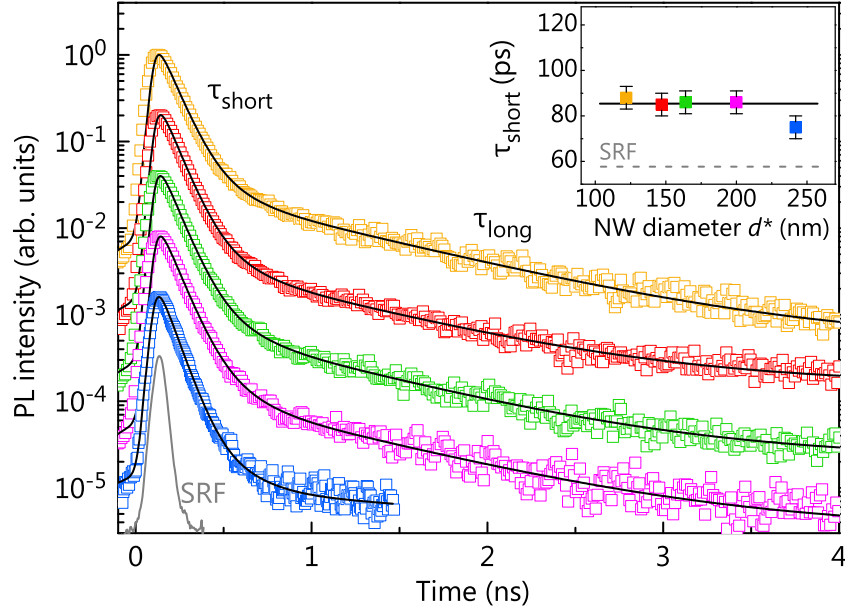


Figure 7.3: Vertically shifted PL transient of the (D^0 , X_A) transition obtained for ordered GaN NW arrays with different average NW diameter: 121 nm (yellow), 147 nm (red), 164 nm (green), 200 nm (magenta) and 242 nm (blue). The solid lines represent a biexponential decay convoluted with the system response function (SRF, shown by the grey line) fitted to the data. The inset depicts the determined value of the short decay time τ_{short} extracted from these fits for different average NW diameters. All decay times are found to be significantly longer than the SRF, which has a FWHM of 58 ps.

where η_{int} is the internal quantum efficiency, η_{extr} the extraction efficiency of the array, and G the carrier generation rate, which is directly proportional to the absorbed light intensity in the GaN NW array. The collection efficiency η_{coll} describes which share of the total extracted intensity is collected by the microscope objective in the experiment. Note that η_{coll} is only constant for a Lambertian radiator, while in general η_{coll} depends on the far-field pattern of the emitted light if the detector is not an Ulbricht sphere. We will explore all of these factors in the following sections for the ordered GaN NW arrays under investigation by a combination of experimental results and numerical simulations.

7.2. Internal quantum efficiency of ordered arrays of GaN nanowires

A straightforward explanation of the decreasing integrated PL intensity of the ordered GaN NW arrays would be a decreasing η_{int} of the GaN NWs with increasing diameter. However, as we already concluded in Chapter 5, the internal quantum efficiency does not depend on the NW diameter or coalescence degree and is essentially constant for different ordered GaN NW arrays [cf. Fig. 5.9].

7.3. Coupling of light into ordered arrays of GaN NWs and subsequent absorption

To illustrate this again for the present ordered GaN NW arrays, Fig. 7.3 shows the low-temperature PL transients of the (D^0, X_A) state in these NWs. The transients follow a biexponential decay with a short lifetime of about 90 ps and a longer component of about 800 ps. Most importantly, the transients are nearly identical for all five investigated arrays. In Sec. 6.3, it has been found that the origin of the long component of the PL decay is a re-population of the (D^0, X_A) state by the (A^0, X_A) state which has a longer effective lifetime. Thus the effective lifetime of the (D^0, X_A) state, which dominates the luminescence at low temperatures [cf. Fig. 7.2], is determined by the short component of the biexponential decay in Fig. 7.3.* Consequently the internal quantum efficiency of the samples at low temperatures [cf. Sec. 2.2.2] is given by:

$$\eta_{\text{int}} = \frac{\tau_{\text{short}}}{\tau_{\text{rad}}} < 10\% \quad , \quad (7.2)$$

with a radiative lifetime τ_{rad} of at least 1 ns for the (D^0, X_A) state in GaN.^[21,22] We conclude that the internal quantum efficiency is low, but essentially similar for the ordered GaN NW arrays under investigation, and hence cannot explain the decrease in PL intensity observed in Fig. 7.2.

7.3. Coupling of light into ordered arrays of GaN NWs and subsequent absorption

Displaying the integrated PL intensity of the ordered GaN NW arrays as a function of the filling factor f of the array in Sec. 7.1 showed that an effective medium approach cannot sufficiently describe the observed effects here. As summarized in Sec. 2.3, the interaction of light with ordered arrays of NWs can be significantly altered depending on the wavelength on the incoming light, the NW dimensions, and their specific arrangement. In the present section, we study the absorption of the laser light by the ordered GaN NW arrays which have been investigated by PL spectroscopy in Sec. 7.1. We perform a complete solution of the Maxwell equations in three dimensions, which enables us to fully cover all effects of the interaction of a light source with the three-dimensional (3D) geometry of the sample without the need of an approximation.

7.3.1. Introductory example: Absorbance of a GaN slab

Prior to employing the 3D-Maxwell solvers described in Sec. 3.4 for calculating the absorption and extraction efficiency of ordered GaN NW arrays, the accuracy of the simulations is validated by comparing the results with the analytical solution for a planar structure. For this purpose, the interaction of a monochromatic plane wave with $\lambda = 325$ nm

*Cf. chapters 5 and 6 for a detailed description of the origin and interpretation of the individual decay times in GaN NW PL transients.

7. Internal and external quantum efficiency of ordered arrays of GaN nanowires

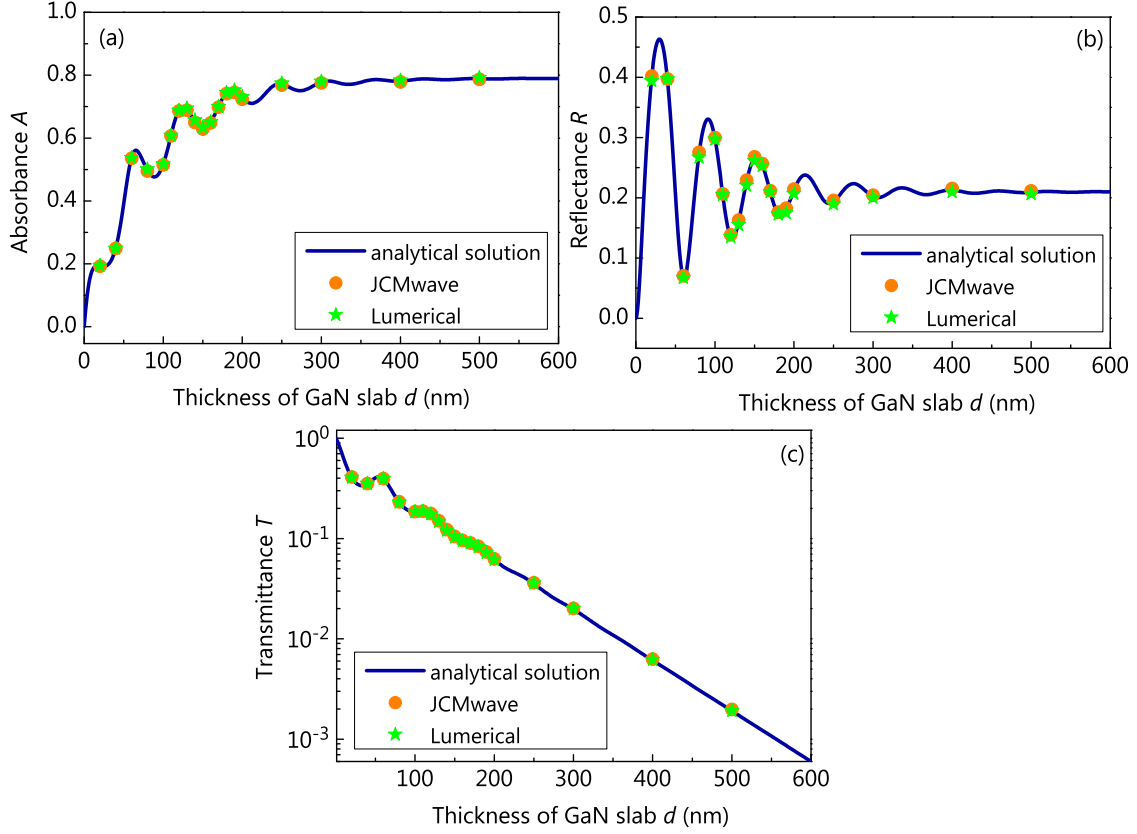


Figure 7.4: Calculated (a) absorbance A , (b) reflectance R and (c) transmittance T of a GaN slab with varying thickness d , surrounded by air and interacting with a plane wave with $\lambda = 325$ nm at normal incidence. The orange circles and green stars show the result obtained by the numerical simulation with JCMWAVE and LUMERICAL, respectively. The solid blue line represents the analytical solution of the problem given by Eqs. 7.3–7.5.

with a GaN slab of thickness d is simulated. The transmittance T , reflectance R , and absorbance A of the slab in vacuum at normal incidence are given by:^[111]

$$T = \left| \cos(\tilde{n}kd) - \frac{i}{2} \left(\tilde{n} + \frac{1}{\tilde{n}} \right) \sin(\tilde{n}kd) \right|^{-2}, \quad (7.3)$$

$$R = \left| \frac{1}{2} \left(\tilde{n} - \frac{1}{\tilde{n}} \right) \sin(\tilde{n}kd) \right|^2 T, \quad (7.4)$$

$$A = 1 - R - T, \quad (7.5)$$

where $\tilde{n} = 2.65 + 0.3i$ is the complex index of refraction of GaN at $\lambda = 325$ nm^[191] and k is the wavenumber of the incident light.

Figure 7.4 shows the result of a 3D FEM simulation with JCMWAVE (orange circles), a 3D FDTD simulation with LUMERICAL (green stars) together with the analytical solution

7.3. Coupling of light into ordered arrays of GaN NWs and subsequent absorption

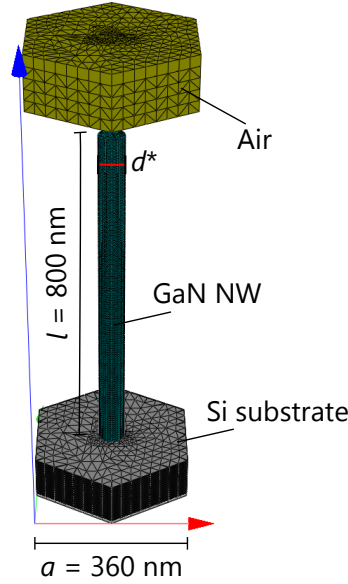


Figure 7.5: Model and simulation domain used to calculate the absorbance of GaN NW arrays with varying diameter d^* with the software package JCMWAVE. In the present case, the pitch is set to $a = 360$ nm, the length of the NW is $l = 800$ nm, and its diameter $d^* = 90$ nm. Apart from the underlying Si substrate, the NW is surrounded by air with $n = 1$, and periodic boundary conditions are employed to represent the ordered NW array.

(in 1D) given by Eqs. (7.3)–(7.5). A very good agreement between the numerical simulations and the exact solution is found. However, it should be noted that, in order to reach this accuracy (i. e., a relative error below 5%), a sufficiently high resolution of the underlying mesh is required for both simulation tools.[†]

7.3.2. Calculating the absorbance of ordered GaN NW arrays

We continue with simulating the absorption of light with $\lambda = 325$ nm in ordered GaN NW arrays grown on a Si substrate. For simplicity, the GaN NWs are represented by cylinders with diameter d^* , since the influence of the exact hexagonal symmetry on the optical modes within the NWs has been shown to be marginal.^[157] We neglect the thin (13 nm) AlN buffer layer below the NWs as well as the sputtered SiO_x-mask. A hexagonal unit cell with periodic boundary conditions is employed in order to represent the hexagonal arrangement of the GaN NW array [cf. Fig. 7.1]. An image of the simulation domain after the meshing is depicted in Fig. 7.5. The complex index of refraction at $\lambda = 325$ nm which was used for the simulation is $2.65 + 0.3i$ for GaN^[191] and $5.16 + 3.2i$ for Si.^[192]

In the following, the absorbance A denotes the total absorbance of the GaN NWs, while the transmittance T represents the total amount of light transmitted through the NW

[†]For the resolution of the mesh used here, each data point required about 20 min of computing time on an Intel Core i7 quad core computer.

7. Internal and external quantum efficiency of ordered arrays of GaN nanowires

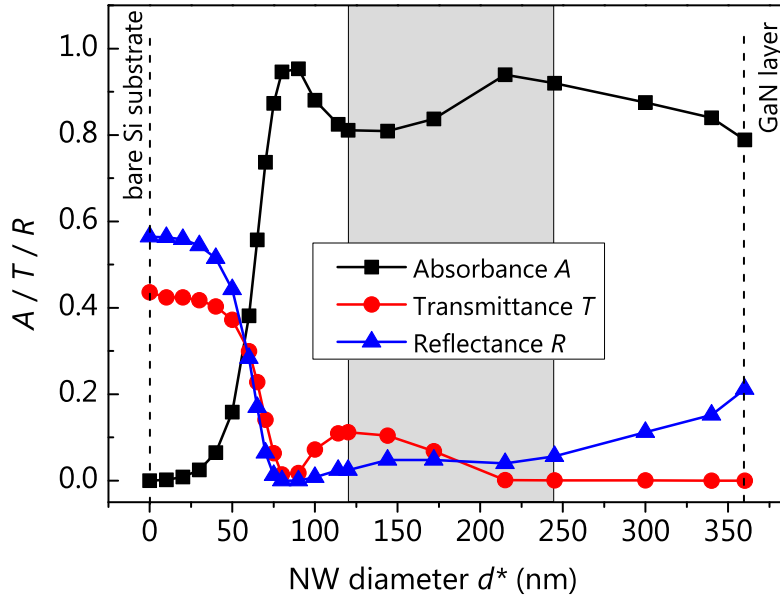


Figure 7.6: Absorbance A , transmittance T , and reflectance R of an ordered GaN NW array on a Si substrate as defined in the text for various NW diameters and an incident plane wave with $\lambda = 325$ nm. The length of the NWs is $l = 800$ nm and the pitch $a = 360$ nm. The grey shaded area depicts the NW diameter range of the experimentally investigated NW arrays. A NW diameter of zero represents a simulation without any NWs, i. e., a bare Si substrate, while $d = 360$ nm represents a compact GaN layer.

array, i. e., absorbed in the Si substrate. The reflectance R denotes the total reflectance of the ordered GaN NW array on the substrate. A monochromatic plane wave at normal incidence with $\lambda = 325$ nm, i. e., the same wavelength as the excitation laser in the PL and TRPL measurements, is chosen as the light source.

Figure 7.6 shows the result of the simulation for the ordered GaN NW array with $a = 360$ nm. The gray shaded area highlights the range of NW diameters investigated experimentally by PL spectroscopy [cf. Fig. 7.2]. Note that $d^* = 0$ represents a bare Si substrate without any GaN NWs, and $d^* = a$ represents a closed GaN layer. The values A , T , and R obtained for these two limiting cases are essentially identical to the values obtained analytically. For example, the absorbance and reflectance of the GaN layer at $\lambda = 325$ nm are found to be 0.8 and 0.2, respectively, as expected [cf. Fig. 7.4].

Let us now take a closer look at the absorbance A for different NW diameters d^* in Fig. 7.6. According to the simulation, very thin NWs with $d < 25$ nm absorb almost no light as their diameter is much smaller than the wavelength of the incident plane wave, which is in agreement with recent experiments^[193] and simulations for other material systems.^[194] A sharp onset of the absorbance is visible around $d^* = 50$ nm, while at the same time the transmittance T and reflectance R decrease. The peak value of $A = 0.97$ at $d^* \approx 90$ nm is significantly higher than the theoretical limit for the absorbance of light

7.3. Coupling of light into ordered arrays of GaN NWs and subsequent absorption

for this wavelength in a planar GaN layer. With increasing NW diameter, the absorbance slightly decreases to $A \approx 0.8$ and then exhibits a second resonance at $d^* = 220$ nm with $A = 0.94$. For $d^* > 220$ nm, it slowly approaches the bulk value of $A = 0.8$. The observed resonances in absorbance are called resonant leaky modes,^[195] and have been also observed for NWs in other material systems such as GaAs^[196] and InP.^[116,194] At these resonances, the incident light is coupled effectively into the NW, which consequently enhances the absorbance. From the simulation results presented in Fig. 7.6, it can be seen that a resonance in the absorbance naturally goes along with a minimum in reflectance R and transmittance T through the NW array into the Si substrate as $A + R + T = 1$ is conserved. More details on the mode-guiding properties of NWs are provided in Sec. 7.4.1.

The main result from this section is that the total amount of absorbed laser light by the ordered GaN NW arrays does not dramatically change within the NW diameter range investigated in the PL experiments in the previous sections, as highlighted by the gray, shaded area in Fig. 7.6. Consequently, the quenching of the integrated PL intensity with increasing NW diameter observed in Sec. 7.1 *cannot* be caused by the difference in absorbance for the different arrays as the latter increases by about 20%, while the former has been found to decrease by a factor of ten.

Dependence of the absorbance on the angle of illumination and the pitch

Up to this point, a plane wave at normal incidence was assumed as the light source in order to simulate the absorbance of the GaN NW array. However, in the PL experiment, the laser light is focused onto the GaN NW array with a microscope objective. The objective which was used for the PL measurements in Sec. 7.1 has a numerical aperture of 0.32, which corresponds to a maximum angle of 18.7° for the incident light with respect to the surface normal. We thus consider the influence of the angle of illumination onto the absorbance of the GaN NW array with $a = 360$ nm. The result is displayed in Fig. 7.7(a), and the difference in absorbance between an incident plane wave at 0° and 18.7° is found to be negligible.

In Sec. 7.1, a quenching of the PL intensity of ordered GaN NW arrays with increasing NW diameter was found for various values of the NW-to-NW distance a . The magnitude of this effect was found to depend strongly on the NW diameter d^* , but only weakly on a [cf. Fig. 7.2(b)]. Figure 7.7(b) depicts the absorbance of the three differently ordered GaN NW arrays with NW pitches of 360, 540, and 700 nm for NW diameters between 0 and 350 nm. As expected, the occurrence of the resonant leaky modes depends only on the NW diameter and not on the NW-to-NW distance a . The absorbance decreases slightly with increasing pitch a , as the incident light is more easily transmitted through the array and absorbed by the Si substrate. Again, the dependence of the absorbance from the NW diameter is in disagreement with the measured PL intensity of the arrays. For $a = 540$ nm, a factor of two increase in A is obtained between $d^* = 120$ and 200 nm, yet an order-of-magnitude decrease in PL intensity was found experimentally in this range

7. Internal and external quantum efficiency of ordered arrays of GaN nanowires

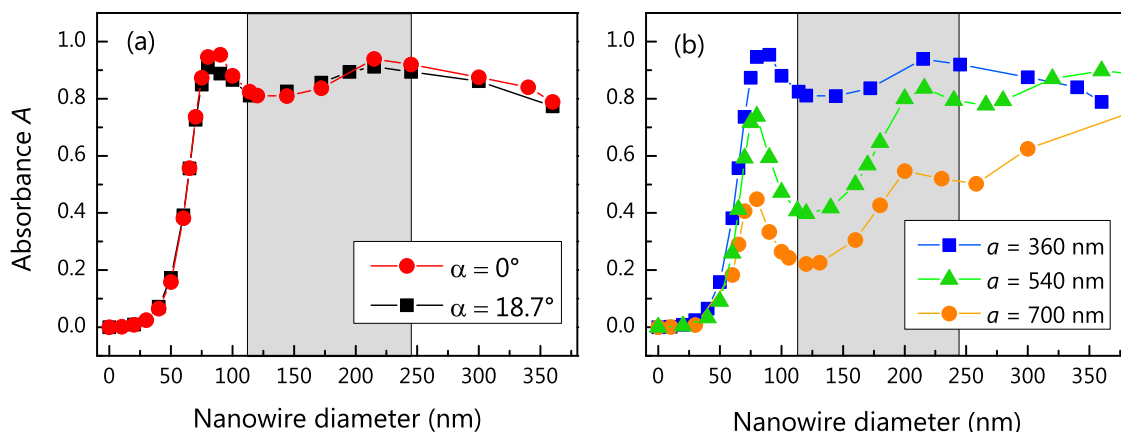


Figure 7.7: (a) Calculated absorbance of light with $\lambda = 325$ nm with two different angles of incidence for an ordered NW array with $a = 360$ nm and $l = 800$ nm. (b) Dependence of the absorbance of the NW array on the pitch a .

[cf. Fig. 7.2].

Nevertheless, we can use the results obtained for the absorbance of the different arrays to amend the measured values of the integrated PL intensity. Figure 7.8(a) shows the integrated PL intensity for 15 different ordered GaN NW arrays as obtained in the PL measurement vs the NW diameter. Figure 7.8(b) displays the data after taking into account the absorbance as obtained by the numerical simulation for the respective array. The dependence of the integrated PL intensity on the NW diameter persists, while the dependence on the NW-to-NW distance is reduced. Consequently, the cause of the decrease in PL intensity is believed to be due to a change of the extraction efficiency of the individual NWs with increasing diameter. This assumption is investigated by performing numerical simulations of the extraction efficiency of the PL signal for different NW diameters in the following section.

7.4. Extraction efficiency of GaN NWs

The dominant contribution to the luminescence of GaN NWs at 10 K is the spontaneous emission from donor- and acceptor-bound excitons at a wavelength of about 357 nm [cf. Fig. 7.2]. These spontaneous emitters can be considered to be distributed randomly in the GaN NW. The spontaneous emission is then either coupled to a guided mode and guided along the axis of the NWs or is leaking into free space. If the light is coupled to a guided mode, it can be either reflected or transmitted through the NW top facet, or guided into the underlying Si substrate and again be reflected or absorbed. Only light which is transmitted through the top facet or leaks into free space through the NW side walls and scattered at nearby NWs can potentially be collected by the microscope objective in a PL experiment.

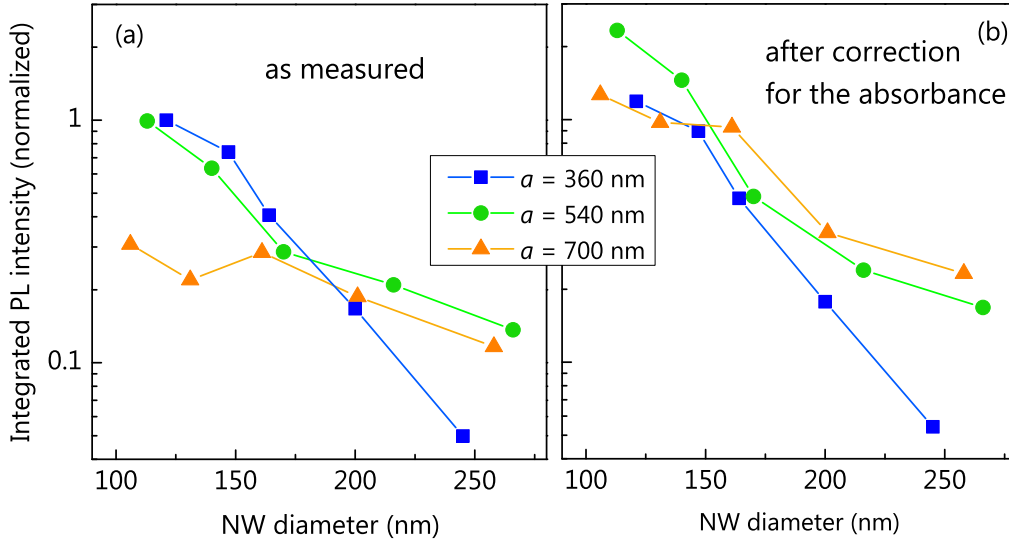


Figure 7.8: (a) Measured integrated low-temperature PL intensity under cw excitation for different ordered GaN NW arrays. The integrated intensity is normalized to the array with $a = 360$ nm and $d^* = 121$ nm. Note that the data is the same as shown in Fig. 7.2(b). (b) Integrated PL intensity after taking into account the differences in absorption of the laser of the respective arrays [cf. Fig. 7.7(b)].

To simulate the extraction efficiency of a GaN NW, we first use a single dipole emitting at $\lambda = 357$ nm to represent the spontaneous emitter. The simulation is performed using the FDTD software package LUMERICAL.[‡] Figure 7.9(a) displays the simulation domain used to calculate the extraction efficiency of a single dipole emitter placed inside a GaN NW. The hexagonal NW (green) has a diameter of $d^* = 120$ nm and stands on a Si substrate (red). In reality, the position of the emitter is distributed randomly inside the NW, but for simplicity we consider it to be placed in the center of the cross-section of the NW here. For each simulation run, the position of the dipole source is then changed along the vertical z -axis, and the extracted amount of light through the top facet is recorded by the denoted monitor in the x - y -plane. Additionally, a monitor plane is placed between the NW and the underlying Si substrate to calculate the power transmitted into the substrate. The simulation domain is surrounded by a three-dimensional box monitoring the total emitted power and perfectly matched layers (PML) in all dimensions. The dipole source emits a single pulse centered at $\lambda_z = 357$ nm, and, after all fields have vanished inside the simulation domain, the power transmitted through the various monitor planes is extracted. The extraction efficiency through the NW top facet and the absorbance of the Si substrate are calculated taking into account the total emitted power of the dipole, and the results are displayed in Fig. 7.9(b) for various positions of the dipole source along

[‡]In Sec. 7.3.1, we have shown that JCMWAVE and LUMERICAL yield identical results for the absorbance, reflectance, and transmittance of a GaN slab. As LUMERICAL more easily allows for the definitions of monitor planes for the transmitted power in arbitrary positions as well as a straight forward implementation for parameter sweeps, it was selected to simulate the extraction efficiency of the single NW here.

7. Internal and external quantum efficiency of ordered arrays of GaN nanowires

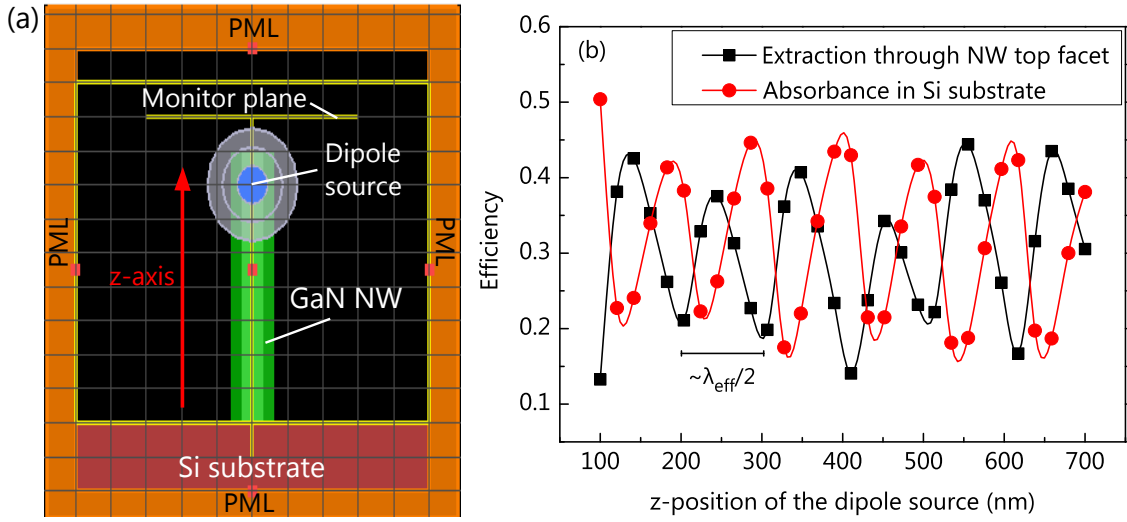


Figure 7.9: (a) Schematic diagram of the simulation domain for calculating the extraction efficiency of a single GaN NW using the software package LUMERICAL. The position of the dipole source is changed along the z -axis, and the extraction is monitored through the top facet. (b) Extraction efficiency of a dipole emitting at $\lambda = 357$ nm through the top facet of the NW as a function of the vertical position of the emitter ($z = 0$ represents the NW-substrate interface). The extraction efficiency is averaged over two polarization directions of the dipole, either perpendicular or parallel to the NW axis. The length of the NW is $l = 800$ nm and its diameter 120 nm.

the z -axis. Note that the values have been averaged for the two polarization directions of the dipole parallel and perpendicular to the NW axis as the experimentally determined PL intensity represents an overlap of transitions involving A and B excitons.

Evidently, both the extraction efficiency through the NW top facet and the absorption efficiency of the Si substrate strongly depend on the position of the dipole in z -direction. This finding provides direct evidence that some of the light emitted by the dipole is coupled to a guided mode of the NW, which is reflected both at the top and bottom facets forming a standing wave with $\lambda_{\text{eff}} = \lambda/2n_{\text{eff}}$. Here, $n_{\text{eff}} = 1.85$ is the effective refractive index of the respective guided mode. Note that a similar periodic dependence of the extraction efficiency of a single dipole emitter placed inside a NW on its vertical position has been found by other groups.^[168,197,198] Averaging over all positions along the z -axis, the extraction efficiency through the NW top facet is about 30%, while about the same amount is absorbed by the Si substrate for the present case. Consequently, 40% of the light leaks through the NW sidewalls and is absorbed by the PMLs. The total extraction efficiency η_{extr} of the GaN NW is thus 70%. Yet, it remains unclear how much of the light extracted through the side facets of the NW is scattered at neighboring NWs towards the microscope objective in the experiment.

In order to quantitatively include also the scattered light at neighboring NWs and collection efficiency of the microscope objective in the PL experiment, a complete simulation

of the NW array is required, including several NWs to act as scatterers. Furthermore, the simulations have to be performed for many different NW diameters and a random distribution of dipole positions. Last but not least, the far field has to be computed for all of these configurations in order to estimate the collection efficiency of a microscope objective with a finite acceptance angle. The simulation time for a 3D geometry with the required mesh accuracy is thus unpractically large. Consequently, most reports in the literature focus on studying the light extraction of single NWs by considering the various guided modes of the NW.^[155,167,168,197,198] We will thus follow this idea and continue with a calculation of the different guided modes in single GaN NWs with increasing diameter to obtain more insight into the mechanisms governing the extraction efficiency.

7.4.1. Guided modes in GaN NWs

Instead of considering single dipoles as the source of the luminescence signal when calculating the extraction, we will now specifically consider the GaN NWs as optical waveguides. First, we calculate the number of guided modes and their effective index of refraction n_{eff} .[§] Then we calculate the dispersion of these guided modes for GaN NWs with effective diameters d^* equal to those investigated in the PL experiment in Sec. 7.1. A mode is guided inside the NW when $n_{\text{eff}} > 1$, although a certain portion of the electric field of the mode will always leak into the surrounding air. The larger the effective refractive index for the mode, the stronger is the confinement inside the NW, i. e., the evanescent field outside the wire is reduced. Figure 7.10 shows the cross-sectional mode profiles of longitudinal guided modes in GaN NWs with diameters equal to those investigated experimentally in Secs. 7.1 and 7.2. Displayed is the cross-sectional electric field intensity profile $|E|^2$ from red (high intensity) to blue (low intensity).[¶] The calculation of the guided modes has been performed with the mode-solver package of LUMERICAL. Thicker GaN NWs are found to support a higher number of longitudinal guided modes, and, with increasing NW diameter, the confinement of the guided modes is increased.

Figure 7.11 displays the effective refractive index n_{eff} of these guided modes with increasing NW diameter, i. e., their dispersion relation. The bottom horizontal axis displays the dispersion for a size-normalized propagation constant given by the ratio of the NW radius $r = d^*/2$ and the frequency $\omega = 2\pi c/\lambda$, while the top horizontal axis relates the corresponding NW diameter d^* to a wavelength of $\lambda = 357$ nm. Note that the hybrid HE and EH modes are two-fold degenerate. The vertical lines indicate the average NW diameters of the ordered GaN NW arrays investigated experimentally in Secs. 7.1 and Sec. 7.2. In accordance with the qualitative impression obtained from Fig. 7.10, the guided modes exhibit a larger effective refractive index for thicker nanowires.

[§]Depending on the spatial extent of the mode, the effective refractive index lies in between the assumed values for GaN ($n = 2.65$) and air ($n = 1$).

[¶]TE stands for *transverse electrical*, i. e. the electric field is perpendicular to the propagation direction, while TM means *transverse magnetical*, thus the magnetic field is perpendicular to the propagation direction for TM modes.

7. Internal and external quantum efficiency of ordered arrays of GaN nanowires

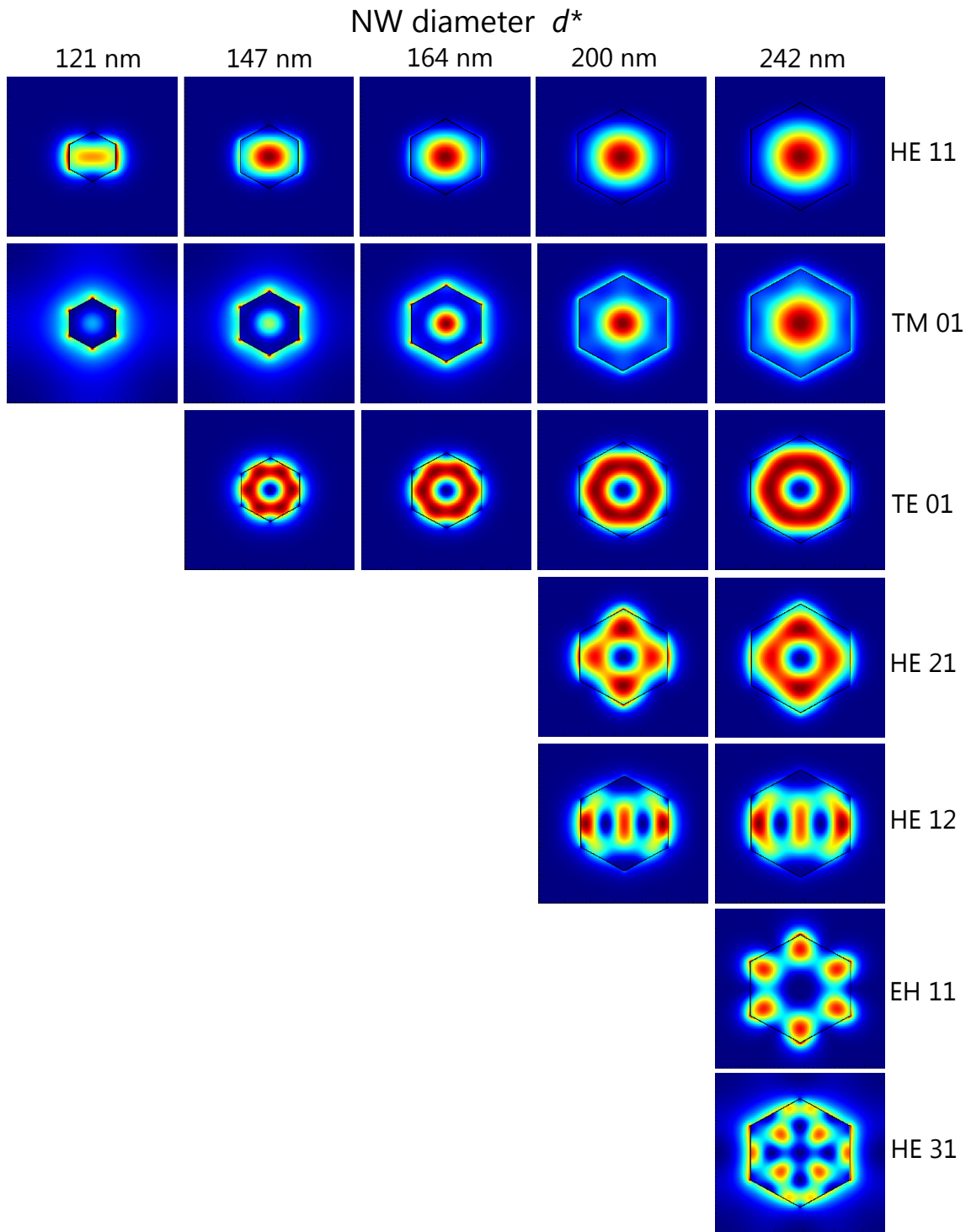


Figure 7.10: Overview of the longitudinal guided modes (i. e., exhibiting $n_{\text{eff}} > 1$) in GaN NWs with different diameters. Displayed is the intensity profile given by $|E|^2$, color-coded from red (high intensity) to blue (low intensity). Note that the hybrid HE modes are two-fold degenerate and only one polarization is shown.

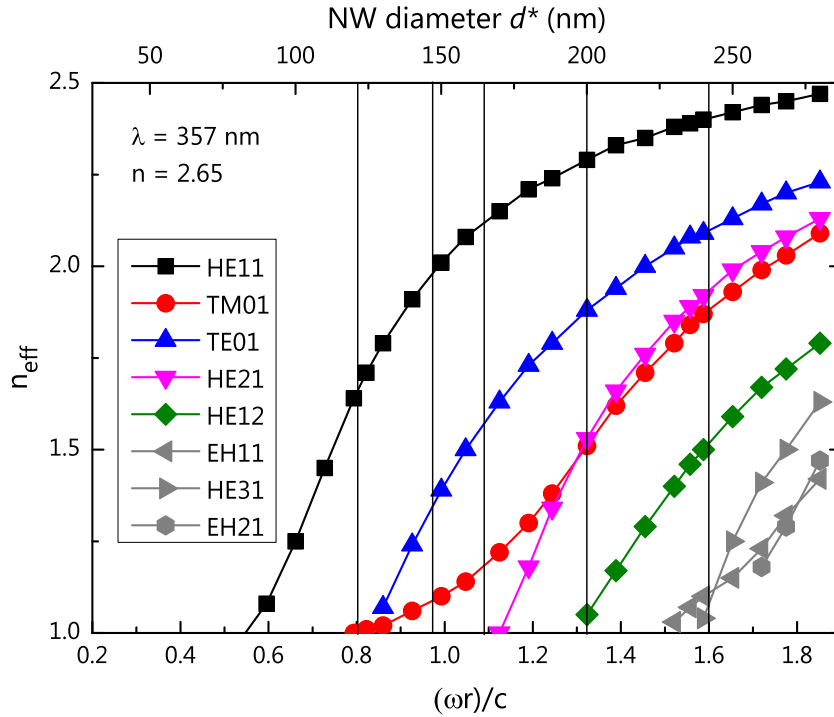


Figure 7.11: Dispersion of the guided modes at $\lambda = 357$ nm displayed in Fig. 7.10 for GaN NW with increasing NW diameter. The vertical lines indicate the diameters of the GaN NWs investigated experimentally in this present chapter.

Additionally, larger NWs support a higher number of guided modes. Both results are also in very good agreement with previously performed simulations on the waveguiding properties of NWs for different materials.^[155,157,167,168] Nanowires with $d^* \approx 120$ nm only support the fundamental HE11 mode and a very weakly guided TM01 mode ($n_{\text{eff}} \approx 1$), while the largest NWs with $d^* = 245$ nm support seven guided modes for emission at $\lambda = 357$ nm. All of these modes exhibit a larger effective refractive index and thus a better confinement within the GaN NW. The cut-off frequency of the individual modes agrees well with previous calculations,^[26] and a similar dispersion has been found for guided waves in NWs at longer wavelengths.^[167,198]

So far, we have only considered longitudinal guided modes in GaN NWs, but it has been shown that also whispering gallery modes (WGM) can be excited in NWs.^[157] A WGM travels along the cross section of the NW by multiple total internal reflection at the NW sidewalls and eventually escapes the NW through one of the sidewalls. The coupling to WGMs is particularly important when the source is a radial quantum well. Qualitatively, the dispersion of WGMs is then very similar to the longitudinal guided modes, i. e., several modes have a cutoff between $1 \leq \omega r/c \leq 2$.^[157] However, as we are interested in the extraction efficiency of light from along the NW axis, we do not further consider the coupling to WGMs here.

Extraction efficiency of guided modes in GaN NWs

A guided mode of the luminescence that travels towards the top facet of a GaN NW will either be reflected at the interface to air or transmitted into free space. If it is reflected, it will be guided towards the underlying Si substrate and again be reflected or absorbed by the Si substrate. We expect that a large portion of the light traveling inside the NW towards the Si substrate is lost due to efficient absorption. In a first approximation, the reflectance of the guided modes at the NW top facet depends on the contrast in refractive index. Thus, modes which are stronger confined exhibit a larger reflectance, which consequently reduces their extraction efficiency.^[167,168] Indeed, the reflectance at the NW top facet was found to increase substantially with increasing NW diameter for $1 \leq \omega r/c \leq 2$,^[157,197] which is exactly the diameter range we investigate in the PL experiment [cf. Fig. 7.11]. At to NW/air interface, a reflectance of up to 0.7 has been found for the TE₀₁ mode and up to 0.6 for the TM₀₁ mode in GaN NWs.^[155] At the same time, the reflectance of the guided modes at the NW bottom interface decreases, for example from 0.3 at $\omega R/c = 1.2$ to below 0.1 at $\omega R/c = 2.2$ for the TM₀₁ mode in a GaN NW on a sapphire substrate.^[155] For the specific case of single GaN NWs grown on Si, a decrease in the ratio of the reflectance at the NW/Si interface (bottom facet) to the reflectance at the NW/air interface (top facet) by a factor of ten for $1 \leq \omega r/c \leq 2$ has been predicted by simulations considering all guided modes in the NWs.^[197] this decrease is in good agreement with the experimentally observed quenching of the PL intensity in this diameter regime in Sec. 7.1.

In summary, we have found that both the number of guided modes for the photoluminescence as well as the effective refractive index of these modes increases considerably when the diameter of a GaN NW is increased from 120 to 245 nm, i. e., the range where a quenching of the measured PL intensity was found experimentally [cf. Sec. 7.2]. Consequently, NWs that support only one guided mode exhibit a larger overall extraction efficiency through the top facet. This extraction efficiency monotonically decreases with increasing NW diameter as more and stronger confined modes are supported by the NW geometry, whose reflectance at the top facet increases with the diameter. At the same time, a larger portion of the light is guided into the substrate and absorbed. This result is in agreement with the presented experimental data in Fig. 7.2. In general, the extraction efficiency depends strongly on the position of localized emitters due to the waveguiding properties of GaN NW in the investigated diameter range [cf. Fig. 7.9]. This becomes of particular importance when a quantum well at a specific position along the vertical axis is used as the source of the light.^[197]

Additionally, the collection efficiency η_{coll} has to be considered as the PL intensity in the experiment is collected by a microscope objective rather than an integrating Ulbricht sphere covering the full solid angle. The amount of light being collected by the objective with a certain numerical aperture depends on the far-field emission pattern of the GaN NWs which is investigated now.

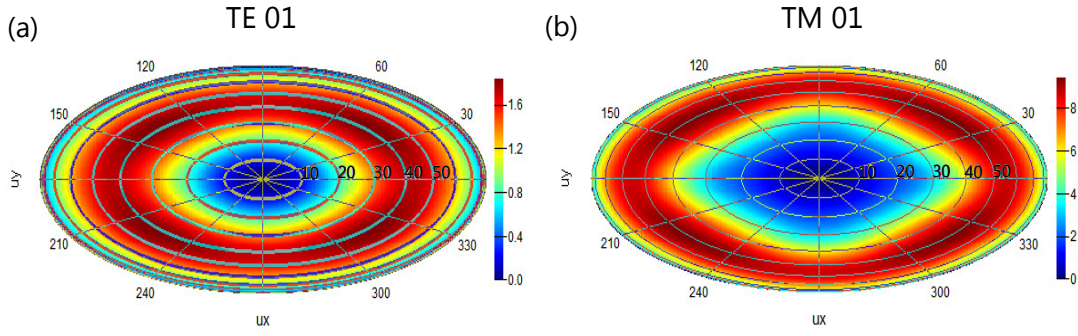


Figure 7.12: Far-field intensity profile of the (a) TE01 and (b) TM01 mode with $\lambda = 357$ nm extracted from a GaN NW with $d^* = 250$ nm at a distance $z \gg \lambda$. The color scale displays the intensity in arbitrary units.

Far-field emission pattern of guided modes

Once a guided mode has been transmitted into free space at the NW top facet, it develops a characteristic intensity distribution perpendicular to the propagation direction (the far-field pattern) at a distance $z \gg \lambda$. The far-field pattern is not directly equivalent to the respective intensity distribution of the electric field inside the NW. The software package LUMERICAL contains a specific function which calculates the far-field pattern at $z \gg \lambda$ from the near-field intensity distribution of a transmitted mode at the NW top facet.

Figure 7.12 displays the calculated far-field pattern for the TM01 and TE01 modes for a GaN NW with $d^* = 250$ nm. While the HE11 mode [not shown] always exhibits a maximum intensity at an angle of 0° with respect to the NW axis in the far field,^[156] the TE01 and TM01 modes exhibit a minimum at this point in space. The maximum intensity in the far field is emitted at an angle of 45° and 55° for the TE01 and TM01 mode, respectively. These values are in agreement with previous calculations^[156] and well beyond the acceptance angle of 18.7° of the objective used for the PL measurements. Consequently, the light which is coupled into those modes and extracted from the NW top facet cannot be collected. It has furthermore been predicted that the angle at which the maximum of the intensity is found increases with increasing NW diameter between $\omega R/c = 1$ and 2 for the TE01 and TM01 modes,^[156] which further increases the magnitude of the effect. In order to circumvent this effect and experimentally determine the total extraction efficiency, an Ulbricht sphere is required.

The complete far-field emission pattern of a NW is a superposition of the individual far-field pattern of all guided (and extracted) modes weighted by the power which is guided in the respective modes. Calculating exactly how much power is guided in each guided mode requires the consideration of a very large number of dipoles at random positions inside the NWs as the coupling probability to a guided mode depends strongly on the position and polarization of each dipole. For small NW-to-NW distances $a \approx \lambda$, the coupling of neighboring NWs can additionally influence the far field of the emission,

7. Internal and external quantum efficiency of ordered arrays of GaN nanowires

and hence a complete simulation is needed which is beyond the scope of this theses.

Experimentally, the far-field emission pattern of InP NW LED has recently been found to exhibit a minimum at 0° with respect to the NW axis, caused by the enhanced coupling of the emission to higher order guided modes in these NWs.^[27] Another way of accessing the directionality of NW emission is Fourier microscopy,^[199] and a severe influence of the NW geometry on the directionality of the emission has been determined for single InP NWs.^[200]

7.4.2. Comment: Ordered NW arrays as a photonic crystal

Due to its regular structure in two dimensions, an ordered GaN NW array may act as a photonic crystal for a specific optical wavelength.^[108] However, within the course of the present thesis, we did not find any evidence that the ordered GaN NW arrays exhibit a photonic bandgap at the investigated wavelengths. First of all, one would expect that the spontaneous emission rate is altered if the emission energy lies within a photonic bandgap. However, the experimentally determined PL transients at $\lambda = 357$ nm did not reveal any change in τ_{short} or τ_{long} with the NW diameter d^* [cf. Fig. 7.3] or pitch a . In accordance with that, the observed quenching of the low-temperature PL occurs for various values of the NW pitch [cf. Fig. 7.2]. Furthermore, the fundamental photonic bandgap of a TM mode for a two-dimensional photonic crystal is expected at $a \approx \lambda/2$,^[108] which would correspond to a lattice constant (NW-to-NW distance) of $a \approx 180$ nm for the wavelength of the low-temperature PL of GaN (if the NWs are surrounded by air with $n = 1$). This regime was not explored experimentally in this theses. Additionally, a photonic crystal requires a high degree of perfection of the involved structures. Although the ordered GaN NW arrays look very regular at first glance, the aberration from a perfectly ordered, homogeneous array of NWs cannot be disregarded [cf. Fig. 7.1] and hence may further obliterate any photonic crystal effects.

7.5. Summary

Upon investigating the low-temperature PL signal of ordered GaN NW arrays fabricated by SAG, an unexpected decrease of the integrated PL intensity with the NW diameter was observed. In order to unravel the origin of this effect, the external quantum efficiency of ordered GaN NW arrays was studied.

- Time-resolved PL measurements revealed a nearly constant internal quantum efficiency of the ordered GaN NW arrays for different NW diameters, in agreement with the results presented in Chap. 5.
- The absorption of the laser light in the different GaN NW arrays was simulated by finite-element simulations. The result is that the quenching of the PL intensity is not caused by a change in absorbance of the laser light for different arrays.

- The extraction efficiency for the spontaneous emission was studied for single GaN NWs. The GaN NWs act as waveguides for the luminescence from the mono-mode regime for the thinnest NWs to the multi-mode regime for the thickest NWs which have been investigated. At the same time, the reflectance of guided modes at the NW top facet increases as the effective refractive index of each mode increases with the NW diameter. Additionally, the transmittance of the spontaneous emission into the substrate is subsequently enhanced for larger NW diameters, which causes a large portion of the light being lost to absorption. Consequently, the overall extraction efficiency of GaN NWs decreases strongly within the investigated NW diameter range.
- Last but not least, the collection efficiency of the microscope objective is decreasing with increasing NW diameter as more modes are guided and extracted, whose far-field pattern exhibits a maximum in the intensity at angles beyond the acceptance angle of the employed objective.

In conclusion, the experimentally obtained decrease in the low-temperature PL intensity for ordered GaN NW arrays with increasing average diameters between 120 and 250 nm is successfully explained by a monotonous reduction in their external quantum efficiency as obtained by the combination of the results from various experiments and simulations within this chapter.

Conclusions and outlook

In this thesis, the dynamics of free and bound excitons in GaN NW ensembles with average diameters between 50 and 250 nm have been investigated by cw and time-resolved PL spectroscopy. Particular focus was given to the measurement of the PL transients of free and bound excitons in the low excitation regime over many orders of magnitude in intensity with high spectral resolution. In conjunction with simulations based on rate equation systems, the experimental results significantly improved our understanding of the exciton dynamics in GaN NWs and gave access to their internal quantum efficiency. Additionally, the different contributions to the external quantum efficiency of ordered GaN NW arrays were explored by a combination of PL experiments and numerical simulations of their light absorption and extraction. In the following section, the main conclusions drawn from each chapter are briefly summarized and linked. Finally, the results are put into a wider context, and an outlook for further investigations is presented.

Conclusions

- Based on their high structural perfection, it has been suggested that excitons in GaN NWs decay mainly radiatively at low temperatures. However, the data obtained within this thesis are not compatible with this hypothesis. The presented results conclusively show that the effective exciton lifetime in the examined GaN NW ensemble is limited by nonradiative recombination between temperatures of 10 and 300 K. Furthermore, bound and free excitons in the investigated GaN NWs are coupled even at nominally low temperatures, a fact which is reflected experimentally by their common effective lifetime. The nonradiative decay of bound excitons may thus take place via the free exciton state. The effective lifetime of the coupled system is found to be independent of the mean surface-to-volume ratio and coalescence degree of the NW ensemble. This implies that the nonradiative process is neither caused by surface recombination nor occurs at dislocations formed due to NW coalescence. The former observation is of particular interest for the community since the crystal surface at the NW sidewalls was generally assumed to provide the dominant channel for nonradiative recombination of excitons in GaN NWs, inde-

8. Conclusions and outlook

pendently of the NW diameter.

- We conclude that the nonradiative recombination of excitons in these GaN NWs occurs at point defects between 10 and 300 K. Given that the substrate temperatures used in the MBE growth of GaN NWs are low compared to those used in both metal-organic and hydride vapor phase epitaxy, the point defect density in these NWs is necessarily higher than in state-of-the-art GaN layers, which are grown closer to equilibrium. However, even for these latter samples, point defects were suggested to limit the lifetime of excitons when the density of structural defects is low,^[201] whereas they were found to dominate recombination in MBE-grown GaN layers regardless of the dislocation density.^[202] In the present case, the point defect density does not need to be excessively high in order to dominate the exciton decay. Given that the diffusion length of free excitons in GaN is larger than 50 nm,^[46-48] a density of nonradiative point defects as low as 10^{15} cm^{-3} may suffice to introduce an effective nonradiative decay channel for the donor-bound exciton state due to its coupling with the free exciton state.
- The combination of our experimental results with simulations based on a coupled rate equation model enabled us to interpret the frequently observed biexponential PL transient of the donor-bound exciton state in GaN NWs. While the fast component of the decay reflects the effective lifetime of the coupled $(D^0, X_A) \leftrightarrow X_A$ system, the slow component of the transient is induced by a repopulation of the (D^0, X_A) state due to the coupling with the acceptor-bound excitons which have a longer lifetime. By analyzing the underlying rate equation model, we were able to quantitatively investigate the strength of the coupling between the (D^0, X_A) and X_A states. At first glance, the strong coupling of these states is surprising given the 7 meV binding energy of the (D^0, X_A) complex and the low lattice temperature of 10 K. However, we obtained values of 27 to 37 K for the carrier temperature of the GaN NWs, despite the low excitation density used in these experiments. Detailed balance arguments predict that a carrier temperature of about 30 K is required to enable the strong coupling between the free and bound exciton state, a value which is in reasonable agreement with the experimentally obtained results. The origin of this unexpectedly high carrier temperature is presently unknown and should be investigated in the future as it ultimately represents the reason for the effective non-radiative decay of the (D^0, X_A) state. Note that an enhanced thermal dissociation of bound excitons due to a high carrier temperature in GaN NWs has also been suggested in Ref. 89.
- The detrimental effect of the nonradiative point defects is mediated by a strong coupling between the free and bound exciton states in these GaN NWs. This coupling effectively masks the intrinsic decay rate of the (D^0, X_A) state. Consequently, a correlation of this quantity with the growth conditions of the NWs, for example

the substrate temperature, is currently not possible. We are thus left with studying the effective lifetime of the coupled system which depends also on the dissociation rate of bound to free excitons.

- We have shown that the PL intensity of a GaN NW ensemble is not a meaningful quantity to determine the internal quantum efficiency, in contrast to a planar layer. The multiple contributions to the external quantum efficiency of ordered GaN NW arrays in PL were explored. This detailed understanding of the contributions is of importance for the optical investigation of NWs in general. We used time-resolved PL experiments to access the internal quantum efficiency and performed numerical simulations to calculate the absorbance and extraction efficiency of ordered GaN NW arrays. Experimentally, we found that the PL intensity of these samples depends critically on the NW diameter, in accordance with the results from the simulations. This diameter dependence originates from an enhanced coupling of the spontaneous recombination to guided modes inside the NW. However, the extraction efficiency of those modes through the NW top facet is reduced with increasing NW diameter, and the light is then guided towards the Si substrate and absorbed. In general, both the absorbance and extraction efficiency of NWs depends critically on the NW diameter within the investigated diameter range. A direct comparison of the PL intensity of samples with different diameters will thus lead to erroneous conclusions regarding the internal quantum efficiency of the samples.

In summary, for the low excitation density used in the present work, the internal quantum efficiency of the GaN NWs investigated is not larger than 20%, even at 10 K, due to the coupling of bound and free exciton states. The coupling of excitonic states is not limited to the specific case of GaN NWs, but should also apply to other material systems and sample geometries. As a matter of fact, signatures for the coupling of different exciton states at low temperatures have been observed experimentally in homoepitaxial GaN layers,^[59] but have been interpreted differently. For ZnO NWs, the interpretation of biexponential PL transients at low temperatures is currently under discussion.^[203–206] In a similar fashion, the insights obtained for the external quantum efficiency of ordered arrays of GaN NWs can be adapted to any semiconductor NW system interacting with light.^[196,207] However, the precise impact of the absorbance and extraction efficiency on a PL measurement depends critically on the NW dimensions, the excitation wavelength used, and the energy of the spontaneous emission in each case.

Outlook

The presented understanding of low-temperature exciton dynamics GaN NWs suggests that nonradiative point defects cause the rapid decay of excitons in the investigated GaN NWs. Here, we propose an approach to reduce the contribution of this nonradiative channel, and consequently enhance the internal quantum efficiency of GaN NWs. We also discuss a complementary approach to study the external quantum efficiency of GaN NWs based on a top-down approach. Finally, we briefly give an outlook on further fundamental investigations of carrier dynamics in the ternary alloy (In,Ga)N used in light-emitting diodes (LEDs) for solid-state lighting.

- The substrate temperature which minimizes the density of point defects corresponds to half the melting temperature of the material, based on theoretical grounds.^[208,209] In vapor-phase epitaxy, GaN is grown at about half its melting point (1000 – 1100 °C), whereas GaN NWs are grown in MBE with typical substrate temperatures of 780 to 830 °C, i. e., a temperature regime which is not optimal following the previous argument. However, increasing the substrate temperature is not straightforward in MBE because the maximum temperature, which is feasible for the growth of GaN, is limited by both the desorption of Ga adatoms and the decomposition of the material.^[132,210] Additionally, further experiments are necessary to unambiguously identify the type of point defect which contributes to the coupling between the (D^0, X_A) and X_A states. A first step would be to study the exciton dynamics in GaN NWs at precisely controlled lattice temperatures below 10 K. This temperature regime can be achieved by immersing the NW sample into liquid helium using a bath cryostat. It should be carefully investigated whether the enhanced carrier temperature is also present in planar GaN layers under the same experimental conditions or if the effect is limited to GaN NWs. If experimental conditions are found which cause the coupling to vanish, a significant increase of the (D^0, X_A) lifetime is expected. The intrinsic lifetime of the (D^0, X_A) state can then be studied further, for example by varying the growth conditions of the GaN NWs.
- The understanding of the external quantum efficiency of NWs, especially those configured in ordered arrays should be further improved. In addition to experiments employing the selective-area growth of GaN NWs on patterned substrates, a top-down approach could be used to achieve ordered arrays of nanostructures with controlled dimensions. This method could also provide new insights into the fundamentals of NW-light interactions, as a top-down approach ensures homogeneous material quality and flexibility in geometric design. Regardless of the approach used to fabricate the NWs, their arrangement and dimensions need to be optimized for each specific application, likely with the help of numerical simulations. It has already been shown in other material systems that an approach combining numerical simulations and optimized growth can result in highly effi-

cient NW-based devices. More specifically, an InP NW-based solar cell with 13.8% efficiency under controlled conditions was achieved,^[211] and, in some respect, this device outperforms its planar counterpart.

- Exciton dynamics in GaN are not only of fundamental interest, but may also present a first step towards understanding carrier dynamics in the ternary compound (In,Ga)N. Because this material is used as the active region in GaN-based LEDs, optimizing its internal quantum efficiency is of high technological relevance. However, the recombination of carriers in (In,Ga)N is far more complex than in GaN. The alloy fluctuations in the former material induce strong carrier localization on a microscopic scale and hence, in many aspects, cause a recombination behavior resembling amorphous semiconductors.^[212–214] While the carrier localization in (In,Ga)N/GaN heterostructures potentially enables the high internal quantum efficiency of light-emitting devices at room temperature,^[215] it introduces at the same time severe difficulties to understand the carrier dynamics on a fundamental level.^[216] In contrast to GaN, the carriers are spatially separated in (In,Ga)N due to a differing carrier localization of electrons and holes. Consequently, both the radiative and nonradiative recombination rates are governed by a combination of diffusion and tunneling of the carriers and are thus no longer time independent. Preliminary TRPL results revealed a complex shape of the PL transient in (In,Ga)N which impedes the extraction of an effective lifetime. Additional temperature-dependent TRPL measurements for various excitation densities are necessary to study the recombination behavior at carrier densities which are similar to those in LEDs. These experiments should be accompanied by Monte-Carlo simulations of the electron-hole kinetics in (In,Ga)N, which take into account both their radiative and non-radiative recombination by tunneling as well as their diffusion. In the end, it is envisioned that such a combination of experiments and simulations may provide new insights into the physical origin of the well-known efficiency droop in nitride-based LEDs.^[217] The dominant mechanism of this efficiency droop is still under discussion,^[218–221] and its identification is of utmost importance for the further improvement of nitride-based light emitters.

Diameter distribution and coalescence degree of nanowire ensembles

In this thesis, correlations between optical properties, such as the effective decay time of free and bound excitons, and structural parameters, such as the perimeter-over-area ratio of GaN NW ensembles, are investigated. Therefore, an accurate and reliable method to determine the diameter distribution and coalescence degree of as-grown NW ensembles is required and described in this appendix. Although we will exclusively report on the investigation of GaN NW ensembles, the presented methods can be applied to nanowires and nanostructures of any material system.

Scanning electron microscopy and image processing using ImageJ

The GaN NWs studied here have a typical diameter of 30 to 250 nm and a length of 500 nm to 5 μm . A technique capable of resolving the shape of nanostructures with these dimensions is scanning electron microscopy (SEM). Figure A.1(a) depicts the top-view scanning electron micrograph of sample R, a typical, spontaneously formed GaN NW ensemble. The NW cross sections clearly exhibit a wide variety of different shapes. While some have an almost regular hexagonal top facet (emphasized by the green arrows), many NWs have branched, kinked, and elongated top facets, i. e., shapes which are very different from a regular hexagon (red arrows). Spontaneously formed GaN NWs form a wurtzite crystal along the polar $\langle 0001 \rangle$ axis on Si(111) substrates.^[129,131] Thus, their top facet is expected to be a regular hexagon. However, if a NW coalesces with an adjacent wire during growth, the shape of the NW top facet is altered. As it has been shown in a recent publication, the degree of coalescence in spontaneously grown GaN NW ensemble can be determined by performing a statistical analysis of the NW top facets shapes.^[178]

A. Diameter distribution and coalescence degree of nanowire ensembles

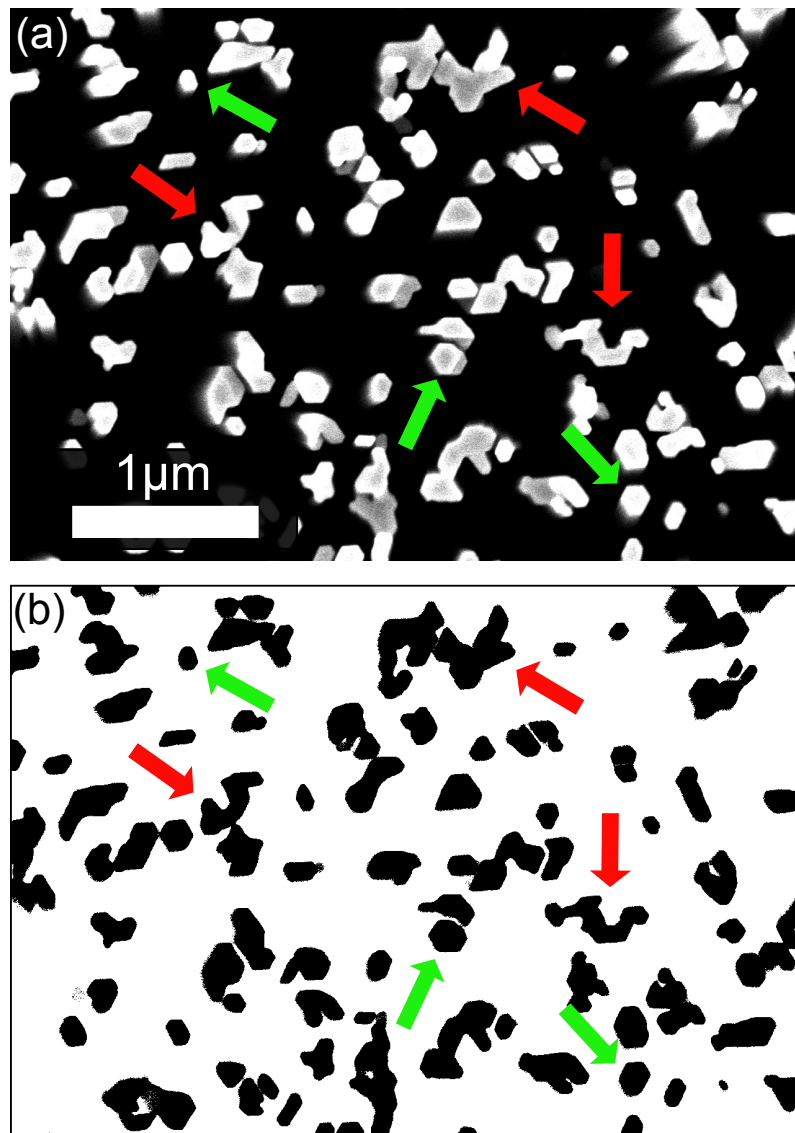


Figure A.1: (a) Contrast-enhanced, cross-sectional scanning electron micrograph of the spontaneously formed GaN NW sample R. The image has been taken by A.-K. Bluhm. (b) After applying a threshold, the image can be used to quantitatively analyze the NW top facets using IMAGEJ.^[222] The colored arrows indicate two different classes of objects in the images, one having a nearly hexagonal top facet (green arrows), the other containing top facets with irregular shapes (red arrows).

Secondary electron micrographs in combination with the scientific image-analysis software IMAGEJ^[222] are employed to extract quantitative information of the NW cross sections. The software analyzes the shape and size of particles in pixel graphics such as the NW cross sections in Fig. A.1(a). Before the 'analyze particles' algorithm of IMAGEJ is executed, the micrographs are despeckled, and their contrast is enhanced. The resulting image after these two steps is displayed in Fig. A.1(b). In general, the scanning electron

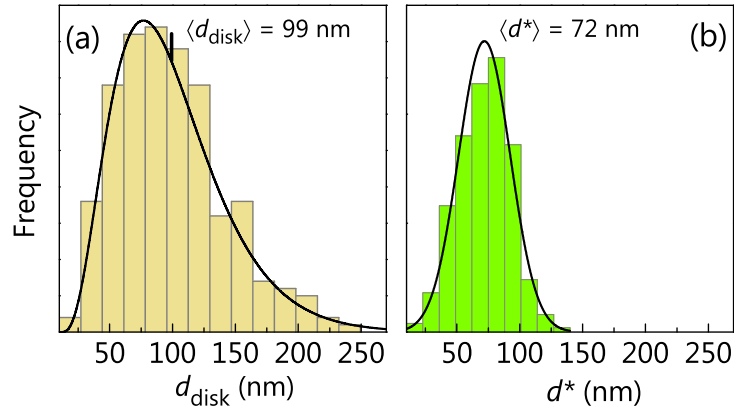


Figure A.2: (a) Histogram representing the distribution of equivalent disk diameters d_{disk} in the GaN NW ensemble as obtained from measuring the area A of the NW top facets. Applying a fit with a shifted Gamma distribution to the data yields a mean of $\langle d_{\text{disk}} \rangle = 99$ nm. (b) Histogram showing the distribution of the parameter d^* for the same NWs as in (a). This distribution is well represented by a Gaussian distribution with a mean of $\langle d^* \rangle = 72$ nm. The data was analyzed by O. Brandt.

micrographs need to have a sufficiently high resolution as the error of a length measurement is at best ± 1 pixel. At the same time, the number of analyzed NWs should be as high as possible to yield a good statistic of the results. In order to fulfill both criteria, it is often desired to analyze many micrographs from the same sample, taken at closely spaced positions on the wafer. The 'analyze particles' algorithm of IMAGEJ then returns a list of properties for each NW cross section, including its area A , and perimeter P .

Equivalent-disk diameter and perimeter-over-area ratio of nanowires

The equivalent disk diameter $d_{\text{disk}} = 2\sqrt{A/\pi}$ for each NW follows directly from the area A . The resulting distribution of d_{disk} for sample R is presented in the histogram in Fig. A.2(a) and is seen to be strongly asymmetric towards larger diameters. This observation is a direct indication that coalescence plays an important role in this sample.^[178] Coalesced aggregates of NWs tend to form elongated and branched shapes exhibiting larger areas [cf. Fig. A.1] than uncoalesced NWs. As the calculation of d_{disk} is based only on the area of the top facet of a NW or aggregate, its distribution is shifted towards larger values of d_{disk} compared to uncoalesced NWs. The data can be fitted with a shifted Gamma distribution to extract the mean equivalent disk diameter $\langle d_{\text{disk}} \rangle = 99$ nm.^[178]

In this thesis, the influence of the NW surface on the recombination dynamics of bound and free excitons is studied. Assuming a finite surface recombination velocity S , the

A. Diameter distribution and coalescence degree of nanowire ensembles

surface recombination rate γ_S in NWs can be approximated by the relation

$$\gamma_S = \frac{4S}{d_{\text{disk}}}, \quad (\text{A.1})$$

which is strictly valid for cylindrical objects with diameter $d = d_{\text{disk}}$. However, as discussed above, the inadvertent coalescence of individual NWs distorts their shape towards elongated and branched shapes. Hence, the equivalent-disk diameter $\langle d_{\text{disk}} \rangle$ systematically underestimates the influence of the surface for NW ensembles with a high coalescence degree. However, it is possible to generalize Eq. (A.1) for an arbitrarily shaped object. In general, the surface recombination rate γ_S is proportional to the perimeter-over-area ratio:^[164]

$$\gamma_S = \frac{SP}{A} = \frac{4S}{d^*}. \quad (\text{A.2})$$

with $d^* = 4A/P$, where A is the cross-sectional area of a NW and P is the perimeter of its cross section. The parameter d^* represent a new effective diameter of coalesced NWs compared to uncoalesced ones when both exhibit the same cross-sectional area A . Figure A.2(b) displays the distribution of d^* for sample R, which is symmetric in contrast to the distribution of equivalent disk diameters. Applying a Gaussian distribution to the data yields $\langle d^* \rangle = 72$ nm. This value is 20% smaller than the average equivalent disk diameter $\langle d_{\text{disk}} \rangle = 99$ nm, underlining the importance of considering the perimeter-over-area ratio of the NWs when investigating surface-related phenomena.

Coalescence degree of spontaneously grown GaN nanowire ensembles

It is possible to distinguish between coalesced and uncoalesced NWs by investigating the circularity C of the NW cross-sections as described in a recent study.^[178] The circularity is defined by $C = 4\pi A/P^2$ for an arbitrarily shaped, contractible two-dimensional shape (i. e., one without any "holes") with area A and perimeter P . For a circle, the circularity is by definition $C = 1$, while a perfect hexagon has a slightly lower value of $C = 0.907$. The stronger the deviation from these regular shapes is, i. e., the larger the perimeter-over-area ratio, the smaller becomes C . Figure A.3(a) displays a histogram of the circularity of the NW cross sections from sample R. The distribution is rather continuous with a peak around $C = 0.8$. In order to distinguish between coalesced and uncoalesced NWs, we employ a threshold $\zeta_A = 0.762$ for the circularity based on the value of C for potential cross-sectional shapes of uncoalesced NWs derived in Ref. 178. Once this threshold is applied to the histogram [cf. dashed line in Fig. A.3(a)], calculating the coalescence degree

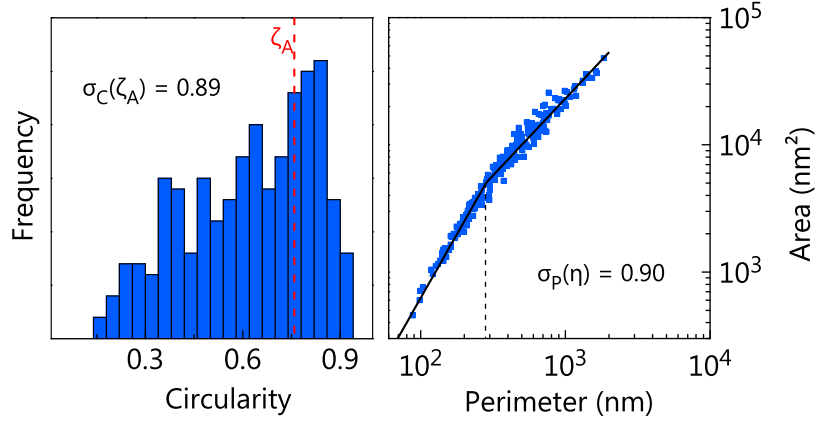


Figure A.3: (a) Histogram showing the circularity C of the top facets of 265 randomly selected NWs of sample R. Employing a threshold for the circularity of $\zeta_A = 0.762$ (vertical, dashed line) in order to distinguish between uncoalesced NWs and coalesced aggregates allows for the determination of the coalescence degree of the sample to $\sigma_C(\zeta_A) = 0.89$. (b) Area–perimeter plot of the same data. The solid line shows a fit to Eq. (6) from Ref. 178, yielding a coalescence degree of $\sigma_p(\eta) = 0.90$. The data was analyzed by O. Brandt.

σ_C of the GaN NW ensemble is straightforward:^[178]

$$\sigma_C(\zeta_A) = \frac{A_{C < \zeta_A}}{A_T} = 0.89. \quad (\text{A.3})$$

Here, $A_{C < \zeta_A}$ represents the sum of all top facet areas with $C < \zeta_A$ and A_T denotes the total area of all NW top facets. As the length of the GaN NWs is very homogeneous and much larger than their diameter, σ_C directly represents the ratio of coalesced to the total GaN volume in the sample. Thus, for the present sample, 89% of the GaN volume belong to NWs which have participated in at least one coalescence event during growth.

A second method to determine the coalescence degree based on the area–perimeter plot displayed in Fig. A.3(b) can be employed. The slope of the data changes abruptly from quadratic to linear at a certain critical perimeter η [cf. dashed line in Fig. A.3(b)]. The coalescence degree is then calculated by^[178]

$$\sigma_C(\eta) = \frac{A_{P > \eta}}{A_T} = 0.90. \quad (\text{A.4})$$

where $A_{P > \eta}$ denotes the sum over all objects with perimeter larger than η . The value of η is found by fitting Eq. (6) from Ref. 178 to the area–perimeter plot [Fig. A.3(b)]. The obtained values for the coalescence of sample R are in good agreement. However,

A. Diameter distribution and coalescence degree of nanowire ensembles

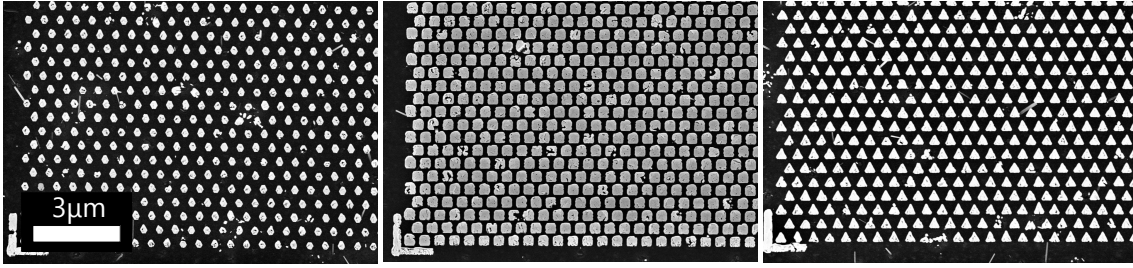


Figure A.4: Cross-sectional secondary electron micrographs of different GaN NW arrays grown by selective-area growth. The shape of the NW top facets reproduces the shape of the prepared holes in the SiO_x -mask. The latter one is shaped like a hexagon, a square, and a triangle (from left to right) in the design of the mask. The images have been taken by A.-K. Bluhm.

the values for the coalescence degree of GaN NW ensembles presented in this thesis are calculated employing the former method, i. e., the circularity of the NW top facets, as this method proved to be more accurate for samples with a low degree of coalescence.^[178]

The coalescence degree of nanowires grown by selective-area epitaxy

The analysis of the cross-sectional shapes of NWs described in the previous section can not be readily transferred to GaN NWs grown by selective-area growth. Figure A.4 displays the cross-sectional scanning electron micrographs of GaN NWs grown by SAG using differently shaped holes in the SiO_x -mask. Due to the small GaN nuclei (≈ 6 nm) compared to the large openings of the holes (50 – 200 nm), multiple NW nucleations per hole are inevitable.^[127,143] Consequently, coalescence of many neighboring NWs per hole occurs during growth and the shape of the final NW top facet mimics the shape of the original hole in the mask [cf. Fig. A.4]. Evidently, since almost arbitrarily shaped NW top facets can be achieved, the circularity C is no longer a meaningful quantity to characterize those NWs. The inverse of the perimeter-over-area ratio is very similar to the equivalent disk diameter ($d_{\text{disk}} \approx d^*$) of these NWs, as the top facet is mainly hexagonal for the investigated SAG GaN NWs samples. Hence, we can not employ the described methods to quantify the coalescence degree of GaN NWs grown by SAG, but rather set their coalescence degree to $\sigma_C = 1$. This approach is justified by the inevitable coalescence of wires in every hole under this specific growth mode.^[127,143]

List of samples

sample name	investigated in chapter	sample number	growth-mode	substrate temperature	III/V ratio	MBE operator
'D'	5	M1122	spontaneous	815 °C	0.44	S. Fernández-Garrido
'B'	5	M8857	spontaneous	800 °C	0.16	V. Consonni
'A'	5	M8891	spontaneous	780 °C	0.16	V. Consonni
'III'	5, 6	M81177	spontaneous	820 °C	0.23	T. Gotschke
	5	M81181	spontaneous	815 °C	0.23	T. Gotschke
	5	M81190	spontaneous	815 °C	0.23	T. Gotschke
	5	M81191	spontaneous	815 °C	0.38	T. Gotschke
	5	M9257	spontaneous	820 °C	0.83	P. Dogan
'R'	4	M9959	spontaneous	875 °C	2.3	J. K. Zettler
	3, 5, 6, A	M9960	spontaneous	835 °C	0.5	J. K. Zettler
'I' and II'	3, 5–7, A	M81224	SAG	825 °C	0.23	T. Gotschke
	4	M81228	SAG	825 °C	0.23	T. Gotschke

Table B.1: List of samples investigated in this thesis. All samples are GaN NWs grown on Si(111) substrates.

Bibliography

- [1] B. I. Shklovskii and A. L. Efros, *Electronic properties of doped semiconductors*, volume 45 of *Solid-State Sciences*, Springer Verlag Berlin Heidelberg, Berlin, Germany (1984).
- [2] H. P. Maruska and J. J. Tietjen, The preparation and properties of vapor-deposited single-crystalline GaN, *Appl. Phys. Lett.* **15**, 327 (1969).
- [3] C. J. Humphreys, Solid-State Lighting, *MRS Bull.* **33**, 459–470 (2008).
- [4] S. Pimputkar, J. S. Speck, S. P. DenBaars, and S. Nakamura, Prospects for LED lighting, *Nat. Photonics* **3**, 180–182 (2009).
- [5] The 2014 Nobel Prize in Physics - Press Release, Nobel Media AB 2014, http://www.nobelprize.org/nobel_prizes/physics/laureates/2014/press.html (2014).
- [6] S. E. Bennett, Dislocations and their reduction in GaN, *Mater. Sci. Technol.* **26**, 1017–1028 (2010).
- [7] C. M. Lieber, Semiconductor nanowires: A platform for nanoscience and nanotechnology., *MRS Bull.* **36**, 1052–1063 (2011).
- [8] W. Lu and C. M. Lieber, Semiconductor nanowires, *J. Phys. D. Appl. Phys.* **39**, R387–R406 (2006).
- [9] N. P. Dasgupta, J. Sun, C. Liu, S. Brittman, S. C. Andrews, J. Lim, H. Gao, R. Yan, and P. Yang, 25th anniversary article: semiconductor nanowires—synthesis, characterization, and applications., *Adv. Mater.* **26**, 2137–2184 (2014).
- [10] V. Mourik, K. Zuo, S. M. Frolov, S. R. Plissard, E. P. A. M. Bakkers, and L. P. Kouwenhoven, Signatures of Majorana fermions in hybrid superconductor-semiconductor nanowire devices., *Science* **336**, 1003–1007 (2012).

Bibliography

- [11] R. Yan, D. Gargas, and P. Yang, Nanowire photonics, *Nat. Photonics* **3**, 569–576 (2009).
- [12] A. Waag, X. Wang, S. Fündling, J. Ledig, M. Erenburg, R. Neumann, M. Al Suleiman, S. Merzsch, J. Wei, S. Li, H. H. Wehmann, W. Bergbauer, M. Straßburg, A. Trampert, U. Jahn, and H. Riechert, The nanorod approach: GaN NanoLEDs for solid state lighting, *Phys. Status Solidi* **8**, 2296–2301 (2011).
- [13] M. E. Coltrin, A. M. Armstrong, I. Brener, W. W. Chow, M. H. Crawford, A. J. Fischer, D. F. Kelley, D. D. Koleske, L. J. Lauhon, J. E. Martin, M. Nyman, E. F. Schubert, L. E. Shea-Rohwer, G. Subramania, J. Y. Tsao, G. T. Wang, J. J. Wierer, and J. B. Wright, Energy Frontier Research Center for Solid-State Lighting Science: Exploring New Materials Architectures and Light Emission Phenomena, *J. Phys. Chem. C* **118**, 13330–13345 (2014).
- [14] A. Kikuchi, M. Kawai, M. Tada, and K. Kishino, InGaN/GaN Multiple Quantum Disk Nanocolumn Light-Emitting Diodes Grown on (111) Si Substrate, *Jpn. J. Appl. Phys.* **43**, L1524–L1526 (2004).
- [15] H. Sekiguchi, K. Kato, J. Tanaka, A. Kikuchi, and K. Kishino, Ultraviolet GaN-based nanocolumn light-emitting diodes grown on n-(111) Si substrates by rf-plasma-assisted molecular beam epitaxy, *Phys. stat. sol. (a)* **205**, 1067–1069 (2008).
- [16] F. González-Posada, R. Songmuang, M. Den Hertog, and E. Monroy, Room-Temperature Photodetection Dynamics of Single GaN Nanowires, *Nano Lett.* **12**, 172–176 (2012).
- [17] M. Beeler, P. Hille, J. Schörmann, J. Teubert, M. de la Mata, J. Arbiol, M. Eickhoff, and E. Monroy, Intraband absorption in self-assembled Ge-doped GaN/AlN nanowire heterostructures., *Nano Lett.* **14**, 1665–1673 (2014).
- [18] M. D. Brubaker, P. T. Blanchard, J. B. Schlager, A. W. Sanders, A. Roshko, S. M. Duff, J. M. Gray, V. M. Bright, N. A. Sanford, and K. A. Bertness, On-chip optical interconnects made with gallium nitride nanowires., *Nano Lett.* **13**, 374–377 (2013).
- [19] M. J. Holmes, K. Choi, S. Kako, M. Arita, and Y. Arakawa, Room-temperature triggered single photon emission from a III-nitride site-controlled nanowire quantum dot., *Nano Lett.* **14**, 982–986 (2014).
- [20] R. K. Ahrenkiel, Minority-carrier lifetime in iii-v semiconductors, In *Minority Carriers in III-V Semiconductors: Physics and Applications*, volume 39 of *Semiconductors and Semimetals*, page 39, Academic Press, Inc., San Diego, CA, USA (1993).
- [21] B. Monemar, P. P. Paskov, J. P. Bergman, A. A. Toropov, T. V. Shubina, T. Malinuskas, and A. Usui, Recombination of free and bound excitons in GaN, *Phys. Status Solidi B* **245**, 1723–1740 (2008).

- [22] B. Monemar, P. P. Paskov, J. P. Bergman, G. Pozina, A. A. Toropov, T. V. Shubina, T. Malinauskas, and A. Usui, Transient photoluminescence of shallow donor bound excitons in GaN, *Phys. Rev. B* **82**, 235202 (2010).
- [23] R. Dingle, D. Sell, S. Stokowski, P. Dean, and R. Zetterstrom, Absorption, Reflectance, and Luminescence of GaN Single Crystals, *Phys. Rev. B* **3**, 497–500 (1971).
- [24] P. J. Pauzauskie and P. Yang, Nanowire photonics, *Mater. Today* **9**, 36 (2006).
- [25] J. C. Johnson, H.-J. Choi, K. P. Knutsen, R. D. Schaller, P. Yang, and R. J. Saykally, Single gallium nitride nanowire lasers., *Nat. Mater.* **1**, 106–110 (2002).
- [26] A. V. Maslov, M. I. Bakunov, and C. Z. Ning, Distribution of optical emission between guided modes and free space in a semiconductor nanowire, *J. Appl. Phys.* **99**, 024314 (2006).
- [27] J. Motohisa, Y. Kohashi, and S. Maeda, Far-field emission patterns of nanowire light-emitting diodes, *Nano Lett.* **14**, 3653–3660 (2014).
- [28] C. Kittel, *Introduction to solid state physics (dt.)*, R. Oldenbourg Verlag GmbH München, Munich, Germany, 8th edition (1989).
- [29] H. Morkoç, *Handbook of Nitride Semiconductors and Devices - Volume 1: Materials Properties, Physics and Growth*, volume 1, Wiley-VCH, Weinheim, Germany (2008).
- [30] H. Morkoç, *Handbook of Nitride Semiconductors and Devices - Volume 2: Electronic and Optical Processes in Nitrides*, volume 2, Wiley-VCH, Weinheim, Germany (2008).
- [31] R. S. Knox, *Theory of excitons*, volume 5, Academic Press Inc., New York, USA (1963).
- [32] I. Pelant and J. Valenta, *Luminescence spectroscopy of semiconductors*, Oxford University Press, Oxford, UK (2012).
- [33] B. Monemar, Fundamental energy gap of GaN from photoluminescence excitation spectra, *Phys. Rev. B* **10**, 676–681 (1974).
- [34] J. J. Hopfield, Fine structure in the optical absorption edge of anisotropic crystals, *J. Phys. Chem. Solids* **15**, 97–107 (1960).
- [35] K. P. Korona, A. Wyszomółek, K. Pakuła, R. Stępniewski, J. M. Baranowski, I. Grzegory, B. Łuczniak, M. Wróblewski, and S. Porowski, Exciton region reflectance of homoepitaxial GaN layers, *Appl. Phys. Lett.* **69**, 788 (1996).
- [36] Wikipedia.com (image has been released to the public domain), http://commons.wikimedia.org/wiki/File:Wurtzite_polyhedra.png (2014).

Bibliography

- [37] H. Morkoç, Comprehensive characterization of hydride VPE grown GaN layers and templates, *Mater. Sci. Eng. R* **33**, 135–207 (2001).
- [38] J. Lähnemann, U. Jahn, O. Brandt, T. Flissikowski, P. Dogan, and H. T. Grahn, Luminescence associated with stacking faults in GaN, *J. Phys. D. Appl. Phys.* **47**, 423001 (2014).
- [39] Y. T. Rebane, Y. G. Shreter, and M. Albrecht, Stacking Faults as Quantum Wells for Excitons in Wurtzite GaN, *Phys. status solidi* **164**, 141–144 (1997).
- [40] V. Consonni, M. Knelangen, U. Jahn, A. Trampert, L. Geelhaar, and H. Riechert, Effects of nanowire coalescence on their structural and optical properties on a local scale, *Appl. Phys. Lett.* **95**, 241910 (2009).
- [41] J. Frenkel, On the Transformation of light into Heat in Solids. I, *Phys. Rev.* **37**, 17–44 (1931).
- [42] J. Frenkel, On the Transformation of Light into Heat in Solids. II, *Phys. Rev.* **37**, 1276–1294 (1931).
- [43] R. E. Peierls, Zur Theorie der Absorptionsspektren fester Körper, *Ann. Phys. (Berlin)* **13**, 905 (1932).
- [44] G. Wannier, The Structure of Electronic Excitation Levels in Insulating Crystals, *Phys. Rev.* **52**, 191–197 (1937).
- [45] E. Hanamura, Rapid radiative decay and enhanced optical nonlinearity of excitons in a quantum well, *Phys. Rev. B* **38**, 1228–1234 (1988).
- [46] J. Speck and S. Rosner, The role of threading dislocations in the physical properties of GaN and its alloys, *Physica B* **273–274**, 24–32 (1999).
- [47] N. Ino and N. Yamamoto, Low temperature diffusion length of excitons in gallium nitride measured by cathodoluminescence technique, *Appl. Phys. Lett.* **93**, 232103 (2008).
- [48] G. Noguez, T. Auzelle, M. Den Hertog, B. Gayral, and B. Daudin, Cathodoluminescence of stacking fault bound excitons for local probing of the exciton diffusion length in single GaN nanowires, *Appl. Phys. Lett.* **104**, 102102 (2014).
- [49] J. Pedrós, Y. Takagaki, T. Ive, M. Ramsteiner, O. Brandt, U. Jahn, K. H. Ploog, and F. Calle, Exciton impact-ionization dynamics modulated by surface acoustic waves in GaN, *Phys. Rev. B* **75**, 115305 (2007).
- [50] K. Kornitzer, T. Ebner, K. Thonke, R. Sauer, C. Kirchner, V. Schwegler, M. Kamp, M. Leszczynski, I. Grzegory, and S. Porowski, Photoluminescence and reflectance

- spectroscopy of excitonic transitions in high-quality homoepitaxial GaN films, *Phys. Rev. B* **60**, 1471–1473 (1999).
- [51] A. Rodina, M. Dietrich, A. Göldner, L. Eckey, A. Hoffmann, A. Efros, M. Rosen, and B. Meyer, Free excitons in wurtzite GaN, *Phys. Rev. B* **64**, 115204 (2001).
- [52] J. J. Hopfield, Theory of the Contribution of Excitons to the Complex Dielectric Constant of Crystals, *Phys. Rev.* **112**, 1555–1567 (1958).
- [53] P. M. Corfdir, *Physics of the Ultrafast Dynamics of Excitons in GaN Nanostructures*, PhD thesis, École Polytechnique Fédérale de Lausanne (2011).
- [54] L. Andreani and F. Bassani, Exchange interaction and polariton effects in quantum-well excitons, *Phys. Rev. B* **41**, 7536–7544 (1990).
- [55] D. Kovalev, B. Averboukh, D. Volm, B. Meyer, H. Amano, and I. Akasaki, Free exciton emission in GaN, *Phys. Rev. B* **54**, 2518–2522 (1996).
- [56] A. Viswanath, J. Lee, D. Kim, C. Lee, and J. Leem, Exciton-phonon interactions, exciton binding energy, and their importance in the realization of room-temperature semiconductor lasers based on GaN, *Phys. Rev. B* **58**, 16333–16339 (1998).
- [57] R. Ulbrich, Energy Relaxation of Photoexcited Hot Electrons in GaAs, *Phys. Rev. B* **8**, 5719–5727 (1973).
- [58] P. Paskov, T. Paskova, P. Holtz, and B. Monemar, Polarized photoluminescence study of free and bound excitons in free-standing GaN, *Phys. Rev. B* **70**, 035210 (2004).
- [59] K. P. Korona, Dynamics of excitonic recombination and interactions in homoepitaxial GaN, *Phys. Rev. B* **65**, 235312 (2002).
- [60] L. C. Andreani, A. D’Andrea, and R. del Sole, Excitons in confined systems: from quantum well to bulk behaviour, *Phys. Lett. A* **168**, 451–459 (1992).
- [61] P. Ščajev, K. Jarašiūnas, S. Okur, U. Özgür, and H. Morkoç, Carrier dynamics in bulk GaN, *J. Appl. Phys.* **111**, 023702 (2012).
- [62] C. Pfüller, O. Brandt, F. Grosse, T. Flissikowski, C. Chèze, V. Consonni, L. Geelhaar, H. T. Grahn, and H. Riechert, Unpinning the Fermi level of GaN nanowires by ultraviolet radiation, *Phys. Rev. B* **82**, 045320 (2010).
- [63] J. R. Haynes, Experimental Proof of the Existence of a New Electronic Complex in Silicon, *Phys. Rev. Lett.* **4**, 361–363 (1960).
- [64] H. B. Bebb and E. W. Williams, Photoluminescence I. Theory, volume 8 of *Semiconductors and Semimetals*, page 181, Academic Press, Inc., New York, USA (1972).

Bibliography

- [65] M. Suffczynski, W. Gorzkowski, and R. Kowalczyk, Excitons bound to charged donors, *Phys. Lett. A* **24**, 453–454 (1967).
- [66] E. I. Rashba and G. E. Gurgenishvili, Edge Absorption Theory in Semiconductors, *Phys. Solid State* **4**, 759–760 (1962).
- [67] B. Monemar, Bound excitons in GaN, *J. Phys. Condens. Matter* **13**, 7011 (2001).
- [68] A. Wysmołek, K. P. Korona, R. Stępniewski, J. M. Baranowski, J. Błoniarczyk, M. Potemski, R. Jones, D. Look, J. Kuhl, S. Park, and S. Lee, Recombination of excitons bound to oxygen and silicon donors in freestanding GaN, *Phys. Rev. B* **66**, 245317 (2002).
- [69] G. Pozina, S. Khromov, C. Hemmingsson, L. Hultman, and B. Monemar, Effect of silicon and oxygen doping on donor bound excitons in bulk GaN, *Phys. Rev. B* **84**, 165213 (2011).
- [70] P. J. Dean, J. R. Haynes, and W. F. Flood, New radiative recombination processes involving neutral donors and acceptors in silicon and germanium, *Phys. Rev.* **161**, 711–729 (1967).
- [71] J. A. Freitas Jr., W. J. Moore, B. V. Shanabrook, G. C. B. Braga, S. K. Lee, S. S. Park, and J. Y. Han, Donor-related recombination processes in hydride-vapor-phase epitaxial GaN, *Phys. Rev. B* **66**, 233311 (2002).
- [72] B. Monemar, P. Paskov, J. Bergman, T. Paskova, C. Hemmingsson, T. Malinauskas, K. Jarasiunas, P. Gibart, and B. Beaumont, Time-resolved spectroscopy of excitons bound at shallow neutral donors in HVPE GaN, *Physica B* **376–377**, 482–485 (2006).
- [73] L. Cerutti, J. Ristić, S. Fernández-Garrido, E. Calleja, A. Trampert, K. H. Ploog, S. Lazić, and J. M. Calleja, Wurtzite GaN nanocolumns grown on Si(001) by molecular beam epitaxy, *Appl. Phys. Lett.* **88**, 213114 (2006).
- [74] E. Calleja, J. Ristić, S. Fernández-Garrido, L. Cerutti, M. A. Sánchez-García, J. Grandal, A. Trampert, U. Jahn, G. Sánchez, A. Griol, and B. Sánchez, Growth, morphology, and structural properties of group-III-nitride nanocolumns and nanodisks, *Phys. Status Solidi* **244**, 2816–2837 (2007).
- [75] L. Geelhaar, C. Chèze, B. Jenichen, O. Brandt, C. Pfüller, S. Münch, R. Rothemund, S. Reitzenstein, A. Forchel, T. Kehagias, P. Komninou, G. P. Dimitrakopoulos, T. Karakostas, L. Lari, P. R. Chalker, M. H. Gass, and H. Riechert, Properties of GaN Nanowires Grown by Molecular Beam Epitaxy, *IEEE J. Sel. Topics Quantum Electron.* **17**, 878–888 (2011).
- [76] A. E. H. Love, *A Treatise on the Mathematical Theory of Elasticity*, Dover, New York, fourth edition (1944).

- [77] G. W. Housner and T. Vreeland Jr., *The Analysis of Stress and Deformation*, McMillan, New York (1966).
- [78] S. Timoshenko and J. N. Goodier, *Theory of Elasticity*, McGraw-Hill, New York, second edition (1951).
- [79] D. Sam-Giao, *Optical study of GaN nanowires and GaN/AlN microcavities.*, PhD thesis, Université de Grenoble (2012).
- [80] R. Calarco, M. Marso, T. Richter, A. I. Aykanat, R. J. Meijers, A. v. d. Hart, T. Stoica, and H. Lüth, Size-dependent photoconductivity in MBE-grown GaN-nanowires., *Nano Lett.* **5**, 981–984 (2005).
- [81] C. Pfüller, *Optical properties of single semiconductor nanowires and nanowire ensembles: Probing surface physics by photoluminescence spectroscopy*, PhD thesis, Humboldt-Universität zu Berlin (2011).
- [82] P. Corfdir, J. K. Zettler, C. Hauswald, S. Fernández-Garrido, O. Brandt, and P. Lefebvre, Sub-meV linewidth in GaN nanowire ensembles: Absence of surface excitons due to the field ionization of donors, *Phys. Rev. B* **90**, 205301 (2014).
- [83] P. Lefebvre, S. Albert, J. Ristić, S. Fernández-Garrido, J. Grandal, M.-A. Sánchez-García, and E. Calleja, Oxygen photo-adsorption related quenching of photoluminescence in group-III nitride nanocolumns, *Superlattices Microstruct.* **52**, 165–171 (2012).
- [84] O. Brandt, C. Pfüller, C. Chèze, L. Geelhaar, and H. Riechert, Sub-meV linewidth of excitonic luminescence in single GaN nanowires: Direct evidence for surface excitons, *Phys. Rev. B* **81**, 045302 (2010).
- [85] P. Corfdir and P. Lefebvre, Role of the dielectric mismatch on the properties of donors in semiconductor nanostructures bounded by air, *J. Appl. Phys.* **112**, 106104 (2012).
- [86] C. Pfüller, O. Brandt, T. Flissikowski, C. Chèze, L. Geelhaar, H. T. Grahn, and H. Riechert, Statistical analysis of excitonic transitions in single, free-standing GaN nanowires: Probing impurity incorporation in the poissonian limit, *Nano Res.* **3**, 881–888 (2010).
- [87] P. Lefebvre, S. Fernández-Garrido, J. Grandal, J. Ristić, M.-A. Sánchez-García, and E. Calleja, Radiative defects in GaN nanocolumns: Correlation with growth conditions and sample morphology, *Appl. Phys. Lett.* **98**, 083104 (2011).
- [88] E. Calleja, M. Sánchez-García, F. Sánchez, F. Calle, F. Naranjo, E. Muñoz, U. Jahn, and K. H. Ploog, Luminescence properties and defects in GaN nanocolumns grown by molecular beam epitaxy, *Phys. Rev. B* **62**, 16826–16834 (2000).

Bibliography

- [89] P. Corfdir, P. Lefebvre, J. Ristic, P. Valvin, E. Calleja, A. Trampert, J.-D. Ganière, and B. Deveaud-Plédran, Time-resolved spectroscopy on GaN nanocolumns grown by plasma assisted molecular beam epitaxy on Si substrates, *J. Appl. Phys.* **105**, 013113 (2009).
- [90] B. Monemar, P. Paskov, G. Pozina, C. Hemmingsson, J. Bergman, T. Kawashima, H. Amano, I. Akasaki, T. Paskova, S. Figge, D. Hommel, and A. Usui, Evidence for Two Mg Related Acceptors in GaN, *Phys. Rev. Lett.* **102**, 235501 (2009).
- [91] P. Corfdir, C. Hauswald, and J. Zettler, Stacking faults as quantum wells in nanowires: Density of states, oscillator strength and radiative efficiency, *Phys. Rev. B* **90**, 195309 (2014).
- [92] A. Das, J. Heo, M. Jankowski, W. Guo, L. Zhang, H. Deng, and P. Bhattacharya, Room Temperature Ultralow Threshold GaN Nanowire Polariton Laser, *Phys. Rev. Lett.* **107**, 66405 (2011).
- [93] J. B. Schlager, N. A. Sanford, K. A. Bertness, and A. Roshko, Injection-level-dependent internal quantum efficiency and lasing in low-defect GaN nanowires, *J. Appl. Phys.* **109**, 044312 (2011).
- [94] Y. S. Park, T. W. Kang, H. Im, S.-K. Lee, Y.-H. Cho, C. M. Park, M.-S. Han, and R. A. Taylor, Effects of Surface Recombination on Exciton Dynamics in GaN Nanorods, *J. Nanoelectron. Optoelectron.* **4**, 307–311(5) (2009).
- [95] Y. S. Park, H. Im, L. Sun-Kyun, C. Yong-Hoon, and R. A. Taylor, Micro- and Time-resolved Photoluminescence in GaN Nanorods with Different Diameters, *J. Korean Phys. Soc.* **57**, 756 (2010).
- [96] A. Gorgis, T. Flissikowski, O. Brandt, C. Chèze, L. Geelhaar, H. Riechert, and H. T. Grahn, Time-resolved photoluminescence spectroscopy of individual GaN nanowires, *Phys. Rev. B* **86**, 041302(R) (2012).
- [97] K. P. Korona, Z. R. Zytkeiwicz, P. Perkowska, J. Borysiuk, M. Sobanska, J. Binder, and K. Klosek, Photoluminescence Dynamics of GaN / Si Nanowires, *Acta Phys. Pol. A* **122**, 1001–1003 (2012).
- [98] J. Yoo, Y.-J. Hong, S. J. An, G.-C. Yi, B. Chon, T. Joo, J.-W. Kim, and J.-S. Lee, Photoluminescent characteristics of Ni-catalyzed GaN nanowires, *Appl. Phys. Lett.* **89**, 043124 (2006).
- [99] L. Wischmeier, T. Voss, I. Rückmann, J. Gutowski, A. Mofor, A. Bakin, and A. Waag, Dynamics of surface-excitonic emission in ZnO nanowires, *Phys. Rev. B* **74**, 195333 (2006).

- [100] Q. X. Zhao, L. L. Yang, M. Willander, B. E. Sernelius, and P. O. Holtz, Surface recombination in ZnO nanorods grown by chemical bath deposition, *J. Appl. Phys.* **104**, 073526 (2008).
- [101] W. Shockley and W. T. Read Jr., Statistics of the Recombinations of Holes and Electrons, *Phys. Rev.* **87**, 835–842 (1952).
- [102] R. Hall, Electron-Hole Recombination in Germanium, *Phys. Rev.* **87**, 387–387 (1952).
- [103] T. Sugahara, H. Sato, M. Hao, Y. Naoi, S. Kurai, S. Tottori, K. Yamashita, K. Nishino, L. T. Romano, and S. Sakai, Direct Evidence that Dislocations are Non-Radiative Recombination Centers in GaN, *Jpn. J. Appl. Phys.* **37**, L398–L400 (1998).
- [104] R. Aleksiejūnas, M. Sūdžius, T. Malinauskas, J. Vaitkus, K. Jarašiūnas, and S. Sakai, Determination of free carrier bipolar diffusion coefficient and surface recombination velocity of undoped GaN epilayers, *Appl. Phys. Lett.* **83**, 1157 (2003).
- [105] J. B. Schlager, K. A. Bertness, P. T. Blanchard, L. H. Robins, A. Roshko, and N. A. Sanford, Steady-state and time-resolved photoluminescence from relaxed and strained GaN nanowires grown by catalyst-free molecular-beam epitaxy, *J. Appl. Phys.* **103**, 124309 (2008).
- [106] C. Hauswald, T. Flissikowski, H. T. Grahn, L. Geelhaar, H. Riechert, and O. Brandt, Radiative and nonradiative decay of excitons in GaN nanowires, In J.-I. Chyi, Y. Nanishi, H. Morkoç, J. Piprek, E. Yoon, and H. Fujioka, editors, *Proc. SPIE*, volume 8986, page 89860V (2014).
- [107] B. Saleh and M. Teich, *Fundamentals of Photonics*, volume 2, Wiley-VCH, Hoboken, NJ, USA (2007).
- [108] J. D. Joannopoulos, P. R. Villeneuve, and S. Fan, Photonic crystals: putting a new twist on light, *Nature* **386**, 143–149 (1997).
- [109] M. Boroditsky, T. F. Krauss, R. Coccioli, R. Vrijen, R. Bhat, and E. Yablonovitch, Light extraction from optically pumped light-emitting diode by thin-slab photonic crystals, *Applied Physics Letters* **75**, 1036 (1999).
- [110] J. C. M. Garnett, Colours in Metal Glasses and in Metallic Films, *Philos. Trans. R. Soc. A Math. Phys. Eng. Sci.* **203**, 385–420 (1904).
- [111] Z. Xiong, F. Zhao, J. Yang, and X. Hu, Comparison of optical absorption in Si nanowire and nanoporous Si structures for photovoltaic applications, *Appl. Phys. Lett.* **96**, 181903 (2010).
- [112] C. Pfüller, M. Ramsteiner, O. Brandt, F. Grosse, A. Rathsfeld, G. Schmidt, L. Geelhaar, and H. Riechert, Raman spectroscopy as a probe for the coupling of light into ensembles of sub-wavelength-sized nanowires, *Appl. Phys. Lett.* **101**, 083104 (2012).

Bibliography

- [113] R. Mata, A. Cros, K. Hestroffer, and B. Daudin, Surface optical phonon modes in GaN nanowire arrays: Dependence on nanowire density and diameter, *Phys. Rev. B* **85**, 035322 (2012).
- [114] A.-L. Henneghien, G. Tourbot, B. Daudin, O. Lartigue, Y. Désières, and J.-M. Gérard, Optical anisotropy and light extraction efficiency of MBE grown GaN nanowires epilayers., *Opt. Express* **19**, 527–39 (2011).
- [115] P. M. Wu, N. Anttu, H. Q. Xu, L. Samuelson, and M.-E. Pistol, Colorful InAs nanowire arrays: from strong to weak absorption with geometrical tuning., *Nano Lett.* **12**, 1990–1995 (2012).
- [116] N. Anttu and H. Q. Xu, Efficient light management in vertical nanowire arrays for photovoltaics, *Opt. Express* **21**, 27589–27605 (2013).
- [117] O. L. Muskens, J. G. Rivas, R. E. Algra, E. P. A. M. Bakkers, and A. Lagendijk, Design of light scattering in nanowire materials for photovoltaic applications, *Nano Lett.* **8**, 2638–2642 (2008).
- [118] G. Grzela, D. Hourlier, and J. Gómez Rivas, Polarization-dependent light extinction in ensembles of polydisperse vertical semiconductor nanowires: A Mie scattering effective medium, *Phys. Rev. B* **86**, 045305 (2012).
- [119] M. A. Sanchez-García, E. Calleja, E. Monroy, F. Sanchez, F. Calle, E. Muñoz, and R. Beresford, The effect of the III/V ratio and substrate temperature on the morphology and properties of GaN- and AlN-layers grown by molecular beam epitaxy on Si(111), *J. Cryst. Growth* **183**, 23–30 (1998).
- [120] K. A. Bertness, N. A. Sanford, J. M. Barker, J. B. Schlager, A. Roshko, A. V. Davydov, and I. Levin, Catalyst-free growth of GaN nanowires, *Journal of Electronic Materials* **35**, 576–580 (2006).
- [121] R. Calarco, R. J. Meijers, R. K. Debnath, T. Stoica, E. Sutter, and H. Lüth, Nucleation and growth of GaN nanowires on Si(111) performed by molecular beam epitaxy., *Nano Lett.* **7**, 2248–2251 (2007).
- [122] K. A. Bertness, A. Roshko, L. Mansfield, T. Harvey, and N. Sanford, Mechanism for spontaneous growth of GaN nanowires with molecular beam epitaxy, *J. Cryst. Growth* **310**, 3154–3158 (2008).
- [123] V. Consonni, A. Trampert, L. Geelhaar, and H. Riechert, Physical origin of the incubation time of self-induced GaN nanowires, *Appl. Phys. Lett.* **99**, 033102 (2011).
- [124] F. Schuster, F. Furtmayr, R. Zamani, C. Magén, J. R. Morante, J. Arbiol, J. A. Garrido, and M. Stutzmann, Self-Assembled GaN Nanowires on Diamond., *Nano Lett.* **12**, 2199–2204 (2012).

- [125] D. Tsivion and E. Joselevich, Guided growth of epitaxially coherent GaN nanowires on SiC., *Nano Lett.* **13**, 5491–5496 (2013).
- [126] S. Fernández-Garrido, V. M. Kaganer, K. K. Sabelfeld, T. Gotschke, J. Grandal, E. Calleja, L. Geelhaar, and O. Brandt, Self-Regulated Radius of Spontaneously Formed GaN Nanowires in Molecular Beam Epitaxy., *Nano Lett.* **13**, 3274–3280 (2013).
- [127] T. Gotschke, *Untersuchungen zum geordneten Wachstum von III-Nitrid Nanodrähten: Analyse der Nukleations-, Dekompositions- und Diffusionsmechanismen*, PhD thesis, Humboldt-Universität zu Berlin (2012).
- [128] M. Yoshizawa, A. Kikuchi, M. Mori, N. Fujita, and K. Kishino, Growth of Self-Organized GaN Nanostructures on Al₂O₃(0001) by RF-Radical Source Molecular Beam Epitaxy, *Jpn. J. Appl. Phys.* **36**, L459–L462 (1997).
- [129] V. Consonni, Self-induced growth of GaN nanowires by molecular beam epitaxy: A critical review of the formation mechanisms, *Phys. stat. sol. RRL* **7**, 699–712 (2013).
- [130] R. S. Wagner and W. C. Ellis, Vapor-Liquid-Solid Mechanism of Single Crystal Growth, *Appl. Phys. Lett.* **4**, 89 (1964).
- [131] S. Fernández-Garrido, X. Kong, T. Gotschke, R. Calarco, L. Geelhaar, A. Trampert, and O. Brandt, Spontaneous Nucleation and Growth of GaN Nanowires: The Fundamental Role of Crystal Polarity., *Nano Lett.* **12**, 6119–6125 (2012).
- [132] S. Fernández-Garrido, J. Grandal, E. Calleja, M. A. Sanchez-García, and D. Lopez-Romero, A growth diagram for plasma-assisted molecular beam epitaxy of GaN nanocolumns on Si(111), *J. Appl. Phys.* **106**, 126102 (2009).
- [133] V. Consonni, M. Hanke, M. Knelangen, L. Geelhaar, A. Trampert, and H. Riechert, Nucleation mechanisms of self-induced GaN nanowires grown on an amorphous interlayer, *Phys. Rev. B* **83**, 035310 (2011).
- [134] V. Consonni, M. Knelangen, L. Geelhaar, A. Trampert, and H. Riechert, Nucleation mechanisms of epitaxial GaN nanowires: Origin of their self-induced formation and initial radius, *Phys. Rev. B* **81**, 085310 (2010).
- [135] K. K. Sabelfeld, V. M. Kaganer, F. Limbach, P. Dogan, O. Brandt, L. Geelhaar, and H. Riechert, Height self-equilibration during the growth of dense nanowire ensembles: Order emerging from disorder, *Appl. Phys. Lett.* **103**, 133105 (2013).
- [136] A.-L. Bavencove, G. Tourbot, J. Garcia, Y. Désières, P. Gilet, F. Levy, B. André, B. Gayral, B. Daudin, and L. S. Dang, Submicrometre resolved optical characterization of green nanowire-based light emitting diodes., *Nanotechnology* **22**, 345705 (2011).

Bibliography

- [137] F. Limbach, C. Hauswald, J. Lähnemann, M. Wölz, O. Brandt, A. Trampert, M. Hanke, U. Jahn, R. Calarco, L. Geelhaar, and H. Riechert, Current path in light emitting diodes based on nanowire ensembles., *Nanotechnology* **23**, 465301 (2012).
- [138] K. Kishino and K. Yamano, Green-Light Nanocolumn Light Emitting Diodes with Triangular-Lattice Uniform Arrays of InGaN-Based Nanocolumns, *IEEE J. Quantum Electron.* **50**, 538–547 (2014).
- [139] S. Ishizawa, H. Sekiguchi, A. Kikuchi, and K. Kishino, Selective growth of GaN nanocolumns by Al thin layer on substrate, *Phys. Status Solidi* **244**, 1815–1819 (2007).
- [140] K. Kishino, T. Hoshino, S. Ishizawa, and A. Kikuchi, Selective-area growth of GaN nanocolumns on titanium-mask-patterned silicon (111) substrates by RF-plasma-assisted molecular-beam epitaxy, *Electron. Lett.* **44**, 819–821 (2008).
- [141] K. A. Bertness, A. W. Sanders, D. M. Rourke, T. E. Harvey, A. Roshko, J. B. Schlager, and N. A. Sanford, Controlled Nucleation of GaN Nanowires Grown with Molecular Beam Epitaxy, *Adv. Funct. Mater.* **20**, 2911–2915 (2010).
- [142] A. Bengoechea-Encabo, F. Barbagini, S. Fernández-Garrido, J. Grandal, J. Ristić, M. A. Sanchez-García, E. Calleja, U. Jahn, E. Luna, and A. Trampert, Understanding the selective area growth of GaN nanocolumns by MBE using Ti nanomasks, *J. Cryst. Growth* **325**, 89–92 (2011).
- [143] T. Schumann, T. Gotschke, F. Limbach, T. Stoica, and R. Calarco, Selective-area catalyst-free MBE growth of GaN nanowires using a patterned oxide layer., *Nanotechnology* **22**, 095603 (2011).
- [144] CODATA webpage (accessed on 16.06.2014), <http://www.codata.org/>.
- [145] Refractiveindex.info webpage (accessed on 16.06.2014), <http://refractiveindex.info/>.
- [146] Hamamatsu - A guide to streak cameras, p. 3 (accessed on 09.06.2014), http://www.hamamatsu.com/resources/pdf/sys/e_streakh.pdf.
- [147] S. Hess, R. A. Taylor, K. Kyhm, J. Ryan, B. Beaumont, and P. Gibart, Femtosecond Exciton Dynamics and the Mott Transition in GaN under Resonant Excitation, *Phys. stat. sol. (b)* **216**, 57–62 (1999).
- [148] K. A. Bertness, N. A. Sanford, and A. V. Davydov, GaN Nanowires Grown by Molecular Beam Epitaxy, *IEEE J. Sel. Top. Quantum Electron.* **17**, 847–858 (2011).
- [149] B. Jenichen, O. Brandt, C. Pfüller, P. Dogan, M. Knelangen, and A. Trampert, Macro- and micro-strain in GaN nanowires on Si(111)., *Nanotechnology* **22**, 295714 (2011).

- [150] V. M. Kaganer, B. Jenichen, O. Brandt, S. Fernández-Garrido, P. Dogan, L. Geelhaar, and H. Riechert, Inhomogeneous strain in GaN nanowires determined from x-ray diffraction peak profiles, *Phys. Rev. B* **86**, 115325 (2012).
- [151] S. Fernández-Garrido, V. M. Kaganer, C. Hauswald, B. Jenichen, M. Ramsteiner, V. Consonni, L. Geelhaar, and O. Brandt, Correlation between the structural and optical properties of spontaneously formed GaN nanowires: a quantitative evaluation of the impact of nanowire coalescence, *Nanotechnology* **25**, 455702 (2014).
- [152] P. Corfdir, F. Feix, J. K. Zettler, S. Fernández-Garrido, and O. Brandt, Importance of the dielectric contrast for the polarization of excitonic transitions in single GaN nanowires, submitted (2014).
- [153] F. Vietmeyer, M. P. McDonald, and M. Kuno, Single Nanowire Microscopy and Spectroscopy, *J. Phys. Chem. C* **116**, 12379–12396 (2012).
- [154] J. Giblin, F. Vietmeyer, M. P. McDonald, and M. Kuno, Single nanowire extinction spectroscopy, *Nano Lett.* **11**, 3307–3311 (2011).
- [155] A. V. Maslov and C. Z. Ning, Reflection of guided modes in a semiconductor nanowire laser, *Appl. Phys. Lett.* **83**, 1237 (2003).
- [156] A. V. Maslov and C. Z. Ning, Far-field emission of a semiconductor nanowire laser, *Opt. Lett.* **29**, 572–574 (2004).
- [157] A.-L. Henneghien, B. Gayral, Y. Désières, and J.-M. Gérard, Simulation of waveguiding and emitting properties of semiconductor nanowires with hexagonal or circular sections, *J. Opt. Soc. Am. B* **26**, 2396–2403 (2009).
- [158] E. O. Schäfer-Nolte, T. Stoica, T. Gotschke, F. Limbach, E. Sutter, P. Sutter, D. Grützmacher, and R. Calarco, Enhanced light scattering of the forbidden longitudinal optical phonon mode studied by micro-Raman spectroscopy on single InN nanowires., *Nanotechnology* **21**, 315702 (2010).
- [159] J. Christen, T. Riemann, F. Bertram, D. Rudloff, P. Fischer, A. Kaschner, U. Haboek, A. Hoffmann, and C. Thomsen, Optical micro-characterization of group-III-nitrides: correlation of structural, electronic and optical properties, *Phys. stat. sol. (c)* **0**, 1795–1815 (2003).
- [160] J. Lähnemann, *Luminescence of group-III-V nanowires containing heterostructures*, PhD thesis, Humboldt-Universität zu Berlin (2013).
- [161] S. K. Lim, M. Brewster, F. Qian, Y. Li, C. M. Lieber, and S. Gradecak, Direct correlation between structural and optical properties of III-V nitride nanowire heterostructures with nanoscale resolution, *Nano Lett.* **9**, 3940–3944 (2009).

Bibliography

- [162] L. Ahtapodov, J. Todorovic, P. Olk, T. Mjåland, P. Slåttnes, D. L. Dheeraj, A. T. J. Helvoort, B.-O. Fimland, and H. Weman, A Story Told by a Single Nanowire: Optical Properties of Wurtzite GaAs, *Nano Lett.* **12**, 6090–6095 (2012).
- [163] H.-Y. Chen, H.-W. Lin, C.-H. Shen, and S. Gwo, Structure and photoluminescence properties of epitaxially oriented GaN nanorods grown on Si(111) by plasma-assisted molecular-beam epitaxy, *Appl. Phys. Lett.* **89**, 243105 (2006).
- [164] C. Hauswald, P. Corfdir, J. K. Zettler, V. M. Kaganer, K. K. Sabelfeld, S. Fernández-Garrido, T. Flissikowski, V. Consonni, T. Gotschke, H. T. Grahn, L. Geelhaar, and O. Brandt, Origin of the nonradiative decay of bound excitons in GaN nanowires, *Phys. Rev. B* **90**, 165304 (2014).
- [165] K. J. Vahala, Optical microcavities, *Nature* **424**, 839–846 (2003).
- [166] E. M. Purcell, Spontaneous emission probabilities at radio frequencies, *Phys. Rev.* **69**, 674 (1946).
- [167] C. Kölper, M. Sabathil, B. Witzigmann, F. Römer, W. Bergbauer, and M. Strassburg, Optical Properties of Individual GaN Nanorods for Light Emitting Diodes: Influence of Geometry, Materials and Facets, *Proc. SPIE* **7933**, 7933141–7933149 (2011).
- [168] R. Paniagua-Domínguez, G. Grzela, J. G. Rivas, and J. A. Sánchez-Gil, Enhanced and directional emission of semiconductor nanowires tailored through leaky/guided modes., *Nanoscale* **5**, 10582–10590 (2013).
- [169] J. Bleuse, J. Claudon, M. Creasey, N. Malik, J.-M. Gérard, I. Maksymov, J.-P. Hugonin, and P. Lalanne, Inhibition, Enhancement, and Control of Spontaneous Emission in Photonic Nanowires, *Phys. Rev. Lett.* **106**, 103601 (2011).
- [170] C. Hauswald, T. Flissikowski, T. Gotschke, R. Calarco, L. Geelhaar, H. T. Grahn, and O. Brandt, Coupling of exciton states as the origin of their biexponential decay dynamics in GaN nanowires, *Phys. Rev. B* **88**, 075312 (2013).
- [171] K. A. Grossklous, A. Banerjee, S. Jahangir, P. Bhattacharya, and J. M. Millunchick, Misorientation defects in coalesced self-catalyzed GaN nanowires, *J. Cryst. Growth* **371**, 142–147 (2013).
- [172] S. Satpathy, Eigenstates of Wannier excitons near a semiconductor surface, *Phys. Rev. B* **28**, 4585 (1983).
- [173] M. Suffczynski and L. Wolniewicz, Size of exciton bound to a neutral impurity, *Phys. Rev. B* **40**, 6250–6257 (1989).

- [174] P. Corfdir, J. Ristić, P. Lefebvre, T. Zhu, D. Martin, A. Dussaigne, J. D. Ganière, N. Grandjean, and B. Deveaud-Plédran, Low-temperature time-resolved cathodoluminescence study of exciton dynamics involving basal stacking faults in A-plane GaN, *Appl. Phys. Lett.* **94**, 201115 (2009).
- [175] O. Brandt, P. Waltereit, S. Dhar, U. Jahn, Y. J. Sun, A. Trampert, K. H. Ploog, M. A. Tagliente, and L. Tapfer, Properties of (In,Ga)N/GaN quantum wells grown by plasma-assisted molecular beam epitaxy, *J. Vac. Sci. Technol. B* **20**, 1626–1639 (2002).
- [176] O. Brandt, J. Ringling, K. H. Ploog, H.-J. Wünsche, and F. Henneberger, Temperature dependence of the radiative lifetime in GaN, *Phys. Rev. B* **58**, R15977–R15980 (1998).
- [177] P. Dogan, O. Brandt, C. Pfüller, A.-K. Bluhm, L. Geelhaar, and H. Riechert, GaN nanowire templates for the pendeoepitaxial coalescence overgrowth on Si(111) by molecular beam epitaxy, *J. Cryst. Growth* **323**, 418–421 (2011).
- [178] O. Brandt, S. Fernández-Garrido, J. Zettler, E. Luna, U. Jahn, C. Chèze, and V. M. Kaganer, Statistical analysis of the shape of one-dimensional nanostructures: determining the coalescence degree of spontaneously formed GaN nanowires, *Cryst. Growth Des.* **14**, 2246–2253 (2014).
- [179] B. Monemar, S. Khromov, G. Pozina, P. Paskov, P. Bergman, C. Hemmingsson, L. Hultman, H. Amano, V. Avrutin, X. Li, and H. Morkoç, Luminescence of Acceptors in Mg-Doped GaN, *Jpn. J. Appl. Phys.* **52**, 08JJ03 (2013).
- [180] M. N. Saha, On a Physical Theory of Stellar Spectra, *Proc. R. Soc. A Math. Phys. Eng. Sci.* **99**, 135–153 (1921).
- [181] M. J. Dresser, The Saha-Langmuir Equation and its Application, *J. Appl. Phys.* **39**, 338 (1968).
- [182] D. S. Chemla, Quasi-two-dimensional excitations in GaAs / Al_xGa_{1-x}As semiconductor multiple quantum well structures, *Helv. Phys. Acta* **56**, 607–637 (1983).
- [183] B. Gil, P. Bigenwald, M. Leroux, P. Paskov, and B. Monemar, Internal structure of the neutral donor-bound exciton complex in cubic zinc-blende and wurtzite semiconductors, *Phys. Rev. B* **75**, 085204 (2007).
- [184] J. Shah, Photoexcited hot electrons and excitons in CdSe at 2 K, *Phys. Rev. B* **9**, 562–567 (1974).
- [185] C. G. Van de Walle and D. Segev, Microscopic origins of surface states on nitride surfaces, *J. Appl. Phys.* **101**, 081704 (2007).
- [186] D. Blossey, Wannier Exciton in an Electric Field. II. Electroabsorption in Direct-Band-Gap Solids, *Phys. Rev. B* **3**, 1382–1391 (1971).

Bibliography

- [187] T. Yamabe, A. Tachibana, and H. Silverstone, Theory of the ionization of the hydrogen atom by an external electrostatic field, *Phys. Rev. A* **16**, 877–890 (1977).
- [188] P. Corfdir, J. Levrat, A. Dussaigne, P. Lefebvre, H. Teisseyre, I. Grzegory, T. Suski, J.-D. Ganière, N. Grandjean, and B. Deveaud-Plédran, Intrinsic dynamics of weakly and strongly confined excitons in nonpolar nitride-based heterostructures, *Phys. Rev. B* **83**, 245326 (2011).
- [189] K. Kishino, H. Sekiguchi, and A. Kikuchi, Improved Ti-mask selective-area growth (SAG) by rf-plasma-assisted molecular beam epitaxy demonstrating extremely uniform GaN nanocolumn arrays, *J. Cryst. Growth* **311**, 2063–2068 (2009).
- [190] A. Bengoechea-Encabo, S. Albert, M. Sanchez-Garcia, L. López, S. Estradé, J. Rebled, F. Peiró, G. Nataf, P. de Mierry, J. Zuniga-Perez, and E. Calleja, Selective area growth of a- and c-plane GaN nanocolumns by molecular beam epitaxy using colloidal nanolithography, *J. Cryst. Growth* **353**, 1–4 (2012).
- [191] Luxpop webpage (accessed on 09.11.2012), <http://www.luxpop.com/>.
- [192] E. D. Palik, *Handbook of optical constants of solids*, Academic Press, Inc., San Diego, CA, USA (1985).
- [193] R. Jayaprakash, D. Ajagunna, S. Germanis, M. Androulidaki, K. Tsagaraki, A. Georgakilas, and N. T. Pelekanos, Extraction of absorption coefficients from as-grown GaN nanowires on opaque substrates using all-optical method, *Opt. Express* **22**, 19555 (2014).
- [194] N. Anttu, Geometrical optics, electrostatics, and nanophotonic resonances in absorbing nanowire arrays, *Opt. Lett.* **38**, 730–732 (2013).
- [195] L. Cao, J. S. White, J.-S. Park, J. A. Schuller, B. M. Clemens, and M. L. Brongersma, Engineering light absorption in semiconductor nanowire devices, *Nat. Mater.* **8**, 643–647 (2009).
- [196] M. Heiss, E. Russo-Averchi, A. Dalmau-Mallorquí, G. Tütüncüoğlu, F. Matteini, D. Ruffer, S. Conesa-Boj, O. Demichel, E. Alarcon-Lladó, and A. Fontcuberta i Morral, III–V nanowire arrays: growth and light interaction, *Nanotechnology* **25**, 014015 (2014).
- [197] J. Chesin, X. Zhou, and S. Gradečak, Light extraction in individual GaN nanowires on Si for LEDs, *Proc. SPIE* **8467**, 846703 (2012).
- [198] J. Chesin and S. Gradečak, Comparing directed efficiency of III-nitride nanowire light-emitting diodes, *J. Nanophotonics* **8**, 083095 (2014).

- [199] Y. Fontana, G. Grzela, E. P. A. M. Bakkers, and J. Rivas, Mapping the directional emission of quasi-two-dimensional photonic crystals of semiconductor nanowires using Fourier microscopy, *Phys. Rev. B* **86**, 245303 (2012).
- [200] G. Grzela, R. Paniagua-Domínguez, T. Barten, Y. Fontana, J. A. Sánchez-Gil, and J. Gómez Rivas, Nanowire antenna emission, *Nano Lett.* **12**, 5481–5486 (2012).
- [201] G. Pozina, C. Hemmingsson, J. P. Bergman, D. Trinh, L. Hultman, and B. Monemar, Dynamics of bound excitons versus thickness in freestanding GaN wafers grown by halide vapor phase epitaxy, *Appl. Phys. Lett.* **90**, 221904 (2007).
- [202] Y. J. Sun, O. Brandt, and K. H. Ploog, Photoluminescence intensity of GaN films with widely varying dislocation density, *J. Mater. Res.* **18**, 1247–1250 (2011).
- [203] C. Li, L. Guo, Z. Wu, L. Ren, X. Ai, J. Zhang, Y. Lv, H. Xu, and D. Yu, Photoluminescence and time-resolved photoluminescence of star-shaped ZnO nanostructures, *Solid State Commun.* **139**, 355–359 (2006).
- [204] C. Pfüller, O. Brandt, T. Flissikowski, H. T. Grahn, T. Ive, J. S. Speck, and S. P. DenBaars, Comparison of the spectral and temporal emission characteristics of homoepitaxial and heteroepitaxial ZnO nanowires, *Appl. Phys. Lett.* **98**, 113113 (2011).
- [205] J. S. Reparaz, G. Callsen, M. R. Wagner, F. Güell, J. R. Morante, C. M. Sotomayor Torres, and A. Hoffmann, Spatial mapping of exciton lifetimes in single ZnO nanowires, *APL Mater.* **1**, 012103 (2013).
- [206] Z. N. Urgessa, J. R. Botha, M. O. Eriksson, C. M. Mbulanga, S. R. Dobson, S. R. Tankio Djiokap, K. F. Karlsson, V. Khranovskyy, R. Yakimova, and P.-O. Holtz, Low temperature near band edge recombination dynamics in ZnO nanorods, *J. Appl. Phys.* **116**, 123506 (2014).
- [207] R. R. LaPierre, A. C. E. Chia, S. J. Gibson, C. M. Haapamaki, J. Boulanger, R. Yee, P. Kuyanov, J. Zhang, N. Tajik, N. Jewell, and K. M. A. Rahman, III-V nanowire photovoltaics: Review of design for high efficiency, *Phys. stat. sol. RRL* **7**, 815–830 (2013).
- [208] W. K. Burton, N. Cabrera, and F. C. Frank, The Growth of Crystals and the Equilibrium Structure of their Surfaces, *Philos. Trans. R. Soc. A Math. Phys. Eng. Sci.* **243**, 299–358 (1951).
- [209] A. Ishizaka and Y. Murata, Crystal growth model for molecular beam epitaxy: Role of kinks on crystal growth, *J. Phys. Condens. Matter* **6**, L693–L698 (1994).
- [210] J. K. Zettler, private communication (2014).

Bibliography

- [211] J. Wallentin, N. Anttu, D. Asoli, M. Huffman, I. Åberg, M. H. Magnusson, G. Siefert, P. Fuss-Kailuweit, F. Dimroth, B. Witzigmann, H. Q. Xu, L. Samuelson, K. Deppert, and M. T. Borgström, InP Nanowire Array Solar Cells Achieving 13.8% Efficiency by Exceeding the Ray Optics Limit, *Science* **339**, 1057–1060 (2013).
- [212] K. Hong, J. Noolandi, and R. Street, Theory of radiative recombination by diffusion and tunneling in amorphous Si:H, *Phys. Rev. B* **23**, 2967–2976 (1981).
- [213] A. K. Jonscher and A. de Polignac, The time dependence of luminescence in solids, *J. Phys. C Solid State Phys.* **17**, 6493–6519 (1984).
- [214] K. Seki, M. Wojcik, and M. Tachiya, Dispersive-diffusion-controlled distance-dependent recombination in amorphous semiconductors, *J. Chem. Phys.* **124**, 044702 (2006).
- [215] O. Brandt and K. H. Ploog, Solid-state lighting: The benefit of disorder, *Nat. Mater.* **5**, 769–770 (2006).
- [216] C.-N. Brosseau, M. Perrin, C. Silva, and R. Leonelli, Carrier recombination dynamics in $\text{In}_x\text{Ga}_{1-x}\text{N}/\text{GaN}$ multiple quantum wells, *Phys. Rev. B* **82**, 085305 (2010).
- [217] J. Piprek, Efficiency droop in nitride-based light-emitting diodes, *Phys. status solidi* **207**, 2217–2225 (2010).
- [218] M.-H. Kim, M. F. Schubert, Q. Dai, J. K. Kim, E. F. Schubert, J. Piprek, and Y. Park, Origin of efficiency droop in GaN-based light-emitting diodes, *Appl. Phys. Lett.* **91**, 183507 (2007).
- [219] J. Iveland, L. Martinelli, J. Peretti, J. S. Speck, and C. Weisbuch, Direct Measurement of Auger Electrons Emitted from a Semiconductor Light-Emitting Diode under Electrical Injection: Identification of the Dominant Mechanism for Efficiency Droop, *Phys. Rev. Lett.* **110**, 177406 (2013).
- [220] F. Bertazzi, M. Goano, X. Zhou, M. Calciati, G. Ghione, M. Matsubara, and E. Bellotti, Comment on “Direct Measurement of Auger Electrons Emitted from a Semiconductor Light-Emitting Diode under Electrical Injection: Identification of the Dominant Mechanism for Efficiency Droop” [*Phys. Rev. Lett.* 110, 177406 (2013)], <http://arxiv.org/abs/1305.2512> (2013).
- [221] M. Binder, A. Nirschl, R. Zeisel, T. Hager, H.-J. Lugauer, M. Sabathil, D. Bougeard, J. Wagner, and B. Galler, Identification of nnp and npp Auger recombination as significant contributor to the efficiency droop in (GaIn)N quantum wells by visualization of hot carriers in photoluminescence, *Appl. Phys. Lett.* **103**, 071108 (2013).
- [222] C. A. Schneider, W. S. Rasband, and K. W. Eliceiri, NIH Image to ImageJ: 25 years of image analysis, *Nat. Methods* **9**, 671–675 (2012).

List of Figures

2.1.	Wurtzite crystal structure and lifting of the degeneracy of the valence band	6
2.2.	Excitation of free carriers in a direct semiconductor	7
2.3.	Exciton-polariton coupling	10
2.4.	Photoluminescence and reflectance spectra of free-standing GaN	12
3.1.	Scanning electron micrographs of a spontaneously grown GaN NW ensemble	22
3.2.	Scanning electron micrographs of NW ensembles grown by SAG	24
3.3.	Schematic diagram of the μ -PL setup and principle of a confocal setup	25
3.4.	Schematic diagram of the μ -TRPL setup	28
3.5.	Schematic diagram of the concept of a streak camera	29
3.6.	Extracting TRPL transients and spectra from a streak camera image	30
4.1.	Comparison of the PL spectra of single GaN NWs and the respective NW ensemble	38
4.2.	μ -PL maps of single free-standing GaN NWs in a sample grown by SAG	41
4.3.	Low-temperature μ -PL spectra of single freestanding GaN NWs grown by SAG	43
5.1.	Low-temperature bound-exciton PL transient of GaN NWs	46
5.2.	Top-view scanning electron micrographs of the investigated NW samples	50
5.3.	TRPL transients of the (D^0, X_A) transition for various GaN NW samples together with a simulation	51
5.4.	Low-temperature PL spectrum and PL transient (within the first ns) of sample R	54
5.5.	Spectral deconvolution of the TRPL data from sample R	55
5.6.	Temperature dependence of the PL spectrum, integrated cw PL intensity and lifetimes of sample R	56
5.7.	Schematic energy diagrams visualizing the rate-equation model for free and bound excitons	58

List of Figures

5.8. Schematic energy diagrams and simulated TRPL transients for case 'A' and 'B'	60
5.9. Effective (D^0, X_A) lifetime of 19 different GaN NW ensembles in dependence of the parameter d^*	62
5.10. Effective (D^0, X_A) lifetime of 19 different GaN NW ensembles in dependence of the coalescence degree of the ensemble	64
6.1. Low-temperature PL transients for the investigated samples	68
6.2. Top-view scanning electron micrographs of the investigated samples	69
6.3. Low-temperature cw μ -PL spectra of the investigated samples	70
6.4. Streak camera images and transient PL spectra obtained at different times	71
6.5. PL transients of the investigated samples obtained after the spectral deconvolution	72
6.6. Schematic energy diagram visualizing the employed rate equation system	73
6.7. Simulated PL transients obtained from a numerical solution of the rate equation system	73
6.8. Calculated ratio between free exciton capture and bound exciton release	76
6.9. High energy part of the time-integrated PL spectra and derived carrier temperature	77
6.10. Schematic representation of the electric potential across a GaN NW	78
6.11. Low temperature PL transients for different bound excitons complexes in sample R	79
7.1. Bright-field optical microscope image and scanning electron micrograph of the SAG GaN NW arrays under investigation	84
7.2. Low-temperature PL spectra and intensity of ordered GaN NW arrays	85
7.3. PL transients for ordered GaN NW arrays with different NW diameter	86
7.4. Absorbance, transmittance and reflectance of a GaN slab	88
7.5. JCMsuite simulation domain	89
7.6. Absorbance, transmittance and reflectance of an ordered GaN NW array grown on Si	90
7.7. Dependence of the absorbance on the angle of the incident light and NW pitch	92
7.8. Measured and absorbance-corrected, integrated PL intensity of various ordered GaN NW arrays	93
7.9. Simulation domain and extraction efficiency of a single dipole inside a GaN NW	94
7.10. Cross-sectional mode profiles for guided modes in GaN NWs	96
7.11. Dispersion of guided modes in GaN NWs	97
7.12. Farfield intensity distribution of the TE01 and TM01 mode extracted from a GaN NW	99

A.1. Cross-sectional scanning electron micrograph of a spontaneously grown GaN NW ensemble	110
A.2. Comparison of the equivalent disk diameter and the parameter d^* of GaN NWs	111
A.3. Circularity and area–perimeter plot	113
A.4. Cross-sectional secondary electron micrographs of different GaN NW arrays grown by SAG	114

List of Tables

3.1. Summary of the properties of the two microscope objectives employed for the μ -PL measurements	26
4.1. Spot size, corresponding excitation area on the sample and approximate number of NWs being excited during PL and TRPL measurements for an as-grown NW ensemble with a typical NW density of $5 \times 10^9 \text{ cm}^{-2}$	39
5.1. Summary of various structural parameters and extracted leffective lifetimes of several GaN NW samples	52
5.2. Parameters used in the rate equation model Eqs. (5.4)–(5.5) to compute the PL transients shown in Fig. 5.8(b) and the effective rate constants given by Eqs. (5.6)–(5.7).	59
6.1. Summary of the free parameters, all in units of ns^{-1} , of the rate equation model [Eqs. (6.1)–(6.3)] used for computing the PL transients shown in Fig. 6.7.	72
B.1. List of samples investigated in this thesis. All samples are GaN NWs grown on Si(111) substrates.	115